POLITECNICO
MILANO 1863

Department of Aerospace Science & Technology
Doctoral Program in Aerospace Engineering

Experimental observation of supersonic non-ideal compressible-fluid flows

Doctoral Dissertation of:
Marta Zocca

Supervisor:
Prof. Alberto Guardone

Co-Supervisor:
Prof. Andrea Spinelli

Tutor:
Prof. Luigi Vigevano

The Chair of the Doctoral Program:
Prof. Luigi Vigevano

January 2018 – Cycle XXX

“There is a pleasure in the pathless woods,
There is a rapture on the lonely shore,
There is society where none intrudes,
By the deep Sea, and music in its roar:
I love not Man the less, but Nature more,
From these our interviews, in which I steal
From all I may be, or have been before,
To mingle with the Universe, and feel
What I can ne’er express, yet cannot all conceal."

George Gordon Byron

Acknowledgements

The research work presented in this thesis was carried out at Politecnico di Milano, Italy, in the Laboratory of Compressible-fluid dynamics for Renewable Energy Applications (CREALab), between years 2014 and 2017. The research was partially funded by the European Research Council under Grant ERC Consolidator 2013, project NSHOCK 617603.

I would like to thank the many people who contributed to this work.

First of all, I would like to express my sincere gratitude to my supervisor, Professor Alberto Guardone, for his valuable and relentless guidance, and to my co-supervisor, Professor Andrea Spinelli, who introduced me and made me get into experimental research. Many thanks to Professor Fabio Cozzi for the interesting discussions during the years.

Special thanks go to all my colleagues and friends of the CREALab, Barbara, Camilla, Davide, Gianluca, Giorgia, Giulio, Luuc, Simone for the time spent together, whether or not doing research.

Many thanks also to the technicians of the CREALab and of the Laboratorio di Fluidodinamica delle Macchine for their help in the preparation of experimental trials.

I would like to thank the reviewers, Professor Carlo Osnaghi and Professor Teemu Turunen-Saaresti for the time devoted to the review of this thesis and for their valuable suggestions.

Finally, I would like to express my thankfulness to my family. May this achievement be a reward for their support on this path.

Marta Zocca
Milano, January 2018

Summary

The branch of fluid mechanics devoted to the study of compressible flows whose behaviour deviates from the one predicted by the ideal-gas model is termed Non-Ideal Compressible-Fluid Dynamics (NICFD). Departure from ideal behaviour is typically observed in fluids made of complex molecules, operating in thermodynamic conditions close to the liquid-vapour saturation curve and critical point. Differently from the ideal-gas case, non-ideal flow dynamics is strongly influenced by the process conditions, and peculiar flow patterns such as rarefaction shock waves, shock waves with either upstream or downstream sonic states, and split shocks are physically admissible. Complex thermodynamic models were devised and applied to the theoretical analysis and numerical simulation of non-ideal flows. However, only few experimental data in the NICFD regime were available up to date.

In the present thesis, experimental benchmark tests are devised and measurements are performed to provide assessment to NICFD theory, thermodynamic models and numerical simulation tools. Experiments are carried out in the Test Rig for Organic VApors (TROVA), the blow-down wind tunnel of the Laboratory of Compressible-fluid dynamics for Renewable Energy Applications (CREALab) of Politecnico di Milano, while numerical simulations are performed using the open-source NICFD solver SU2. Two main flow configurations are considered, namely adapted flows in planar converging-diverging nozzles and uniform supersonic flows with oblique shock waves and expansion fans.

An experimental campaign is carried out to study the NICFD flow of siloxane vapour MDM (octamethyltrisiloxane, $C_8H_{24}O_2Si_3$) in a planar converging-diverging nozzle. The nozzle is designed using the method of characteristics, complemented with state-of-the-art Equations of State (EoS) dealing with non-ideal flow behaviour. Operation of the nozzle is characterised through pressure and temperature measurements, schlieren visualizations, and numerical simulations. Numerical simulations and theoretical predictions based on the isentropic hypothesis for nozzle expansions agree well with experimental data. Consistently with NICFD theory, reservoir conditions are found to significantly influence both the pressure ratio and the Mach number distribution along the nozzle axis.

Numerical simulations and the NICFD theory are then extensively applied to the study of supersonic expansions in converging-diverging nozzles, both in the ideal and NICFD regimes. Two different topics related to the design and operation of converging-diverging nozzles are addressed. First, a design solution aimed at fixing the location of the minimum-area section of the nozzle is discussed. The geometry of planar converging-diverging nozzles operating with air and MDM is modified by the introduction of a small recessed step at the geometrical throat. The recessed step triggers boundary layer separation and fixes the location of the minimum-area section of the nozzle. Experiments and numerical simulations are applied to the analysis of the adapted flow. A complex perturbation wave pattern originates at the step location, and propagates up to the exhaust section of the nozzle through multiple reflections at the nozzle walls and interactions at the nozzle symmetry axis. Pressure measurements performed along the nozzle axis show that the perturbation introduced by the step influences the flow only locally. For the nozzle operating with MDM in the NICFD regime, the configuration of the perturbation wave pattern in the throat region is found to depend on reservoir conditions. Second, a key parameter for the design and performance analysis of supersonic nozzles is investigated, namely the discharged massflow rate. A closed-form expression for this parameter is derived analytically. The massflow rate is found to be dependent on the radius of curvature of the nozzle profile at the throat section, on the molecular complexity

of the working fluid, and on process conditions. A numerical verification of the dependence of the discharged massflow rate on relevant design parameters is performed, both in the ideal and non-ideal flow regimes. The dependence of the massflow rate on the fluid properties and on process conditions is confirmed. Moreover, the discharged massflow rate is found to be affected by the overall shape of the converging portion, and not only by the local curvature of the nozzle profile at the throat section. This is true even in the case of smooth convergents.

A second experimental campaign is carried out to characterize oblique shock waves and expansion fans occurring in the NICFD regime. A diamond-shaped airfoil with semi-aperture 7.5° at leading edge and 10° at the trailing edge is placed in a uniform supersonic stream of MDM, which in test conditions is a single-phase vapour lying in the NICFD region. Two oblique shocks at the airfoil leading-edge and centered expansion fans at the shoulder are observed. Oblique shock waves and expansion fans are studied at varying upstream stagnation conditions, for six deviation angles in the range ϑ = 6.5°-10° obtained by changing the attitude of the model with respect to the wind tunnel axis. Experimental results are assessed against the inviscid shock-expansion theory for two-dimensional steady flows, complemented with state-of-the-art EoS. All the geometrical configurations and operating conditions explored in wind-tunnel tests are reproduced numerically. In the inviscid core of the flow, where measurements are performed, numerical results agree fairly well with experimental data. A significant dependence of the pre-shock, post-shock and post-expansion states on the corresponding upstream flow conditions is found, and the speed of sound is seen to decrease across shock waves and increase upon expansion fans, consistently with the NICFD theory applied to the tested thermodynamic conditions.

Contents

List of Figures

List of Tables

Nomenclature

Acronyms

BZT	Bethe-Zel'dovich-Thompson
CFD	Computational Fluid Dynamics
EoS	Equation of State
HMC	High Molecular Complexity
HPV	High-Pressure Vessel
iPRSV	improved Peng Robinson Stryjek Vera
CREALab	Laboratory of Compressible-fluid dynamics for Renewable Energy Applications
LMC	Low Molecular Complexity
LPV	Low-Pressure Vessel
MOC	Method Of Characteristics
NICFD	Non-Ideal Compressible-Fluid Dynamics
MDM	Octamethyltrisiloxane, $C_8H_{24}O_2Si_3$
ORC	Organic Rankine Cycle
PIG	Polytropic Ideal Gas
SW	Span Wagner
TROVA	Test-Rig for Organic Vapours
vdW	van der Waals

Subscripts

D	Post-expansion state (expansion fan)
B	Post-shock state, Pre-expansion state (expansion fan)
A	Pre-shock state
r	Reduced variables made dimensionless by critical point values
c	Thermodynamic variables at critical point
e	Variables evaluated at the exhaust section
t	Variables evaluated at the throat section

Greek alphabet

ρ	Density
ϑ	Flow deviation angle
Γ	Fundamental derivative of gasdynamics
β	Shock angle
γ	Specific heat ratio
α	Specific Helmoltz free energy

Latin alphabet

Z	Compressibility factor
A	Cross-sectional area of a nozzle
C_D	Discharge coefficient
S	Entropy
U	Expanded uncertainty (gaussian, 95% confidence level)
F	Helmoltz free energy
E	Internal energy
M	Mach number
x	Mass fraction
$\dot{m}$	Massflow rate
M_m	Molecular mass
r_t	Non-dimensional radius of curvature of the nozzle profile at the throat

N	Number of active degrees of freedom of a molecule, Number of grid points and elements
P	Pressure
h	Specific enthalpy per unit mass
s	Specific entropy per unit mass
R	Specific gas constant
c_v	Specific heat at constant volume
e	Specific internal energy per unit mass
v	Specific volume
c	Speed of sound
T	Temperature
H	Throat half-height
$\mathcal{R}$	Universal gas constant
$\mathbf{u}$	Velocity vector
V	Volume

Superscripts

$\tilde{\cdot}$	Perturbation variables for the small-perturbation transonic solution at the nozzle throat
$\bar{\cdot}$	Reference sonic state for the small-perturbation transonic solution at the nozzle throat
t	Total thermodynamic state

1 Introduction

1.1 Motivation for the research

Flows of molecularly complex substances in the single-phase vapour region close to the liquid-vapour saturation curve and critical point evolve through a sequence of thermodynamic states which can be quantitatively and qualitatively different from the ones predicted by the ideal-gas model of dilute gases. The knowledge of the flow behaviour in aerodynamic devices operating in dilute-gas conditions is well-established and satisfactory. Provided that the specific heat at constant volume is constant during the process, the flow dynamics depends only on the ratio of the reservoir to ambient pressure and on the polytropic exponent. Differently from the ideal-gas case, the process conditions, namely, the initial thermodynamic state and expansion or compression ratio, together with the fluid characteristics determine the dynamics of a *real* gas. Here, the term real does not refer to dissipative mechanisms such as internal friction and heat conduction or to chemical reactions. Rather, it indicates the occurrence of peculiar flow behaviour because of departure from dilute, ideal-gas thermodynamics. The branch of fluid mechanics devoted to the study of these flows is termed *Non-Ideal Compressible-Fluid Dynamics* (NICFD).

Fluid flows featuring so-called *non-ideal* behaviour close to saturation and critical point, or within the supercritical region, are encountered in a number of aerospace and industrial applications, including rocket propulsion, wind tunnels for aerodynamic testing, and turbomachinery. Fluids in the vicinity of the liquid-vapour saturation curve can be adopted as oxidizers in hybrid rocket motors (e.g. N_2O) and can be exploited for surface cooling to reduce ablation and degradation of nozzle performance (see e.g. (Sutton & Biblarz (2001)) and Guardone (2011)). As a matter of fact, operation in the vicinity of the liquid-vapour saturation curve allows to increase the heat transfer rates at a relatively constant fluid temperature and pressure, thanks to the contribution of latent heat of vaporization. Gases made of molecules of high molecular mass can be used in supersonic wind tunnels instead of air to achieve higher Reynolds numbers, which can be varied almost independently from the Mach number, see Sagnier & Vérant (1998). As far as process engineering applications are concerned, non-ideal flow conditions are found for example in *Organic Rankine Cycle* (ORC) plants, namely Rankine cycles using a molecularly-complex organic compound instead of water as working fluid (see e.g.Angelino *et al.* (1991), Larjola (1995), Colonna *et al.* (2015), and Macchi & Astolfi (2016)). Since the specific vaporization heat of organic fluids is much lower than that of water, Rankine cycles operating with organic fluids are particularly suitable for the exploitation of heat sources such as waste heat from industrial processes, geothermal reservoirs, biomass combustion, and concentrated solar radiation. The thermodynamic state of the single-phase vapour at the inlet of an ORC turbine stator usually belongs to the non-ideal thermodynamic region close to liquid-vapour saturation curve and critical point. Moreover, since the speed of sound of this class of fluids is low compared to that of air and other simple gases, expansion processes in turbine stators involve supersonic outlet flows even if modest flow velocities are attained (Brown & Argrow (2000), Colonna *et al.* (2008*b*)). In these conditions, oblique shock waves occur within the blade passages and at the trailing edge of the blades, thus entailing significant entropy generation (Denton (1993)). Supersonic flows in the NICFD regime also occur in industrial and power generation applications using *supercritical carbon dioxide* (sCO_2) as working fluid, e.g. in sCO_2 power cycles (Feher (1968), Brun *et al.* (2017)) and in the rapid expansion of supercritical solutions (RESS) for particle generation or extraction of chemicals (Helfgen *et al.* (2003)). In this respect, an accurate treatment of the flow behaviour in the NICFD regime, both in converging-diverging ducts delivering supersonic outlet flows and across oblique compression

and expansion waves, is key for a proper design of aerodynamic devices performing expansion and compression of flows which can be no longer described by the ideal-gas model.

To date, extensive theoretical effort in the field of NICFD brought to a deep understanding of the phenomenological features of non-ideal fluid flows, see e.g. Kluwick (2017) for a concise review. Complex thermodynamic models were devised and implemented in *Computational Fluid Dynamics* (CFD) codes. However, due to the lack of measurements in the NICFD regime, none of the currently available NICFD CFD codes was ever assessed against experimental data. The accuracy of the simulations results, which amplifies the unknown accuracy of the underlying thermodynamic models, is therefore highly questionable. Currently, several research groups are devoting their efforts to fill this gap. At Delft University of Technology, two experimental test-rigs were designed and commissioned to carry out both fundamental and applied research on NICFD flows. The first one is the Flexible Asymmetric Shock Tube (FAST), a Ludwieg-tube facility designed to verify the occurrence of rarefaction shock waves in molecularly complex dense vapours (see Colonna *et al.* (2008*a*)), where Mathijssen *et al.* (2015) successfully performed preliminary rarefaction wave experiments in the dense vapour region of cyclic siloxane fluid D_6 (dodecamethylcyclohexasiloxane $C_{12}H_{36}O_6Si_6$). The second one is the Organic Rankine Cycle Hybrid Integrated Device (ORCHID), a facility implementing a high-temperature ORC and capable of accommodating two interchangeable test sections, namely a supersonic nozzle and a mini-ORC expander with power output up to 100 kW_e (see Head *et al.* (2016)). Experimental campaigns envisaged for the near future include the characterization of expansions in supersonic nozzles and of shock-wave patterns on models and obstacles of varying geometry (Head *et al.* (2017)). At Whittle Laboratory of University of Cambridge, the ORC Ludwieg tube, a Ludwieg-tube facility designed to operate with several gases including air, CO_2 and organic fluids, is currently being used to study supersonic axial vane cascades, with particular attention to trailing edge loss analysis, see e.g. Galiana *et al.* (2017). A micro-ORC test-tig using the waste heat of the exhaust gases of a Diesel engine as heat source and linear siloxane MDM (octamethyltrisiloxane $C_8H_24O_2Si_3$) as working fluid was recently built at the Laboratory of Fluid Dynamics at Lappeenranta University of Technology. The prime mover of the ORC is a hermetic high-speed turbo-generator-feed pump, in which the working fluid also acts as lubricant. Uusitalo *et al.* (2017) reported results of the first test runs, in which the vapour exiting the evaporator was expanded through an expansion valve replacing the turbogenerator. In a second experimental campaign, documented by Turunen-Saaresti *et al.* (2017), tests were run with the turbogenerator installed in the plant, and electric power was extracted, up to a measured power output of 5.1 kW_e. At Münster University of Applied Sciences, a closed-loop continuous-running wind tunnel implementing a closed gas cycle was designed, as documented by Reinker *et al.* (2016) and Reinker *et al.* (2017). In the test section, simple nozzle geometries as well as turbine blade cascades can be tested. The facility, named Closed Loop Organic Wind Tunnel (CLOWT), is designed to operate with fluorketone Novec^{TM} 649 ($CF_3CF_2C(O)CF(CF_3)_2$), and is currently being built.

The work documented in this thesis fits within this framework, and represents a contribution to the experimental research aimed at providing assessment to NICFD theory, thermodynamic models and simulation tools. Experiments are carried out in the supersonic blow-down wind tunnel TROVA (*Test Rig for Organic Vapours*) of the *Laboratory of Compressible-Fluid Dynamics for Renewable Energy Applications* (CREALab), Politecnico di Milano (Spinelli *et al.* (2013), Guardone *et al.* (2013), and Pini *et al.* (2011)). Different flow configurations are designed and tested in the NICFD regime, including converging-diverging nozzles and a supersonic airfoil, and experimental measurements are assessed against the NICFD theory and numerical simulations using state-of-the-art thermodynamic models. Specifically, simplified experimental benchmark tests are devised, and measurements are carried out to provide reference experimental results which could contribute to the phenomenological understanding of NICFD and to the improvement of

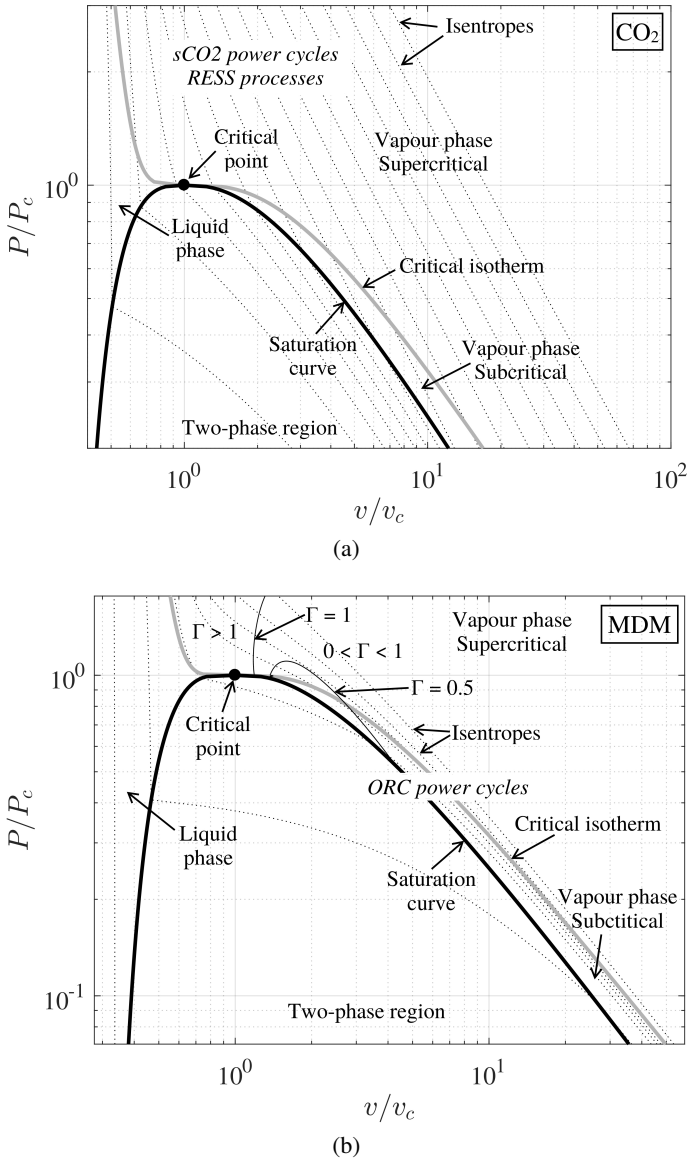

Figure 1.1: *P-v* diagram for (a) carbon dioxide, CO_2 (LMC fluid) and (b) octamethyltrisiloxane MDM, $C_8H_{24}O_2Si_3$ (HMC fluid)

thermodynamic models. Numerical and analytical methods for NICFD flows are extensively applied to provide assessment of design solutions and performance parameters of supersonic nozzles operating in the non-ideal regime.

1.2 Non-Ideal Compressible-Fluid Dynamics

The present paragraph provides a brief overview of non-ideal flow phenomena, with focus on the flow configurations investigated throughout the thesis, namely expanding flows in converging-diverging nozzles and supersonic flows with oblique shock waves and expansion fans occurring in the NICF regime.

The curvature of an isentrope drawn in the pressure-specific volume plane corresponds to the second partial derivative of specific volume with respect to pressure. This derivative, written

in non-dimensional form, is referred to as the *fundamental derivative of gasdynamics*, Γ (see Thompson (1971)):

$$\Gamma \equiv \frac{c^4}{2v^3}\left(\frac{\partial^2 v}{\partial P^2}\right)_s \tag{1.1}$$

where c is the speed of sound, v is the specific volume, P is the pressure, and s is the specific entropy per unit mass. Thermodynamic manipulation leads to the following alternative expressions of the fundamental derivative:

$$\Gamma = 1 + \frac{c}{v}\left(\frac{\partial c}{\partial P}\right)_s \tag{1.2}$$

According to eq. 1.2, Γ can be interpreted as a non-dimensional measure of the variation of the speed of sound with pressure along an isentropic transformation. The effect of Γ on the dynamic behaviour of compressible fluids is of paramount importance: for ideal gases, Γ is always > 1, whereas molecularly complex fluids having sufficiently large specific heats are expected to exhibit a finite region of negative Γ in the neighbourhood of the saturated vapour line at pressures and temperatures of the order of the critical values. Following Colonna & Guardone (2006), the *molecular complexity* of a fluid can be defined as the number of active degrees of freedom N of a molecule, including vibrational degrees of freedom which, at a given temperature, can be partially or fully activated. Kluwick (2004) showed that a $0 < \Gamma < 1$ region exists in the vapour phase of a polytropic van der Waals fluid, provided $N > N^{\mathrm{HMC}} \simeq 7.57$, where the acronym HMC, introduced by Colonna & Guardone (2006), stands for *High Molecular Complexity*. For $N > N^{\mathrm{BZT}} \simeq 33.33$, a $\Gamma < 0$ region exists alongside the $0 < \Gamma < 1$ region. Fluids exhibiting a negative-Γ region are commonly referred to as *Bethe-Zel'dovich-Thompson* (BZT) fluids, due to the significant contributions by these authors in recognizing the existence of such region in van der Waals gases with large specific heats and in formulating the typical gasdynamic problems considering general *Equations of State* (EoS), see Bethe (1942), Zel'dovich (1946), Zel'dovich & Raizer (1966), and Thompson (1971). For fluids having $3 < N < N^{\mathrm{HMC}}$, where 3 is the number of active degrees of freedom of a monoatomic gas, only the region $\Gamma > 1$ exists. Fluids of this class are termed LMC fluids, where LMC stands for *Low Molecular Complexity*. Figure 1.1 reports the P-v diagram for carbon dioxide, a LMC fluid (Fig. 1.1a), and for MDM, a HMC fluid (Fig. 1.1b), according to state-of-the-art thermodynamic models. On the two diagrams, the saturation dome, the critical isotherm and selected isentropes are reported. The typical thermodynamic states attained by such fluids in common industrial applications are also indicated for reference.

In the study of NICFD, it is customary to distinguish between the so-called *non-classical* ($\Gamma \leq 0$) and *classical* ($\Gamma > 0$) regimes. In the classical regime, evolution towards thermodynamically stable states at higher entropy realizes through compression waves possibly steepening into shocks and expansion waves spreading out as fans. The opposite is true for non-classical flows, namely, expansion waves may steepen into shocks and compression waves may spread out as fans. A further distinction can be made within the classical regime: for $\Gamma > 1$, the speed of sound c increases with pressure P, which is the behaviour of usual substances. For a Polytropic Ideal Gas, Eq. 1.2 reduces to $\Gamma = (\gamma + 1)/2$, which is always positive and greater than 1. For $0 < \Gamma < 1$, which is referred to as *non-ideal classical regime*, the speed of sound decreases with pressure, see for instance Lambrakis & Thompson (1972) and Kluwick (2017).

A fluid having constant negative Γ cannot be accelerated supersonically from a stagnation state (Thompson (1971)). This means that the supersonic conditions are attainable only if Γ is positive in some region of the flow connecting the stagnation and supersonic states. Phenomena occurring in fluids with $\Gamma < 0$ have no counterpart in the classical theory of gases: expansion shocks, the partial disintegration of both compression and expansion shocks, shock splitting and sonic shocks. Classical converging-diverging nozzles are not suitable to generate shock-free flows

if the medium is taken from one side of the $\Gamma > 0$ region to the other side as it accelerates from subsonic to supersonic speeds. Nozzles of rather unconventional shape with two throats are required to accommodate the non-monotone behaviour of the Mach number across the expansion and to avoid the occurrence of shocks, see for example Cramer & Best (1991), Cramer & Fry (1993), and Kluwick (1993).

In the present thesis, focus is mainly placed on supersonic flows of single-constituent fluids in the non-ideal classical regime. Specifically, steady isentropic expansions in converging-diverging nozzles and supersonic flows with oblique shocks and expansion waves are investigated. The theoretical formulation of such flows valid for the complex EoS presented in paragraph 1.2.1 is reviewed in paragraphs 1.2.2 and 1.2.3.

1.2.1 Thermodynamic models

To describe non-ideal fluid dynamics phenomena, suitable EoS are to be selected. Due to its simplicity, the van der Waals (vdW) model has often been used for a qualitative description of non-ideal compressible fluids effects. For a better accuracy, more complex EoS, such as the Peng-Robinson EoS and complex multiparameter EoS are to be employed. In the present paragraph, the EoS adopted throughout the thesis to describe the behaviour of flows featuring $\Gamma < 1$ are introduced. The properties of thermodynamic systems are defined following the approach to thermodynamics presented e.g. by Callen (1985) and Gyftopoulos & Beretta (1991).

For a single-constituent thermodynamic system in stable equilibrium state, the value of any property is uniquely determined by the energy E, the volume V and the mass M of the system. Indeed, among all the states with the same values of (E, V, M), the Second Law of thermodynamics guarantees that there exists one and only one stable equilibrium state, which is the one corresponding to the maximum value of the entropy S. The state principle, applied to the property entropy, reads:

$$S = S(E, V, M) \tag{1.3}$$

The above equation 1.3 is called the *fundamental relation* of the stable equilibrium state in entropy form. The Second Law of Thermodynamics and the requirement of stability for the considered equilibrium states guarantee strict monotonicity of entropy with respect to energy. The entropy function in eq. 1.3 can thus be inverted to obtain the fundamental relation for the stable equilibrium state in energy form:

$$E = E(S, V, M) \tag{1.4}$$

Each partial derivative of the fundamental relation represents a *property* of the system in the considered stable equilibrium state. An equivalent form of the fundamental relation in energy form can be obtained by taking the partial Legendre transform of the function defined by eq. 1.4 and substituting the independent variable S with the partial derivative of E with respect to S. This derivative is the definition of the intensive variable temperature T, namely:

$$T \equiv \frac{\partial E}{\partial S} \tag{1.5}$$

The partial Legendre transform of the fundamental relation in energy form eq. 1.4, with S substituted by T as independent variable, yields the function

$$F = F(T, V, M) \tag{1.6}$$

which is an equivalent form of the fundamental relation for the same stable equilibrium state. Function F is the Helmoltz free energy of the system, and reads:

$$F = E - TS \tag{1.7}$$

Under the *simple system* model assumption (see e.g. Gyftopoulos & Beretta (1991)), the fundamental relations in entropy and energy form, eq. 1.3 and 1.4, are homogeneous functions of first degree in all their variables, thus they can be written in terms of specific variables as:

$$S = S(E, V, M) = Ms(e, v, x) \quad \text{and} \quad E = E(S, V, M) = Me(s, v, x) \tag{1.8}$$

where s is the specific entropy, e the specific internal energy, v the specific volume and x the mass fraction. For a *single-constituent* fluid, $x = 1$, and the two fundamental relations in entropy and energy form can be written in terms of specific variables as:

$$s = s(e, v) \quad \text{and} \quad e = e(s, v) \tag{1.9}$$

All thermodynamic properties of a stable equilibrium state can be calculated by taking derivatives of the fundamental relation with respect to its independent variables. Different thermodynamic models are obtained by assigning relations to the partial derivatives of the fundamental relation, and by assuming these relations, i.e. the EoS, as definitions of the intensive variables. For single-constituent simple systems, the knowledge of two EoS is equivalent to the knowledge of the fundamental relation. From the fundamental relation expressed in the Helmoltz free energy form $\alpha = \alpha(T, v)$, the following EoS are derived:

$$P = P(T, v) \quad \text{and} \quad e = e(T, v) \tag{1.10}$$

$P = P(T, v)$ is referred to as the *Thermal EoS* and $e = e(T, v)$ as the *Caloric EoS*.

In the *ideal-gas* assumption, valid in dilute-gas conditions, gases are modelled as identical point-particles interacting with each other only through elastic collisions. The thermal and caloric EoS read:

$$\begin{aligned} P(T, v) &= \frac{RT}{v} \\ e(T, v) = e(T) &= e_0 + \int_{T_0}^{T} c_v(\mathcal{T})\mathrm{d}\mathcal{T} \end{aligned} \tag{1.11}$$

where

- R is the specific gas constant, namely the ratio of the universal gas constant $\mathcal{R}$ to the molecular mass M_m of the fluid

$$R = \frac{\mathcal{R}}{M_m}, \qquad \mathcal{R} = 8.314 \, \frac{\mathrm{kJ}}{\mathrm{kmol\,K}} \tag{1.12}$$

- subscript $(\cdot)_0$ indicates an arbitrary reference state
- c_v is the specific heat at constant volume, defined as

$$c_v = \left(\frac{\partial e}{\partial T} \right)_v \tag{1.13}$$

If constant specific heat is also assumed, the internal energy depends linearly on temperature and the model is called *Polytropic Ideal Gas* (PIG) model.

The *van der Waals* (vdW) model (van der Waals (1873)) is the simplest model capable of representing in a qualitative way both liquid and vapour homogeneous states. In the vdW model, particles have a finite volume and interact through elastic collisions, subject to weak long-range attractive forces and strong short-range repulsive forces. The validity of model can be extended

to the two-phase region by introducing a correction based on the Maxwell construction. The vdW thermal and caloric EoS are:

$$\begin{aligned} P(T,v) &= \frac{RT}{v-b} - \frac{a}{v^2} \\ e(T,v) &= e_0 + \int_{T_0}^{T} c_v(\mathcal{T})\mathrm{d}\mathcal{T} - \frac{a}{v} \end{aligned} \tag{1.14}$$

where a, $a > 0$ accounts for the long-range attractive intermolecular forces, and b, $b > 0$ accounts for the short-range repulsive intermolecular forces, due to the finite dimension of particles. Both parameters are substance-specific and depend on critical temperature T_c and pressure P_c. The thermodynamic state at the critical point can in turn be determined by solving the following system of equations:

$$\begin{cases} \left.\dfrac{\partial P}{\partial v}\right|_{T_c,v_c} = 0 \\ \left.\dfrac{\partial^2 P}{\partial v^2}\right|_{T_c,v_c} = 0 \end{cases} \tag{1.15}$$

This is equivalent to imposing that the critical isotherm has horizontal tangent and an inflection point at the critical point in the P-v thermodynamic diagram. From the solution of system eq. 1.15, with $P(T,v)$ given by the first of eq. 1.14, the two constants a and b read:

$$a = \frac{27}{64}\frac{(RT_c)^2}{P_c} \quad \text{and} \quad b = \frac{1}{8}\frac{RT_c}{P_c} \tag{1.16}$$

When dealing with flows of molecularly complex compounds, the improved Peng-Robinson-Stryjek-Vera EoS formulated by van der Stelt *et al.* (2012), and the multiparameter EoS by Span & Wagner (2003) and by Thol *et al.* (2017) are adopted.

The *improved Peng-Robinson-Stryjek-Vera* (iPRSV) cubic EoS is of the form:

$$P = \frac{RT}{v-b} - \frac{a}{v^2 + 2bv - b^2} \tag{1.17}$$

where

$$b = \frac{0.077796RT_c}{P_c} \tag{1.18}$$

and

$$a = \left(\frac{0.457235R^2T_c^2}{P_c}\right)\bar{\alpha} \tag{1.19}$$

The $\bar{\alpha}$-function includes a dependence on temperature, which allows to extend the range of applicability of the EoS to the low reduced temperature region and to polar fluids. The *reduced temperature* T_r is defined as the ratio of temperature T to the critical temperature T_c, namely

$$T_r = \frac{T}{T_c} \tag{1.20}$$

In the iPRSV model, the $\bar{\alpha}$-function reads:

$$\bar{\alpha} = \left[1 + \kappa\left(1 + \sqrt{T_r}\right)\right]^2 \tag{1.21}$$

The κ-function in the above equation 1.21 is in turn a continuous function of temperature, which reads:

$$\kappa = \kappa_0 + \kappa_1\left\{\sqrt{[A - D(T_r + B)]^2 + E} + A - D(T_r + B)\right\}\sqrt{T_r + C} \tag{1.22}$$

where

- κ_0 is a function of the acentric factor ω:

$$\kappa_0 = 0.378893 + 1.4897153\omega - 0.17131848\omega^2 + 0.0196554\omega^3 \tag{1.23}$$

- κ_1 is a pure-component parameter, which can be obtained by regressing experimental data
- A, B, C, D, and E are constant coefficients, whose values are:

$$A = 1.1, \quad B = 0.25, \quad C = 0.2, \quad D = 1.2, \quad E = 0.01 \tag{1.24}$$

For the calculation of caloric properties, the iPRSV EoS is complemented with a polynomial function of the temperature approximating the ideal-gas contribution to the isobaric heat capacity C_P:

$$\frac{C_P^0(T)}{R} = C_0 + C_1 T + C_2 T^2 + C_3 T^3 \tag{1.25}$$

where C_0, C_1, C_2, C_3 are substance-specific coefficients. Tabulated values of κ_1 and of coefficients C_0, C_1, C_2, and C_3 are reported by van der Stelt *et al.* (2012).

Finally, the *Span-Wagner* (SW) model is a state-of-the-art multiparameter EoS for non-polar and weakly polar fluids providing highly accurate thermodynamic properties for technical applications, even close to the critical point. It provides a functional form of the reduced Helmoltz free energy $\alpha_r(T, v)$, i.e. of the function

$$\alpha_r = \frac{\alpha}{RT} \tag{1.26}$$

in terms of the inverse of the reduced temperature $\tau = T_c/T$ and of the reduced density $\rho_r = \rho/\rho_c$, here denoted as δ for compactness. The function $\alpha_r = \alpha_r(\tau, \delta)$ is a fundamental relation for the stable equilibrium state defined by (τ, δ), thus all other thermodynamic properties can be calculated by taking derivatives of α_r with respect to its independent variables. The functional form for α_r comprises two terms, $\alpha_r^{\text{id.}}$ and $\alpha_r^{\text{n.id.}}$, which account for the ideal-gas contribution to the Helmoltz free energy and for the difference between non-ideal and ideal-gas behaviour:

$$\alpha_r(\tau, \delta) = \alpha_r^{\text{id.}}(\tau, \delta) + \alpha_r^{\text{n.id.}}(\tau, \delta) \tag{1.27}$$

The first term $\alpha_r^{\text{id.}}$ can be written as function of temperature T and density ρ as:

$$\alpha_r^{\text{id.}} = \alpha_{r_0} + \int_{T_0}^{T} \left(C_P^0 - R\right) \mathrm{d}\mathcal{T} - T \int_{T_0}^{T} \frac{C_P^0 - R}{T} \mathrm{d}\mathcal{T} + RT \ln\left(\frac{\rho}{\rho_0}\right) \tag{1.28}$$

where the isobaric heat capacity is given by eq. 1.25. The non-ideal term reads:

$$\begin{aligned} \alpha_r^{\text{n.id.}}(\tau, \delta) = \quad & n_1 \delta \tau^{0.25} + n_2 \delta \tau^{1.125} + n_3 \delta \tau^{1.5} \\ & + n_4 \delta^2 \tau^{1.375} + n_5 \delta^3 \tau^{0.25} + n_6 \delta^7 \tau^{0.875} \\ & + n_7 \delta^2 \tau^{0.625} \mathrm{e}^{-\delta} + n_8 \delta^5 \tau^{1.75} \mathrm{e}^{-\delta} + n_9 \delta \tau^{3.625} \mathrm{e}^{-\delta^2} \\ & + n_{10} \delta^4 \tau^{3.625} \mathrm{e}^{-\delta^2} + n_{11} \delta^3 \tau^{14.5} \mathrm{e}^{-\delta^3} + n_{12} \delta^4 \tau^{12.0} \mathrm{e}^{-\delta^3} \end{aligned} \tag{1.29}$$

where n_i, $i = 1, \ldots, 12$ are substance-specific parameters, which result from fitting or extrapolation of a set of experimental data. All experiments reported in the present thesis were performed in the TROVA wind tunnel, which was run with siloxane MDM as working fluid. The values of the parameters n_i for MDM were reported for the first time by Colonna *et al.* (2008*c*). Starting from a new set of experimental data, which include additional speed of sound measurements, Thol *et al.* (2017) improved the estimation of the parameters of the SW EoS and achieved a better representation of the caloric properties of MDM, especially close to the critical point. In the present work, the SW EoS of Thol *et al.* (2017) is used to compute reference thermodynamic quantities.

1.2.2 Non-ideal compressible-fluid flows in supersonic nozzles

The steady operation of de Laval nozzles can be studied by resorting to the *quasi-one-dimensional* approach (see e.g. Thompson (1988)), provided the radius of curvature of the nozzle axis at any streamwise location x is large compared to the nozzle cross-sectional length, and the cross-sectional area distribution along the nozzle axis $A(x)$ is smooth and gradual. Under such hypotheses, all flow variables are assumed to vary only along the streamwise coordinate x. Further assuming *adiabatic* flow with negligible body forces, the mass, momentum and energy balance equations reduce to:

$$\begin{aligned} \frac{1}{\rho}\frac{\mathrm{d}\rho}{\mathrm{d}x} + \frac{1}{u}\frac{\mathrm{d}u}{\mathrm{d}x} + \frac{1}{A}\frac{\mathrm{d}A}{\mathrm{d}x} &= 0 \\ \rho u\frac{\mathrm{d}u}{\mathrm{d}x} + \frac{\mathrm{d}P}{\mathrm{d}x} &= 0 \\ \frac{\mathrm{d}h^t}{\mathrm{d}x} &= 0 \end{aligned} \tag{1.30}$$

where ρ is the fluid density, u is the streamwise component of the flow velocity, $A = A(x)$ is the cross-sectional area distribution, P is the pressure and h^t the specific total enthalpy. The latter is defined as:

$$h^t = e + \frac{1}{2}u^2 + \frac{P}{\rho} = h + \frac{1}{2}u^2 \tag{1.31}$$

The mathematical statement expressed by eq. 1.30 is made complete by a suitable EoS for the fluid under scrutiny. In most applications of converging-diverging nozzles, including wind-tunnel flows, de Laval nozzles for supersonic propulsion and converging-diverging blade cascades in turbomachinery, ducts operate at sufficiently large Reynolds numbers for viscous effects (and related entropy production) to be neglected, at least to a first approximation, and viscous effects are limited to the thin boundary layer region. In the case of steady *isentropic* flows, the pressure gradient $\mathrm{d}P/\mathrm{d}x$ can be expressed in terms of the density gradient $\mathrm{d}\rho/\mathrm{d}x$ by introducing the definition of the speed of sound $c = (\partial P/\partial\rho)_s$:

$$\frac{\mathrm{d}P}{\mathrm{d}x} = \left(\frac{\partial P}{\partial\rho}\right)_s \frac{\mathrm{d}\rho}{\mathrm{d}x} \tag{1.32}$$

Manipulation of the governing equations, eq. 1.30, under the additional hypotesis of isentropic flow, which holds in the inviscid core provided that shock waves are present, allows to conveniently express the streamwise gradients of all the flow variables as function of the gradient of the known cross-sectional area distribution along the nozzle axis:

$$\begin{aligned} \frac{1}{u}\frac{\mathrm{d}u}{\mathrm{d}x} &= \frac{1}{M^2-1}\frac{1}{A}\frac{\mathrm{d}A}{\mathrm{d}x} \\ \frac{1}{\rho}\frac{\mathrm{d}\rho}{\mathrm{d}x} &= \frac{M^2}{1-M^2}\frac{1}{A}\frac{\mathrm{d}A}{\mathrm{d}x} \\ \frac{1}{P}\frac{\mathrm{d}P}{\mathrm{d}x} &= \frac{1}{1-M^2}\frac{\rho u^2}{P}\frac{1}{A}\frac{\mathrm{d}A}{\mathrm{d}x} \\ \frac{1}{c}\frac{\mathrm{d}c}{\mathrm{d}x} &= \frac{(\Gamma-1)M^2}{1-M^2}\frac{1}{A}\frac{\mathrm{d}A}{\mathrm{d}x} \\ \frac{1}{M}\frac{\mathrm{d}M}{\mathrm{d}x} &= \frac{1+(\Gamma-1)M^2}{M^2-1}\frac{1}{A}\frac{\mathrm{d}A}{\mathrm{d}x} \end{aligned} \tag{1.33}$$

The above set of equations, where $M = u/c$ is the flow Mach number and Γ the fundamental derivative of gasdynamics, highlights the role of Γ in determining the behaviour of subsonic ($M < 1$) and supersonic ($M > 1$) flows in the converging ($\mathrm{d}A/\mathrm{d}x < 0$) and diverging ($\mathrm{d}A/\mathrm{d}x > 0$) portions of a de Laval nozzle. For all Γ-regimes, a supersonic flow is compressed (ρ and P increase) and decelerated (u decreases) in a converging duct, while it is expanded (ρ and P decrease) and accelerated (u increases) in a diverging duct. The opposite is true for a subsonic flow. The fundamental derivative of gasdynamics appears explicitly in the last two relations of eq. 1.33, namely the ones expressing the speed of sound and Mach number gradients. For $\Gamma > 1$, an increase of the speed of sound is associated to a compression/deceleration and a decrease to an expansion/acceleration. The opposite is true for $\Gamma < 1$. The classical result by Thompson (1971) concerning Mach number variation at a throat (i.e. an area minimum) or at an antithroat (i.e. an area maximum) with sonic conditions follows directly from the last of eq. 1.33. Its limit as $M \to 1$ and $\mathrm{d}A/\mathrm{d}x \to 0$, calculated applying the de l'Hôpital's rule, yields:

$$\left(\frac{\mathrm{d}M}{\mathrm{d}x}\right)^2 \to \frac{\Gamma}{2A}\frac{\mathrm{d}^2A}{\mathrm{d}x^2} \tag{1.34}$$

The above result (eq. 1.34) means that, for a subsonic-supersonic transition to occur, a conventional throat (antithroat) is required if $\Gamma > 0$ ($\Gamma < 0$).

For fixed total enthalpy and entropy, the flow Mach number can be expressed as function of the density only as:

$$M(\rho; \bar{s}, \bar{h}^t) = \frac{u(\rho; \bar{s}, \bar{h}^t)}{c(\bar{s}, \rho)} = \frac{\sqrt{2\left[\bar{h}^t - h(\bar{s}, \rho)\right]}}{c(\bar{s}, \rho)} \tag{1.35}$$

where $\bar{s}$ and $\bar{h}^t$ are the constant values of the entropy and total enthalpy, respectively. Derivation of the above relation with respect to ρ yields:

$$\frac{\mathrm{d}M}{\mathrm{d}\rho}(\rho; \bar{s}, \bar{h}^t) = \frac{M(\rho; \bar{s}, \bar{h}^t)}{\rho}\left[1 - \Gamma(\bar{s}, \rho) - \frac{1}{M^2(\rho; \bar{s}, \bar{h}^t)}\right] \tag{1.36}$$

The Mach number, which for the ideal-gas case is a monotone decreasing function of density, could exhibit non-monotone behaviour if $\Gamma \leq 1$. Moreover, if $\Gamma < 0$, up to three sonic points could be simultaneously present.

Guardone & Vimercati (2016) give complete account of all the admissible solution patterns for BZT fluids expanding in converging-diverging nozzles, which include rarefaction shock waves, shock waves with either upstream or downstream sonic states, and split shocks. In the non-ideal classical case, which is the one investigated in the present thesis, the flow behaviour can qualitatively depart from its ideal-gas counterpart only for what concerns the increase of the speed of sound along the nozzle expansion and the non-monotone variation of the Mach number for certain stagnation conditions.

1.2.3 Oblique waves in the non-ideal classical regime

Shock waves are discontinuous solutions to the Euler equations of gasdynamics. Across a shock wave, the mass, momentum and energy conservation are expressed by the well-known *Rankine-Hugoniot relations*, see e.g. Thompson (1988). It is convenient to analyse oblique shocks by resorting to the simplified problem of a *two-dimensional compressive wedge* (Fig. 1.2), which is the simplest geometry imposing a flow deviation which occurs through a shock wave. Indicating with subscripts $(\cdot)_t$ and $(\cdot)_n$ the velocity components in a direction tangential and normal to the

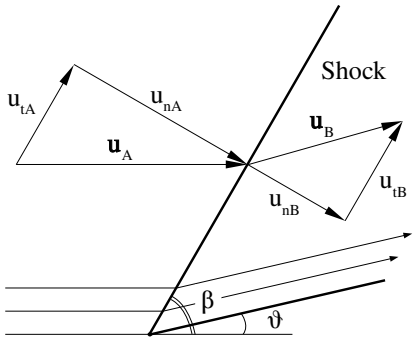

Figure 1.2: Oblique-shock geometry

shock front, by ϑ the flow deviation imposed by the wedge and β the shock angle, the Rankine-Hugoniot relations for two-dimensional flows read:

$$\begin{aligned} \rho_A u_{nA} &= \rho_B u_{nB} \\ u_{tA} &= u_{tB} \\ P_A + \rho_A u_{nA}^2 &= P_B + \rho_B u_{nB}^2 \\ h_A + \frac{u_{nA}^2}{2} &= h_B + \frac{u_{nB}^2}{2} \end{aligned} \tag{1.37}$$

where subscripts $(\cdot)_A$ and $(\cdot)_B$ indicate the pre-shock and post-shock variables, respectively. The above equations can be reformulated as:

$$\begin{aligned} [h] &= \frac{1}{2}[P](v_A + v_B) \\ -[P]/[v] &= (\rho_A \|\mathbf{u}_A\| \sin\beta)^2 \\ \rho_A \tan\beta &= \rho_B \tan(\beta - \vartheta) \\ \|\mathbf{u}_A\| \cos\beta &= \|\mathbf{u}_B\| \cos(\beta - \vartheta) \end{aligned} \tag{1.38}$$

where the notation $[\cdot] = (\cdot)_B - (\cdot)_A$ indicates the jump of a flow variable across the discontinuity.

The *post-shock state* $(P_B, v_B, \mathbf{u}_B, \beta)$ is the one obtained solving system 1.38, complemented with an appropriate EoS giving $h = h(P, v)$, once the pre-shock state and the deviation angle ϑ are selected. The first of eq. 1.38 defines the *Hugoniot locus* $P^{\mathrm{RH}} = P^{\mathrm{RH}}(v; P_A, v_A)$, namely the locus of thermodynamic states that can be connected by a shock wave. The second of eq. 1.38 is the equation of the *Rayleigh line* $P^{\mathrm{R}} = P^{\mathrm{R}}(v; P_A, v_A)$. In a P-v diagram, the Rayleigh line is a straight line connecting the pre-shock and post-shock states. Among the solutions of 1.38, those which are physically admissible must satisfy the entropy inequality:

$$[s] > 0 \tag{1.39}$$

and the *speed-ordering condition* (see Lax (1957) and Oleinik (1959)):

$$M_{nA} \geq 1 \geq M_{nB} \tag{1.40}$$

The latter can be alternatively expressed on a geometrical basis as:

$$\left.\frac{\mathrm{d}P^{\mathrm{RH}}}{\mathrm{d}v}\right|_A \geq \left.\frac{\mathrm{d}P^{\mathrm{R}}}{\mathrm{d}v}\right|_A \quad \text{and} \quad \left.\frac{\mathrm{d}P^{\mathrm{RH}}}{\mathrm{d}v}\right|_B \leq \left.\frac{\mathrm{d}P^{\mathrm{R}}}{\mathrm{d}v}\right|_B \tag{1.41}$$

If the flow deviation angle is lower than the maximum value $\vartheta_{\max}$, then flow compression and turning is attained by means of an attached oblique shock wave. If the deviation angle exceeds $\vartheta_{\max}$, then the flow deviates by means of a detached shock. In the case of an attached oblique shock, either the weak or the strong solutions are possible.

In the positive-Γ region of interest in the present thesis, only compressive shocks are admissible, see e.g. Thompson (1988). Differently from ideal-gas flows, for which the properties of oblique shock waves depend uniquely on the upstream Mach number M_A and on the flow deviation angle ϑ, flows with shock waves described by non-ideal EoS show a more or less noticeable dependence of the post-shock state on the upstream thermodynamic state (P_A, v_A). Moreover, for certain stagnation conditions close to the critical point, so-called *non-ideal shock waves* accompained by a Mach number increase across the shock can occur. This family of admissible non-ideal shock waves in the $\Gamma > 0$ region was recognized for the first time by Gori *et al.* (2017*a*) and Vimercati *et al.* (2017). Non-ideal shock waves slow down and compress the flow. However, the decrease of the speed of sound across the shock—which is a distinctive feature of shock waves occurring in the non-ideal classical regime—causes an increase in the tangential Mach number. For certain inlet conditions, the latter compensates the decrease in the normal Mach number required by shock stability, thus resulting in an increase of the Mach number across the shock.

The turning of a supersonic flow over a wedge can also be achieved in an *isentropic* way, through a smooth variation of the flow properties. In the gasdynamic jargon, the smooth variation is often represented as an infinite number of so-called Mach waves of infinitesimal strength. Depending on the sign of the flow deviation angle ϑ, Mach waves can be either compressive or expansive. The behaviour of a flow undergoing a continuous isentropic turning through an angle ϑ can be determined by integrating the following equation:

$$\mathrm{d}\omega = \sqrt{M^2 - 1}\frac{\mathrm{d}u}{u} = \pm \mathrm{d}\vartheta \tag{1.42}$$

where $\mathrm{d}\omega$ is the exact differential of the Prandtl-Meyer function ω. The differential $\mathrm{d}\omega$ can be expressed as function of the fundamental derivative of gasdynamics, which embeds the dependence on the fluid characteristics and local thermodynamic conditions:

$$\mathrm{d}\omega = \frac{\sqrt{M^2 - 1}}{1 + (\Gamma - 1)M^2}\frac{\mathrm{d}M}{M} \tag{1.43}$$

For a PIG gas, Γ is constant and equal to $(\gamma + 1)/2$, thus the Prandtl-Meyer function depends on the local Mach number only, as it can be found in any textbook of gasdynamics, see e.g. Anderson (2004).

1.3 Thesis outline

The thesis is structured in two main parts. The first part deals with supersonic nozzle flows, both in the ideal and NICFD regimes. Chapter 2 deals with the experimental characterization and numerical simulation of supersonic expansions of pure siloxane vapour MDM in a planar converging-diverging nozzle. Experiments are carried out in the Test Rig for Organic VApors (TROVA), the blow-down wind tunnel of the Laboratory of Compressible fluid-dynamics for Renewable Energy Application (CREALab) of Politecnico di Milano, while numerical simulations are performed using the open-source NICFD solver SU2. Chapter 3 discusses the introduction of a recessed step at the throat section of a planar converging-diverging nozzle as a design solution for fixing the location of the throat, regardless of small variation of process conditions during operation. The analysis is based on experiments and numerical simulations performed using both

dilute dry air and MDM as working fluids. Chapter 4 investigates the influence of nozzle geometry, working fluid molecular complexity and flow non-ideality on the massflow rate discharged by adapted nozzles. An analytical expression for the massflow rate discharged by planar and axisymmetric nozzles is derived, which highlights its dependence on key design parameters. Numerical verification of theoretical results is performed, and guidelines for nozzle design are provided.

In the second part of the thesis, supersonic NICF flows with oblique shocks and rarefaction waves are investigated. An extensive experimental campaign aimed at characterizing oblique shock waves and expansion fans occurring in the non-ideal classical regime is described. In all experiments, the working fluid is siloxane MDM. In Chapter 5, experimental results are reported and commented by resorting to the theoretical formulation of shock waves and expansion fans valid for non-ideal fluid flows. In Chapter 6, all wind tunnel tests discussed in chapter 5 are reproduced numerically, and numerical results are used alongside experimental measurements to comment on the non-ideal nature of the observed flow patterns. Conclusions and recommendations for future work are given in Chapter 7.

Part I

Supersonic nozzle flows

2

Non-ideal expansions of siloxane MDM in supersonic nozzles: wind tunnel tests and numerical simulations

The present chapter discusses the experimental characterization and numerical simulation of supersonic expansions of pure siloxane vapour MDM. Experiments are carried out in the TROVA, the blow-down wind tunnel of the CREALab, Politecnico di Milano. The test section of the wind tunnel is a straight-axis, planar converging-diverging nozzle, designed to discharge a uniform supersonic flow of single-phase vapour MDM at Mach number 1.5*, starting from total conditions* $P^t = 10$ *bar and* $T^t = 277°C$*. In the experiments, total temperature and pressure are measured in the settling chamber upstream of the nozzle, while the flow within the test section is characterized by means of pressure and Mach number measurements. Experimental results are compared with CFD simulations of the flow-field within the TROVA test section. CFD simulations are run using the open-source software SU2, which implements state-of-the-art termodynamic models for NICFD flows. Experimental and numerical results are analyzed in terms of local pressure ratio* P/P^t *and Mach number* M *and compared to predictions based on the PIG model, to provide evidence of the non-ideal nature of the observed flow-fields.*

The structure of the present chapter is the following. Paragraph 2.1 describes the layout and operation of the TROVA test-rig and presents the measurement techniques and instrumentation implemented. The CFD tool used to simulate the experimental runs is briefly presented in paragraph 2.2. Paragraph 2.3 deals with the design of the supersonic nozzle employed in the present experimental campaign. Results are discussed in paragraph 2.4 and concluding remarks are given in Paragraph 2.5.

Part of the contents of this chapter appear in:

Spinelli, A., Cozzi, F., Dossena, V., Gaetani, P., Zocca, M. & Guardone, A. 2016 Experimental investigation of a non-ideal expansion flow of siloxane vapor MDM. In ASME Turbo Expo 2016: Turbomachinery Technical Conference and Exposition

Spinelli, A., Cozzi, F., Cammi, G., Zocca, M., Gaetani, P., Dossena, V. & Guardone, A. 2017a Preliminary characterization of an expanding flow of siloxane vapor MDM. Journal of Physics: Conference Series 821 (1), 012022

Conti, C. C., Spinelli, A., Cammi, G., Zocca, M. & Guardone, A. 2017 Schlieren visualizations of non-ideal compressible-fluid flows. In 13th International Conference on Heat Transfer, Fluid Mechanics and Thermodynamics, HEFAT 2017

Spinelli, A., Cammi, G., Zocca, M., Gallarini, S., Cozzi, F., Dossena, V., Gaetani, P., & Guardone, A. 2017b Experimental observation of supersonic non-ideal compressible-fluid nozzle flows of siloxane MDM. Energy Procedia 129 (Supplement C), 1125–1132

Spinelli, A., Cammi, G., Gallarini, S., Zocca, M., Cozzi, F., Gaetani, P., Dossena, V. & Guardone, A. Experimental evidence of non-ideal compressible effects in expanding flow of a high molecular complexity vapor, Submitted for publication to Experiments in Fluids (2017)

2.1 Experimental set-up

In this section, the experimental setup is briefly described. Paragraph 2.1.1 provides an overview of the layout of and operation of the TROVA wind tunnel. The measurement techniques and instrumentation applied to the characterization of non-ideal flows are described in paragraph 2.1.2. Further details regarding the TROVA test rig, the nozzle design and the measurement techniques can be found in Spinelli *et al.* (2013), Guardone *et al.* (2013), and Spinelli *et al.* (2017*b*), respectively.

2.1.1 The TROVA blow-down wind tunnel

Supersonic expansions of a molecularly complex vapour are characterized experimentally in the TROVA, a blow-down wind tunnel designed to investigate NICFD flows of a wide variety of organic fluids. In the experiments presented here, the wind tunnel is operated with the siloxane compound MDM (octamethyltrisiloxane $C_8H_24O_2Si_3$), which is liquid at room temperature and pressure. With reference to Fig. 2.1, the layout and operation of the plant are briefly outlined.

The TROVA operates as a blow-down wind tunnel, namely, in a discontinuous way, to reduce the thermal power required for vapour production. A specified mass of fluid is charged into the high pressure vessel (HPV). The fluid contained in the HPV is first degased in order to remove non-condensables and then isochorically heated to pressure P_4 and temperature T_4 (point 4) above the nozzle stagnation conditions P_{T6} and T_{T6}. The working fluid contained in the low pressure vessel (LPV) is also degased applying the same procedure and criteria. Since the LPV is kept at room temperature, the working fluid stored in the LPV is at saturation conditions (at room temperature). Indeed, the degasing process is stopped when the saturation pressure of the fluid at room temperature is reached (≈ 5 mbar), to avoid evacuating the working fluid in the vapour phase. The heated section of the plant includes the HPV and the pipeline from the HPV to valve V4, and thus the settling chamber (point 6) and the test section (point 7). The heating system consists of electrical bands and wires externally clung to the heated section of the plant. Operation of the heaters is controlled by Proportional-Integral-Derivative (PID) regulators, which use the wall temperature of the vessel and the pipeline as feedback signal.

Tests are triggered by the opening of the main control valve (MCV), which regulates the feeding total pressure P_{T6} at nozzle inlet and hence the flow rate discharged through the nozzle. In all experiments described in the present chapter, the valve is kept at a fixed 100% opening position, therefore the total pressure upstream of the nozzle is not controlled. This expedient entails the opportunity of exploring a wide variety of thermodynamic states during one single run. Indeed, after the opening transient of about 2 s, the HPV empties and P_{T6} decreases.

Starting from the inlet total conditions P_{T6} and T_{T6}, the fluid is expanded through the nozzle (point 7), where wall pressure measurements and schlieren visualizations are performed. The fluid is finally discharged into a large area pipe (point 8), where it is slowed and brought to the LPV (point 9). The fluid condenses in the LPV and the loop is closed (point 1) by the liquid compression to the HPV (point 2), performed by a membrane metering pump.

The test section is characterized by a modular structure. Among other aerodynamic shapes, it allows to accommodate straight-axis planar converging-diverging nozzles, as it is for the case examined in the present chapter. Specifically, nozzles are made of contoured profiles, which can be easily replaced whenever a different geometry has to be tested. Moreover, the planar configuration of the test section facilitates the implementation of optical diagnostic techniques, such as schlieren visualizations and Laser Doppler Velocimetry (LDV).

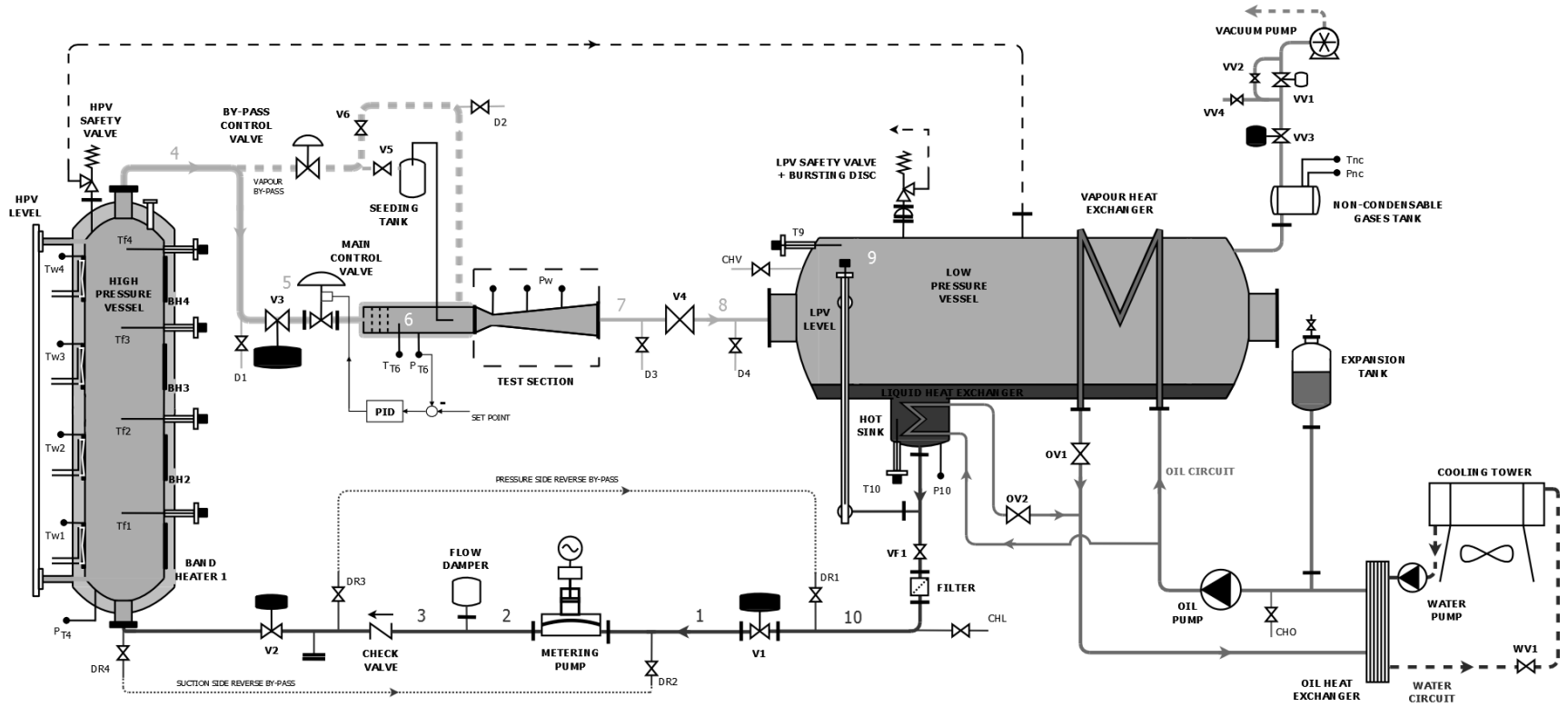

Figure 2.1: Scheme of the complete TROVA test-rig. The total pressure and temperature in the settling chamber are measured by sensors P_{T6} and T_{T6}, respectively. Static pressure taps in the test section are indicated by P_w.

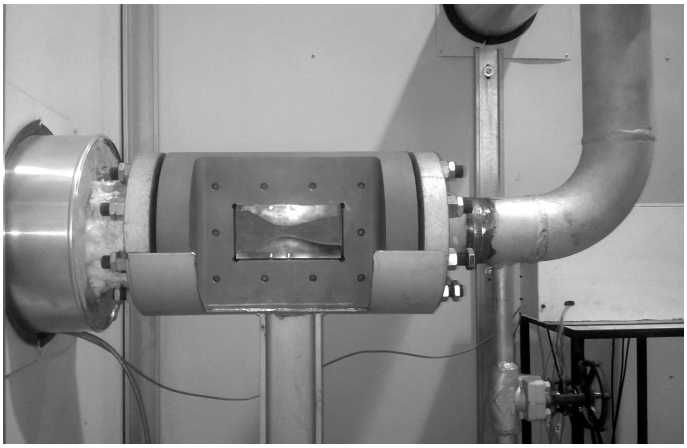

(a)

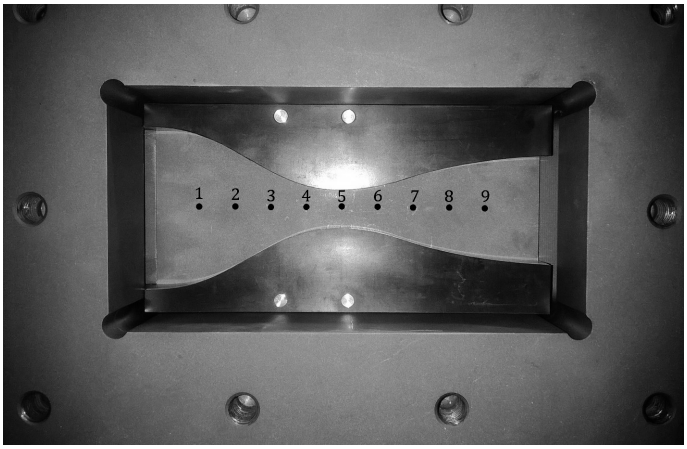

(b)

Figure 2.2: Overview of the TROVA test section (a) and details of the nozzle within the test section (b). Flow direction is from left to right

2.1.2 Measurement techniques and test section instrumentation

In the experiments described in the present chapter, a planar converging-diverging nozzle constitutes the test section of the TROVA wind tunnel. The nozzle is designed according to the procedure presented in Guardone *et al.* (2013). Pressure and temperature measurements and schlieren visualizations are performed to characterize the expansion process bringing the fluid from rest to supersonic speed. Thanks to the modular structure of the test section, the plant can also be operated as a conventional blow-down wind tunnel for the testing of aerodynamic components. In this latter case, the test section is (ideally) a uniform isentropic flow region located downstream of the de Laval nozzle. In the present paragraph, the pressure and temperature measurement system and the layout of the schlieren bench are briefly described.

Piezo-resistive pressure transducers (Kulite XTEH-7L series), with full scale in the range 3.5-40 bar and calibrated both in pressure and temperature in the range 1 bar-FS (full scale) and 25-300 °C, are used to measure static pressures at discrete locations within the flow-field (e.g. along the nozzle axis, at the locations marked with black dots in Fig. 2.2b) and the stagnation pressure in the settling chamber upstream of the nozzle. Due to the very low flow velocity in the settling chamber ($\sim$ 1 m/s), the same arrangement implemented for static pressure measurements is adopted for the

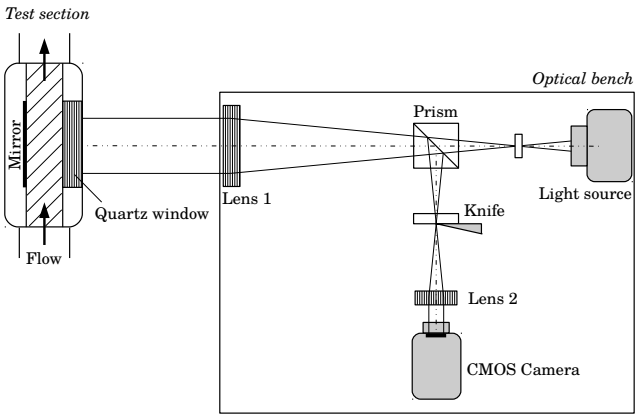

Figure 2.3: Functioning scheme of the double-passage schlieren set-up

measurement of the stagnation pressure P^t. After calibration, an expanded uncertainty of 0.07% of the full scale for all transducers (95% confidence interval) was obtained. Each pressure tap on the nozzle axis is connected to a transducer by a 30 mm-long line-cavity system, followed by a 130 mm^3 capacity ahead of the sensing element. For the line-cavity system, a resonance frequency of the order of 200 Hz was estimated according to the viscous model by Antonini *et al.* (2008), developed for an arbitrary complex system of lines and cavities. To measure the stagnation temperature, the hot junctions of a J-type (Fe - Cu/Ni) and of a K-type (Ni/Cr - Ni/Al) thermocouple are positioned at the symmetry axis of the settling chamber, at the same axial location of the total pressure tap. The diameter of the hot junction is 0.7 mm for the J-type and 0.25 mm for the K-type thermocouple. The time constants of the J-type and the K-type thermocouples, estimated according to the method proposed by Hung *et al.* (2005), are 1.34 s and 0.28 s, respectively. Calibration of thermocouples in the range 25-300 °C results in expanded uncertainties of 1.2 °C (J-type) and 1.0 °C (K-type) on each measured temperature. During an experiment run, pressure and temperature signals are acquired at a sampling frequency of 1 kHz. Since the frequency content of pressure and temperature signals lies below 1 Hz, dynamic compensation is not required. Both pressure transducers and thermocouples provide voltage output signals, which are amplified by an analog signal conditioning system before being sampled and converted to digital ones by a high-speed data acquisition board. A software developed in LabView® environment manages the plant control and the data acquisition.

Schlieren visualizations of the flow within the test section complement pressure and temperature measurements. The front planar wall of the test section is a quartz window allowing for optical access to the flow, while the rear closure is a mirror-polished steel plate. Since optical access is guaranteed only from one side of the test section, the double-passage parallel-light schlieren system sketched in Fig. 2.3 is used instead of the classical Z-type configuration. The emitting and receiving optical components are mounted on the same bench, thus the optical path lies in a plane containing the nozzle axis and a line perpendicular to the nozzle lateral walls (i.e. the front quartz window and the back closure). The light from a 100 W Hg arc-lamp is focused by a F/1.5 silica lens into a circular spot of about 3 mm in diameter and then collimated by the schlieren head (Lens 1 in Fig. 2.3, 150 mm diameter, 1000 mm focal length) perpendicularly to the test section. After traversing the test section, the reflected beam is deflected from the incident one by an amount proportional to the density gradients within the flow in the measurement volume. A cubic beam-splitter (Prism in figure 2.3) separates the light originated by the light source from the

reflected beam and deviates the latter towards the knife edge. The vertical orientation of the knife edge allows to visualize density gradients in the nozzle streamwise direction. The lens indicated as Lens 2 in Fig. 2.3 (52 mm diameter, 75 mm focal length) forms the image of the test section on the sensor of a high-speed CMOS camera. At test start, a digital triggering signal is sent to the camera in order to synchronize the schlieren images with pressure and temperature readings. The camera records the schlieren images at a rate of 20 fps. In order to be synchronized with schlieren images, pressure and temperature data are averaged in packages of 50 points, resulting in a time resolution of 50 ms for the whole dataset. The image resolution is 1936×1216 pixels, the pixel dimension is 5.86 μm, and the exposure time is 1 ms. In all recorded images, the knife is rotated so that darker gray levels are associated to positive density gradients (compressions) and lighter gray levels to negative ones (expansions). Further details on the schlieren setup can be found in Cozzi *et al.* (2015).

Besides providing a visualization of the whole flow-field, schlieren images allow to perform a direct measurement of the local Mach number of the flow. Indeed, the contoured profiles of the test section feature a surface roughness high enough to trigger the formation of Mach waves in the supersonic portion of the domain. As it will be detailed in paragraph 2.4, Mach waves can be detected by the schlieren visualization under certain operating conditions. The slope of the Mach waves with respect to the local flow direction provides a direct measurement of the local Mach number. Along the nozzle axis, the local flow direction lies on the test section longitudinal axis. The line-detection algorithm proposed in Lo & Tsai (1995) is applied to the schlieren frames to determine the slope of the Mach waves μ, which is related to the local Mach number by $M = 1/\sin\mu$. The angular resolution is limited by pixel size. Once one line is identified, the angular expanded uncertainty U_μ (95% confidence level) is computed by assuming a uniform probability distribution within the pixel of the end point location. The angular uncertainty U_μ is determined by the pixel size and by the dimensions of the sub-regions in which the image to be processed is subdivided. Given the angular uncertainty U_μ, the uncertainty U_M of Mach number measurement increases with Mach number. Indeed, the uncertainty propagated to Mach number is

$$U_M = M\sqrt{M^2 - 1}\, U_\mu \tag{2.1}$$

where the term $M\sqrt{M^2 - 1}$ increases almost quadratically with Mach number above $M \approx 1.2$. Therefore, the increased uncertainty is due to the dependence of the Mach number on the Mach line slope μ, through the inverse sine function.

2.2 Numerical method

Throughout the present and the following chapters, experimental results from the TROVA are compared to numerical simulations performed using the open-source NICFD solver SU2. A thorough description of the code structure and capabilities is provided by Palacios *et al.* (2013). Here, the features of SU2 relevant to the simulation of NICFD flows are summarized.

SU2 is an open-source platform for solving multi-physics PDE problems and PDE-constrained optimization problems on general, unstructured meshes, including hexahedral, tetrahedral and hybrid meshes. The core of SU2 is a Reynolds-averaged Navier-Stokes (RANS) solver dedicated to the simulation of compressible, turbulent flows. Thanks to the collaborative effort of a joint research team composed by researchers from Delft University of Technology, Politecnico di Milano, and Stanford University, the code was recently extended to the simulation of NICFD flows with the implementation of state-of-the-art thermodynamic models, as documented by the work of Vitale *et al.* (2015), Gori *et al.* (2015), and Pini *et al.* (2017). The solver was recently validated against experimental data from the TROVA, as documented in Gori *et al.* (2017*b*).

SU2 solves the following system of PDE enforcing mass, momentum and energy equations in conservative form:

$$\frac{\partial \mathbf{U}}{\partial t} + \nabla \cdot \mathbf{F}^c - \nabla \cdot \mathbf{F}^v = \mathbf{Q} \quad \text{in } \Omega,\ t > 0 \tag{2.2}$$

where the vector of unknowns is $\mathbf{U} = (\rho, \rho u_1, \rho u_2, \rho u_3, \rho e^t)^T$, namely the vector of conservative variables, and $\mathbf{F}^c$ and $\mathbf{F}^v$ are the convective and viscous fluxes, respectively. Conservative variables are the fluid density ρ, the total energy per unit mass e^t, and the flow velocity $\mathbf{u} = (u_1, u_2, u_3)$. The latter is expressed in a Cartesian coordinate system. Convective and viscous fluxes are given by:

$$\mathbf{F}_i^c = \begin{pmatrix} \rho u_i \\ \rho u_i u_1 + P\delta_{i1} \\ \rho u_i u_2 + P\delta_{i2} \\ \rho u_i u_3 + P\delta_{i3} \\ \rho u_i h^t \end{pmatrix}, \quad \mathbf{F}_i^v = \begin{pmatrix} \cdot \\ \tau_{i1} \\ \tau_{i2} \\ \tau_{i3} \\ u_j \tau_{ij} + k_{\text{tot}} \partial_i T \end{pmatrix}, \quad i = 1, \ldots, 3 \tag{2.3}$$

where P is the pressure, T is the temperature, h^t is the total enthalpy, δ_{ij} is the Kronecker delta, and τ_{ij} the viscous stresses, which can be written as:

$$\tau_{ij} = \mu_{\text{tot}} \left(\partial_j u_i + \partial_i u_j - \frac{2}{3} \delta_{ij} \nabla \cdot \mathbf{u} \right) \tag{2.4}$$

The total viscosity μ_{tot} and the total thermal conductivity k_{tot} include a molecular and a turbulent contribution.

The formulation of the compressible RANS equations defined by Eq. 2.2, 2.3, and 2.4 enables the use of arbitrary thermodynamic and transport models to express any thermo-physical and transport quantity, namely the pressure P, temperature T, molecular viscosity μ_{mol}, molecular thermal conductivity k_{mol}, and specific heat capacity C_P, as function of density ρ and internal energy e, which in turn can be written as function of the conservative variables:

$$\rho = U_1, \quad e = \rho e^t - \frac{\|\mathbf{u}\|^2}{2} = \frac{U_5}{U_1} - \frac{(U_2 + U_3 + U_4)^2}{2U_1^2}. \tag{2.5}$$

SU2 embeds the vdW and the iPRSV EoS (see paragraph 1.2.1) and provides an interface towards the REFPROP library (see Lemmon *et al.* (2013), Colonna & van der Stelt (2005)), which, among other EoS, includes the state-of-the-art EoS for MDM presented by Thol *et al.* (2017). SU2 does not use the look-up table approach. Instead, all EoS are directly coded.

In the numerical method, convective fluxes are reconstructed by means of an approximate Riemann solver based on the Roe averaging procedure, namely:

$$\left(\mathbf{F}_i^c - \mathbf{F}_j^c \right) = \bar{A} \left(\mathbf{U}_i - \mathbf{U}_j \right), \quad \bar{A} = A(\bar{\mathbf{U}}) \tag{2.6}$$

If a NICFD model is used, the following supplementary condition arises from the spectral decomposition of the Roe's averaged state Jacobian. The supplementary condition reads:

$$\bar{\chi}(\rho_i - \rho_j) + \bar{\kappa}(\rho_i e_i - \rho_i e_j) = (P_i - P_j), \tag{2.7}$$

where $\bar{\chi}$ and $\bar{\kappa}$ are the average of the two thermodynamics quantities defined by:

$$\chi = \left(\frac{\partial P}{\partial \rho} \right)_{\rho e} = \left(\frac{\partial P}{\partial \rho} \right)_e - \frac{e}{\rho} \left(\frac{\partial P}{\partial e} \right)_\rho \tag{2.8}$$

$$\kappa = \left(\frac{\partial P}{\partial \rho e} \right)_\rho = \frac{1}{\rho} \left(\frac{\partial P}{\partial e} \right)_\rho \tag{2.9}$$

According to the PIG model, the condition expressed by Eq. 2.7 is automatically satisfied, since $\chi = 0$ and $\kappa = \gamma - 1$. If instead a NICFD model is used, only one relation (i.e. Eq. 2.7) is provided for the two unknowns $\bar{\chi}$ and $\bar{\kappa}$. In order to uniquely define the Roe-average state, SU2 implements the closure condition proposed by Montagne & Vinokur (1990). Second-order accuracy in the reconstruction of convective fluxes is resolved using a Monotone Upstream-centered Scheme for Conservation Laws (MUSCL) approach by van Leer (1979), with gradient limitation. On the other hand, viscous fluxes are evaluated by averaging the flow variables, flow derivatives, and transport properties at two neighbouring cells, whereas the Thin Shear-Layer approximation reported by Blazek (2005) is employed for gradient calculation. SU2 implements two turbulence models, namely the k-ω SST and the Spalart-Allmaras models presented by Menter (1994) and Spalart & Allmaras (1994), respectively.

Boundary conditions are imposed following the characteristic-based approach presented in Guardone *et al.* (2011) and implemented in the SU2 suite by Vitale *et al.* (2015), which allows to automatically detect inflow/outflow boundaries.

In the present and the following chapters, the SU2 software suite is applied to the simulation of diverse NICFD flows, using both the Euler and the full compressible RANS equations. Numerical simulations are complemented with either the PIG or a non-ideal EoS, including the polytropic vdW and iPRSV EoS, and the SW EoS, in the version proposed by Thol *et al.* (2017). Navier-Stokes simulations adopt either the Spalart-Allmaras or the k-ω SST turbulence model. In the numerical simulation of flows featuring shock waves and expansion fans, an automatic mesh refinement procedure is adoptded, in order to properly resolve flow regions characterized by large gradients, while still using a reasonable amount of grid points in the baseline grid. The mesh adaptation procedure is presented by Dussin *et al.* (2009) and its first application to numerical simulations with SU2 is documented by Gori *et al.* (2017*b*).

In paragraph 2.4, experiments on the supersonic expansion of MDM in the TROVA test section are discussed. Selected test conditions are simulated numerically with SU2 using different EoS and flow models, to provide reference results for the understanding and discussion of experimental data.

2.3 Design of the TROVA nozzle

The TROVA features the typical layout of a supersonic wind tunnel (cf. Fig. 2.1 and paragraph 2.1.1). The fluid is supplied by the high-pressure storage tank and is discharged in a converging-diverging nozzle providing a supersonic flow. Regardless of the layout of the test section adopted for the particular test campaign, the wind-tunnel nozzle must be designed so that it produces a parallel uniform flow at the exhaust section. According to the quasi-one-dimensional model for isentropic nozzle flows (see paragraph 1.2.2 and eq. 1.33), the expansion process occurring in a de Laval nozzle depends on the value of the fundamental derivative of gasdynamics Γ. In the ideal-gas case, the value of Γ is constant and depends only on the fluid characteristics, regardless of process conditions. For NICFD flows, instead, Γ depends on reservoir conditions. The dependence of Γ on reservoir conditions in NICFD flows has the following important consequence on the design and operation of de Laval nozzles in the non-ideal regime. In the ideal-gas regime, nozzles are designed for a particular working fluid and exhaust Mach number. In the non-ideal regime, instead, nozzles are designed for a particular working fluid, exhaust Mach number and reservoir thermodynamic state. The discontinuous operation of the TROVA wind tunnel is such that the high pressure vessel empties during each test, and the total thermodynamic variables measured in the settling chamber change accordingly from thermodynamic states characterized by a high degree of non-ideality to close-to-ideal conditions. As a consequence, the TROVA nozzle, which

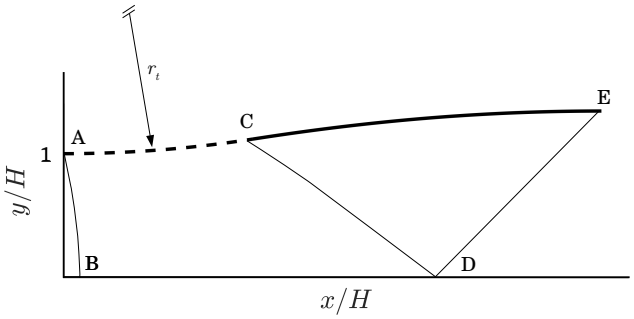

Figure 2.4: Determination of the expansion and turning contours based on the Method of Characteristics

is designed for the wind-tunnel working fluid and for selected exhaust Mach number and total thermodynamic state, mostly works in off-design conditions.

In the following, the design of the supersonic nozzle used to characterize supersonic expansions of MDM in the TROVA is presented. The supersonic portion of the nozzle is designed using the *Method of Characteristics* (MOC) for general fluids implemented by Guardone *et al.* (2013). An overview of the design method is provided, together with an assessment of the influence of the thermodynamic model on the resulting nozzle geometry. Finally, the layout of the test section obtained from the design process is reported.

Following Zucrow & Hoffman (1977), the design of the diverging portion of the nozzle starts from the knowledge of the transonic flow-field in the throat region of the nozzle, computed by solving the transonic perturbation potential equation with the linearized theory of Sauer (1947). The flow equations for the transonic flow in the throat region of a chocked nozzle and the application of the small-perturbation technique of Sauer are described in detail in paragraph 4.1.1. For the purpose of the present discussion, it is worth underlining that the fluid thermodynamics enters the governing equations only through the definition of the speed of sound $c = c(h, s)$, with h the specific enthalpy and s the specific entropy. In the present case of uniform total specific enthalpy h^t and entropy s throughout the domain, the speed of sound is a function of the velocity module $\|\mathbf{u}\|$ only, and the following relation holds: $c^2 = c^2(s, h) = c^2(s, h^t - \|\mathbf{u}\|^2/2) = c^2(\|\mathbf{u}\|^2)$. The solution of the transonic flow-field in the throat region provides the initial data curve for the MOC, which is the locus of points exhibiting a null y-component of the perturbation velocity. Once the initial value line (curve AB in the qualitative plot of Fig. 2.4) is determined, the portion of the divergent geometry immediately downstream of the throat is assigned as a circular arc of nondimensional radius r_t (the normalization length parameter is the height of the wall at the throat section H). The flow-field in this region is completely determined by the inlet conditions and by the assigned wall geometry. The expansion flow-field is governed by the governing equations for two-dimensional irrotational flows, which are solved numerically using the formulation of the MOC by Zucrow & Hoffman (1977), to give, among other flow variables, the distribution of the Mach number along the nozzle axis. The design Mach number is attained at point D of Fig. 2.4. The flow properties along the right-running characteristic CD are determined by interpolation of the flow properties between the two right-running characteristics that intersect the x axis upstream and downstream of point D. Curve AC defines the so-called *expansion region* of the nozzle, i.e. the region in which expansion to the desired Mach number is performed. The portion CE of the divergent is termed *turning region*, since it is devoted to the generation of a parallel uniform flow at nozzle exhaust. In the exhaust flow-field, characteristics are straight lines, whose slope is determined by the exhaust Mach number, namely $\mathrm{asin}(1/M_e)$. The exit section is immediately obtained by requiring

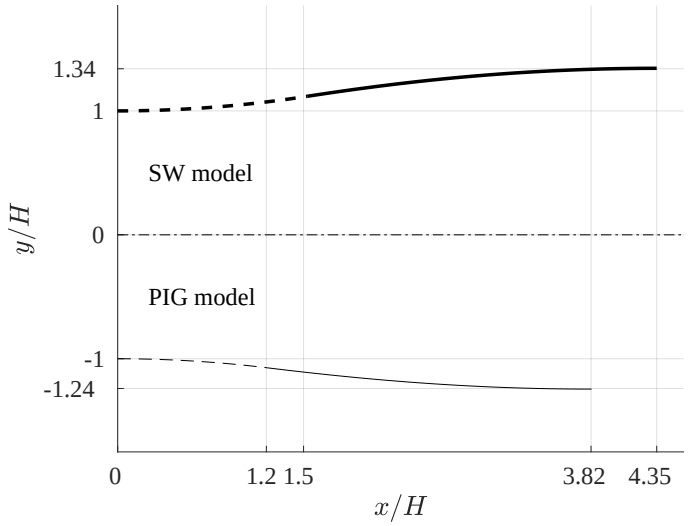

Figure 2.5: Geometry of the diverging portion of the TROVA nozzle resulting from MOC design using SW (thick lines) and PIG (thin lines) models. Design conditions are $P^t = 10$ bar, $T^t = 277$ °C, $\beta = 3.125$ ($M_e = 1.5$)

the massflow rate across line DE to be equal to the massflow rate across the initial value line AB, where E is a straight characteristic drawn from point D, making the angle asin$(1/M_e)$ with the nozzle axis. The turning profile AE is determined by imposing the massflow rate through each discrete characteristic line intersecting the nozzle wall. Further details can be found in Guardone (2011), Guardone *et al.* (2013).

The design operating condition of the TROVA nozzle is defined by total conditions $P^t = 10$ bar, $T^t = 277$ °C and by a total to ambient pressure ratio $\beta = P^t/P_a = 3.125$, which corresponds to an exhaust Mach number (from quasi-1D flow theory) of $M_e = 1.5$. The diverging portion of the nozzle is designed using the procedure presented so far. The resulting geometry is shown in Fig. 2.5. The expansion and turning regions are represented with dashed and solid lines, respectively. For both geometries, pressure P, Mach number M, speed of sound c, and fundamental derivative of gas dynamics Γ along the axis of the diverging duct are reported in Fig. 2.6. In Fig. 2.5 and Fig. 2.6, results obtained using the SW model are compared to results obtained using the PIG model. In the PIG calculations, the specific heat ratio γ is evaluated in the dilute gas limit, giving $\gamma = 1.017$ for MDM. Finally, Fig. 2.7 shows the streamlines and the pressure field computed using the SW model. In all plots, spatial coordinates are normalized with respect to the height of the profile at the throat H. Figure 2.5 clearly shows that the two geometries obtained using the SW and PIG models are different in terms of nozzle length and exit area. Indeed, the expansion occurs in a thermodynamic region in which the fundamental derivative of gasdynamics, calculated using the SW model, is always lower than the corresponding perfect-gas value (Fig. 2.6a). Moreover, $\Gamma < 1$ throughout the diverging portion, and the SW model predicts a speed of sound increasing along the isentropic expansion (Fig. 2.6b). A justification for the differences between the SW and PIG nozzle geometries is provided by the quasi-one dimensional theory, and specifically by the equations relating the gradients of the flow variables to the area gradient. One of those equations, namely the last of Eq. 1.33 is reported here for convenience:

$$\frac{1}{M}\frac{dM}{dx} = \frac{1+(\Gamma-1)M^2}{M^2-1}\frac{1}{A}\frac{dA}{dx}$$

In the thermodynamic region of interest here, the term multiplying the area gradient is always greater for the PIG case (Γ is constant and equal to 1.0087) than for the non-ideal case. This

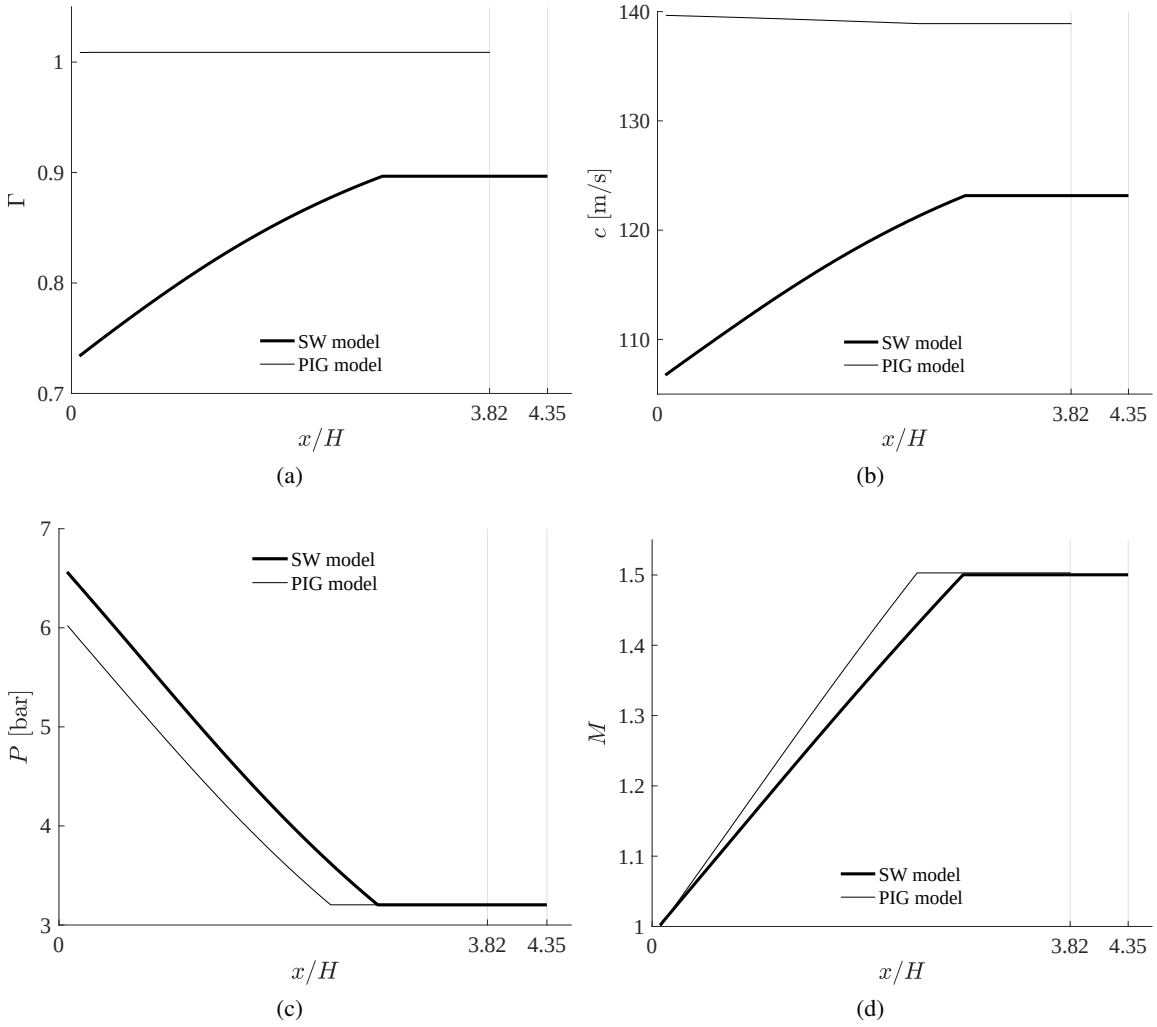

Figure 2.6: (a) Fundamental derivative of gasdynamics, (b) Speed of sound, (c) Pressure, and (d) Mach number distribution along the symmetry axis of the TROVA nozzle, for the two designs perfomed with the SW (thick lines) and PIG (thin lines) models.

implies that the Mach number gradient $\mathrm{d}M/\mathrm{d}x$ in the non-ideal gas case is lower than that obtained in the perfect-gas case, thus resulting in a lower area gradient $\mathrm{d}A/\mathrm{d}x$ (or, in other words, in a longer nozzle). The influence of the fluid molecular complexity and of the thermodynamic model employed in the design of the supersonic portion of the nozzle is analyzed in detail in the works by Guardone (2010) and Guardone *et al.* (2013), which report results of nozzle design for different working fluids.

Despite differences between the geometries resulting from the PIG and SW models, the pressure and Mach number profiles of Fig. 2.6c and Fig. 2.6d reveal that, in both cases, the design pressure ratio is attained and the Mach number is uniform at nozzle exhaust. The streamlines reported in the top portion of Fig. 2.7 show that the flow at the exhaust section is parallel to the nozzle axis.

For the TROVA nozzle, the exhaust pressure in design conditions is 3.2 bar. However, due to the extremely low initial pressure within the LPV (< 10 mbar), and the large HPV-to-LPV capacity ratio (about 6), the test section operates in under-expanded conditions during the entire

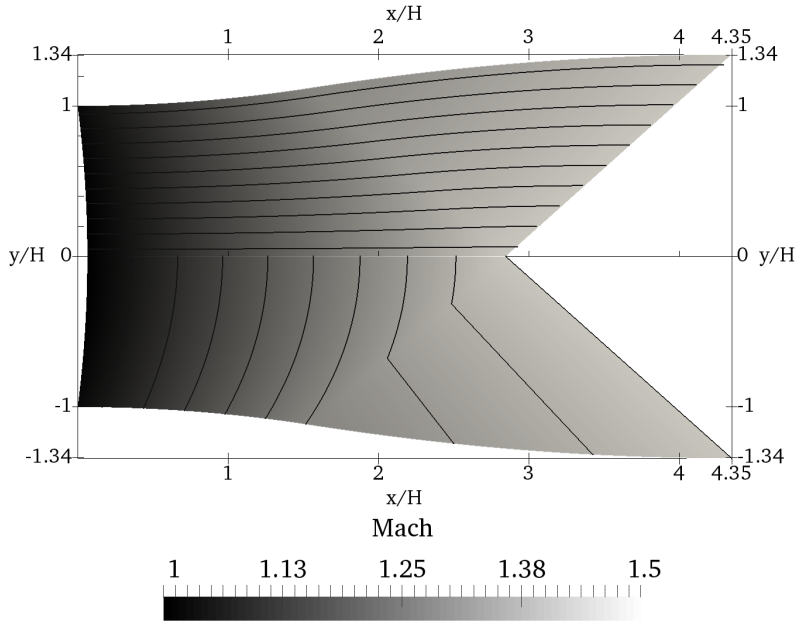

Figure 2.7: Mach number distribution in the diverging portion of the TROVA nozzle (grayscale contour), as resulting from MOC design using the SW model. Streamlines (top) and selected Mach number isolines (bottom) are superimposed to the Mach number distribution

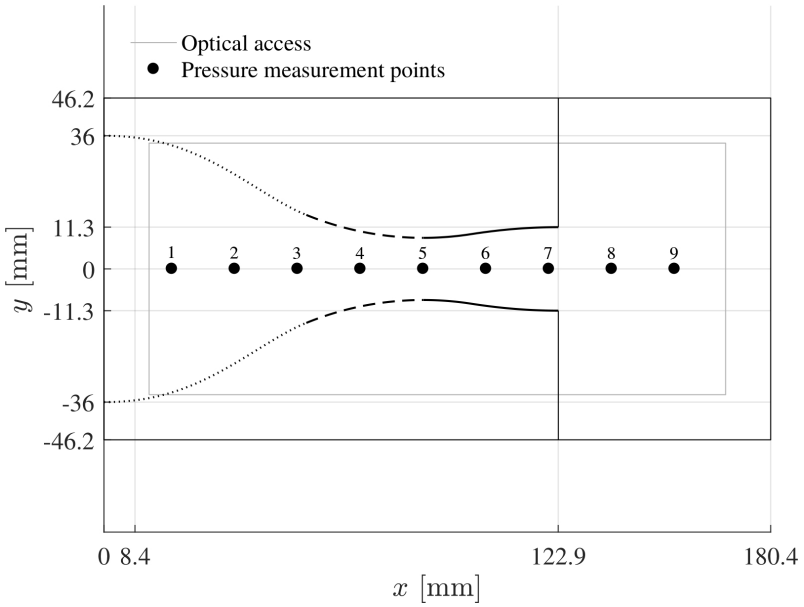

Figure 2.8: Layout of the TROVA test section in dimensional units

test. This mode of operation does not affect the flow-field inside the nozzle, which is described by the isentropic adapted-flow solution.

Once the non-dimensional geometry of the diverging portion of the nozzle is determined, an appropriate scaling of the geometry based on the throat half-height H is performed and a converging portion is designed. The nozzle must fit the dimensions of the TROVA test section and (at least) the diverging portion must be optically accessible for schlieren visualizations. Static pressure is measured along the nozzle axis, and distance between pressure taps is imposed by

run ID	P^t	T^t	P_r^t	T_r^t	Z^t	β	M_e
1-1	4.59	239	0.32	0.91	0.81	3.34	1.55
2-1	9.20	268	0.64	0.96	0.63	3.12	1.50

Table 2.1: Operating conditions for reference experiments at test start. Pressures are expressed in bar, temperatures in °C.

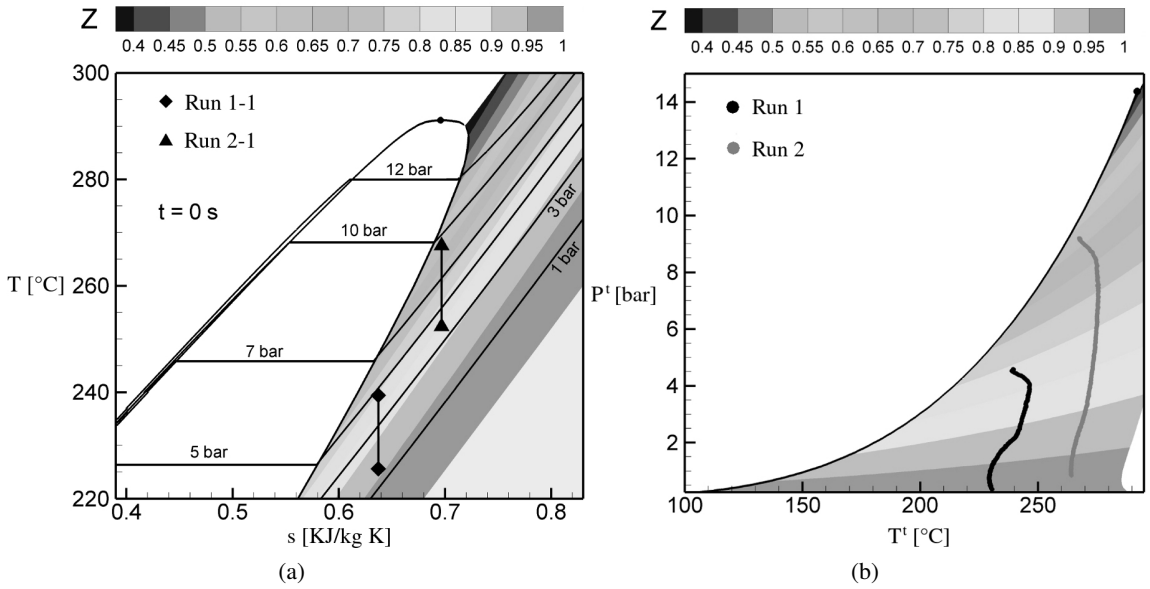

Figure 2.9: (a) Steady, isentropic expansion processes in the T-s diagram. (b) Time evolution of the inlet conditions (P^t, T^t) in the P-T diagram. Operating conditions at test start are reported in Tab. 2.1

the dimension of sensors. In order to properly characterize the expansion process, one pressure measurement point is conveniently placed at the geometrical throat, at least one pressure tap in the expansion region (indicated as BD in Fig. 2.4) and one pressure tap in the uniform region from point D of Fig. 2.4 to the exhaust section. Figure 2.8 shows the final layout of the test section of the TROVA. The nozzle is 122.9 mm long, with a width of 18.7 mm in the direction perpendicular to the contoured profile. The height at the geometrical throat H is 8.4 mm, which gives a throat area of 314.16 mm^2 (20 mm equivalent diameter). The height of the profile at the exit section is 11.3 mm, which results in a exit-to-throat area ratio of 1.35. The converging portion is a 5$^{\text{th}}$-order polynomial curve (dotted line in Fig. 2.8), matched smoothly with a circular arc of radius 84 mm at the throat (dashed line in Fig. 2.8), i.e. ten times H ($r_t = 10$). In chapter 4, the influence of both the nozzle geometry and the reservoir conditions on the nozzle throat flow and of the discharge coefficient will be duly discussed. The plot also reports the optically accessible region and pressure measurement points along the nozzle axis. In Fig. 2.8, the black dots marking the position of pressure taps are not to scale, namely they do not represent the actual dimension of pressure taps, whose diameter is 0.3 mm.

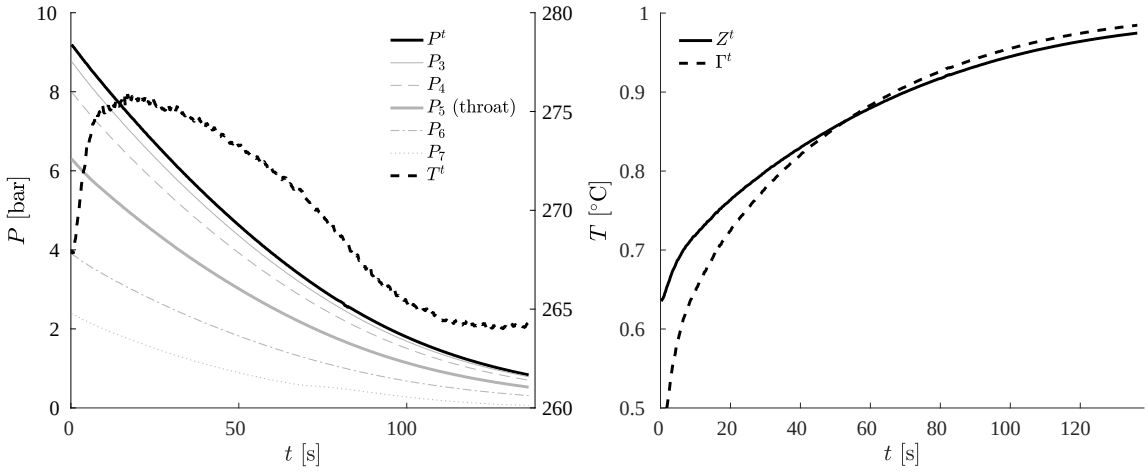

(a) (b)

Figure 2.10: Time trends of measured P^t , T^t and P, and of Z^t and Γ^t calculated using the SW model. At t = 0s, test conditions are those labelled as run 1-1 in Tab. 2.1

2.4 Results and discussion

Several wind-tunnel tests were performed to study the expansion of MDM vapour in a supersonic nozzle (Fig. 2.8). Subcritical and slightly superheated inlet total states were examined, which all feature $\Gamma < 1$. In tests performed at moderately non-ideal states, total conditions are $P^t \approx 4.5$ bar ($P_r^t = P^t/P_c = 0.31$) and $T^t \approx 240$ °C ($T_r^t = T^t/T_c = 0.91$), where P_c and T_c denote critical pressure and temperature of MDM. In total conditions, the compressibility factor, defined as $Z = Pv/RT$, is $Z^t \approx 0.8$. For tests at higher non-ideal conditions, total conditions are $P^t \approx 9$ bar ($P_r^t = 0.63$) and $T^t \approx 270$ °C ($T_r^t = 0.96$), with compressibility factors $Z^t \approx 0.6$. Compressibility factors are calculated using the SW model.

Two tests selected within the overall experimental campaign are discussed in detail in this chapter. Table 2.1 summarizes the operating conditions at test start (t = 0 s), which correspond to the minimum value of the compressibility factor in the stagnation state Z^t. The two selected tests feature moderate (run 1-1) and high (run 2-1) level of flow non-ideality.

For the two analyzed tests, Fig. 2.9a depicts, in the T-s diagram, the steady-state, isentropic expansion processes occurring within the nozzle at time t = 0 s, while Fig. 2.9b shows, in the P-T chart, the time evolution of the inlet condition (P^t, T^t) during each test, clarifying that as P^t reduces, Z^t increases and ideal conditions are approached as the reservoir empties. Also, the extent of the thermodynamic region explored during a single test can be appreciated, as well as the proximity to the saturation curve. The specific entropy s is calculated from the measured values of total pressure and temperature using the SW model.

Figure 2.10a shows the time evolution of the total temperature, and of total and static pressures. The latter are labeled according to the corresponding tap number (cf. Fig. 2.8). The test lasts approximately 140 s. All pressure values decrease in time due the emptying of the HPV, while the pressure along the nozzle reduces as the vapor expands. Contrarily, the total temperature does not display the expected monotonically decreasing behaviour. This is possibly due to non-uniformity of the temperature within the HPV and in the heated pipe upstream of the plenum. Figure 2.10b reports the evolution of the compressibility factor Z^t and of the fundamental derivative of gasdynamics Γ^t at total conditions. Both values are initially well below one and monotonically increase throughout the test, indicating that the nozzle is fed at conditions of decreasing non-ideality until

run ID	P^t	T^t	Z^t
1-5	0.52	230	0.98
2-5	0.84	264	0.98
3-5	0.30	233	0.99
4-5	0.60	263	0.98
5-5	0.22	263	0.99
6-5	0.89	263	0.97

Table 2.2: Test conditions considered for consistency analysis. Pressures are expressed in bar, temperatures in °C.

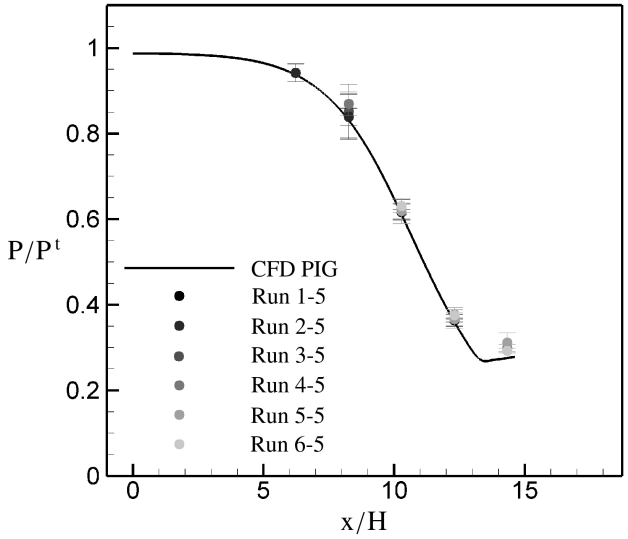

Figure 2.11: Pressure ratio P/P^t trends along the nozzle axis for test conditions reported in Tab. 2.2.

the ideal-gas state is approached at the end of the test.

With reference to Fig. 2.10, at each time instant during the test run, a different dataset including total temperature, total and static pressures and schlieren images is acquired. Since the characteristic time of the emptying of the high-pressure reservoir $\Delta t_{\text{reservoir}}$ is more than two orders of magnitude greater than the flow residence time in the de Laval nozzle Δt_{nozzle} (see Spinelli *et al.* (2013)) and the latter, in turn, satisfies $\Delta t_{\text{nozzle}} \ll \tau$, where τ is the thermodynamic relaxation time associated to the expansion of vapour MDM within the supersonic nozzle (see Thompson (1988) and Colonna *et al.* (2007)), each dataset is considered as a steady-state representation of the flow-field. Throughout the chapter, datasets are labelled as run i-j, where i identifies the test run and j the flow conditions attained at different time instants during the test.

In the following, results on nozzle expansion flows are discussed by analyzing the profiles of the pressure ratio P/P^t and, for the diverging portion only, of the Mach number M along the nozzle axis. Since both quantities are available from experimental measurements, they can be evaluated without the introduction of inaccuracies other than the instrument uncertainty. Furthermore, they significantly characterize isentropic nozzle flows. According to the PIG model, their trend is fixed once the fluid and the nozzle geometry are given, thus any depart from the PIG behaviour not ascribable to measurement uncertainties provides evidence of the non-ideal nature of the flow.

Consistency of experimental measurements is checked over six operating conditions attained

Low-Z^t test					
	run 1-1	run 1-2	run 1-3	run 1-4	run 1-5
P^t	4.59	3.96	2.69	1.29	0.52
T^t	239	246	243	231	230
Z^t	0.81	0.85	0.90	0.95	0.98
High-Z^t test					
	run 2-1	run 2-2	run 2-3	run 2-4	run 2-5
P^t	9.20	8.51	6.23	3.27	0.84
T^t	268	274	275	271	264
Z^t	0.63	0.70	0.80	0.90	0.98

Table 2.3: Total termodynamic states and compressibility factors for reference experiments.

in six different tests, to assess test repeatability. Due to the expected dependency of the nozzle flow on the inlet flow conditions, each run (i.e. the j-th condition attained in the i-th test) represents a single realization of the state (P^t, T^t) and of the set of pressures P measured along the nozzle axis, even if conditions with equal Z^t are considered. For this reason, test repeatability cannot be assessed rigorously. In order to minimize the influence of non-ideal effects on the P/P^t reported for comparison, pressure ratios corresponding to the maximum value of the compressibility factor attained during each test are considered. Test conditions are reported in Tab. 2.2 and experimental points are shown in Fig. 2.11. The measured pressure ratios lie within the error bars from one another, thus proving the consistency of the experimental data acquired during different experimental runs. Figure 2.11 also reports the result of a steady two-dimensional Navier-Stokes simulation, performed in the PIG hypothesis. The constant specific heat ratio is $\gamma = 1.018$, as obtained in the temperature range of interest for the presented experiments, according to Span (2000). The computational domain considered for the CFD simulations reported in the present chapter is limited to the converging and diverging sections of the nozzle. The computational grid is quadrilateral and it is made of 35 340 elements and 35 750 points. The conditions of the fluid at the inlet boundary reproduce the measured total conditions P^t and T^t. A supersonic outlet flow is set at the nozzle exhaust section, namely an arbitrarily low pressure value is imposed.

Detailed results obtained for the two tests representative of the whole experimental campaign are now gathered and discussed, at variable non-ideal conditions. Schlieren visualizations are reported, alongside pressure ratios P/P^t and Mach number M measured along the nozzle axis. Flow conditions at nozzle inlet at different time instants during the tests are reported in Tab. 2.3.

Figure 2.12 reports schlieren visualizations of the flow-field in test conditions of Tab. 2.3. It is worth recalling here that the schlieren arrangement is such that darker gray levels identify positive density gradients, lighter gray levels negative ones. The contoured nozzle profiles exhibit an enhanced roughness, in order to promote Mach waves formation, which are indeed well visible in the diverging portion of the nozzle. Consistently, the nozzle core flow is isentropic, as it is confirmed by the evidence that the flow is under-expanded. Indeed, the nozzle outlet section is optically accessible and the post-expansion is evidenced by the expansion fans and the slip lines visible at the nozzle exit. Overall, schlieren images are considerably dark, especially in the throat region, where maximum density gradients are attained. Moreover, in the reported frames, expansion fans appear as dark regions instead as bright.

Conti *et al.* (2017) analyzed the optical path in the TROVA schlieren set-up described in paragraph 2.1.2 by means of a ray tracing algorithm. The study revealed that light rays crossing

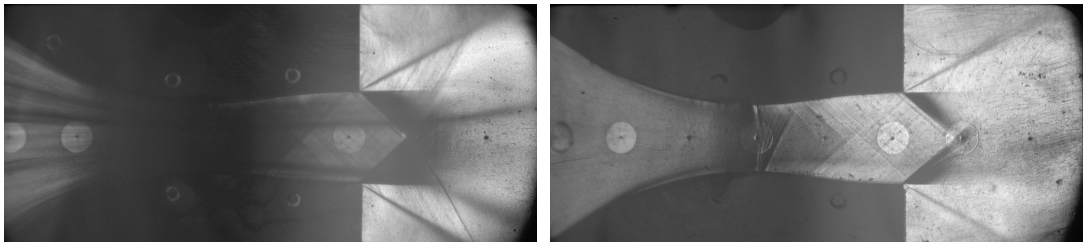

(a) run 1-1

(b) run 2-1

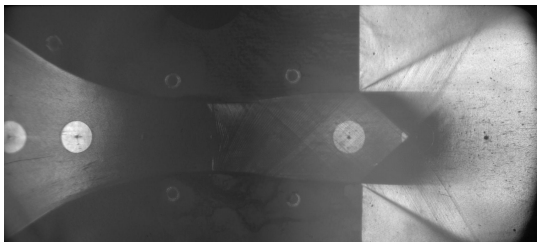

(c) run 1-2

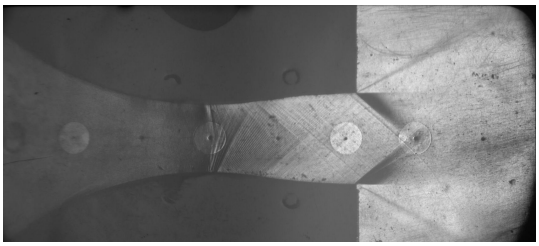

(d) run 2-2

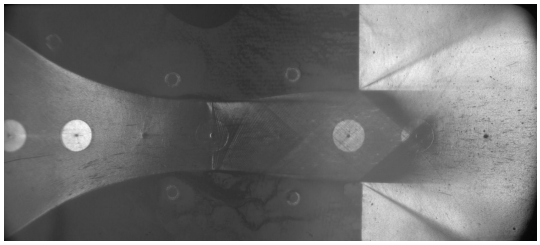

(e) run 1-3

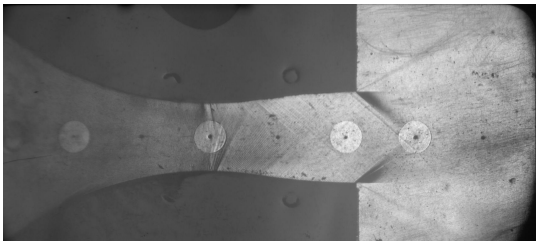

(f) run 2-3

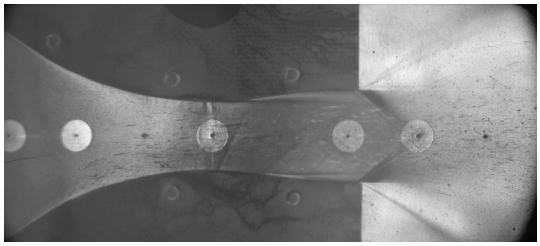

(g) run 1-4

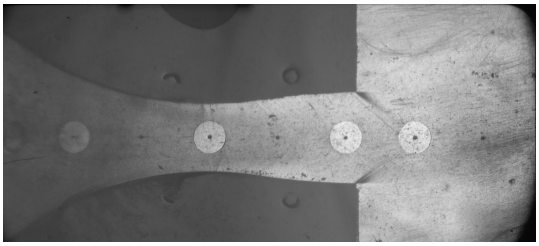

(h) run 2-4

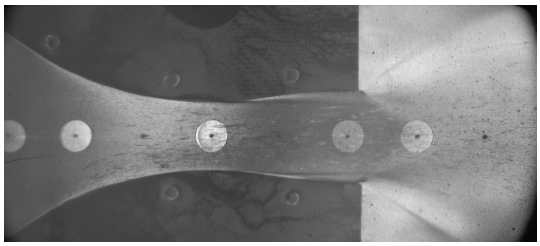

(i) run 1-5

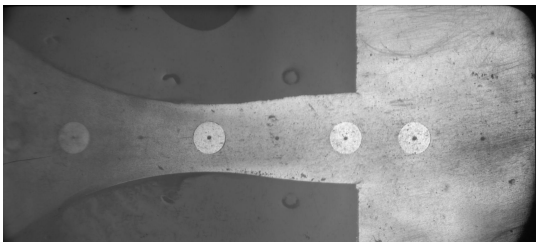

(j) run 2-5

Figure 2.12: Schlieren visualizations of the flow field in test conditions reported in Tab. 2.1 and 2.3

regions of the flow domain characterized by stronger density gradients are deviated outside the measuring range, thus they do not reach the camera sensor. As tests proceed towards more dilute conditions, the influece of these measuring range issues progressively reduces and the images become less dark. This latter phenomenon, namely the reduced influence of measuring range issues at approaching dilute conditions, can be explained by resorting to the fundamentals of the schlieren measurement technique. Schlieren visualizations are sensitive to the refractive index gradient along the nozzle axis (x-direction). Specifically, deflection of light rays is proportional to $\partial n/\partial x$, with n the refractive index. The refractive index gradient can be expressed using the Gladstone-Dale relation (see Tropea *et al.* (2007) for reference) as:

$$\frac{\partial n}{\partial x} = K\frac{\partial \rho}{\partial x}, \tag{2.10}$$

where ρ is the fluid density and K is a quantity depending on fluid properties, which keeps constant along the x axis. Validity of the Gladstone-Dale relation for nozzle flows of MDM was checked by Conti *et al.* (2017), which estimated $K_{\mathrm{MDM}} = 4.30 \cdot 10^{-4}$ m^3/kg. For an the isentropic expansion occurring in the nozzle, the refractive index gradient can be conveniently rewritten highlighting the compressibility ($1/c^2$) and the pressure ratio along the nozzle, as:

$$\frac{\partial n}{\partial x} = K\frac{1}{c^2}P^t\frac{\partial (P/P^t)}{\partial x} \tag{2.11}$$

Total conditions at nozzle inlet, which appear at right hand side of the above equation, play a direct role in determining the refractive index gradient through the value of P^t and also have an indirect impact because they determine the extent of non-ideal gas effects, since they affect both compressibility and the gradient of the pressure ratio along the nozzle axis. At progressing testing time, the variation of compressibility $1/c^2$ and of the gradient $\partial(P/P^t)/\partial x$ are significantly lower then the variation of the value of P^t. It can therefore be concluded that, although non-ideal gas effects do have an impact, the most important parameter in determining the different values of the refractive index gradient, and thus the extent of the measuring range issues during the test, is total pressure. When the total thermodynamic state approaches dilute conditions at the end of a test, the refractive index gradient attains its lowest value. Accordingly, deviation of light rays reduces so as to fall into the measuring range.

Figure 2.13 reports the local pressure ratio P/P^t measured at the active taps at different Z^t, in test conditions reported in Tab. 2.3. Only four taps were used, in the region of higher pressure gradients. For plot clarity, uncertainty bars are reported only for the experiment carried out at the highest level of non-ideality (see Fig. 2.13b). Expanded uncertainty (95% confidence interval) for the pressure ratio was calculated by propagating the uncertainties of measured P and P^t. As a reference, the continuous expansion profiles obtained from a two-dimensional Navier-Stokes simulation using the PIG model is reported. The constant specific heat ratio is $\gamma = 1.018$. Consistently, CFD results agree well with data measured at the maximum Z^t, namely close to dilute conditions.

Together with experimental points, calculated distributions of the compressibility factor Z at the measuring points are reported in Fig. 2.14 in order to point out the non-ideal effect pertaining to each condition analyzed. Compressibility factors along the nozzle axis are calculated assuming a steady isentropic expansion within the nozzle. Uncertainties for the compressibility factor are calculated by applying the Monte Carlo method reported by (JCGM-WG1 (2008)), in order to propagate uncertainties of measured P, P^t and T^t to the functional relation $Z = Z(P, s(P^t, T^t))$, expressed using the SW thermodynamic model. Note that no uncertainty in the thermodynamic model is accounted for. Figure 2.14 clearly show that the level of Z increases for the whole flow field as operating conditions become more ideal (increase of Z^t); furthermore, Z increases as the

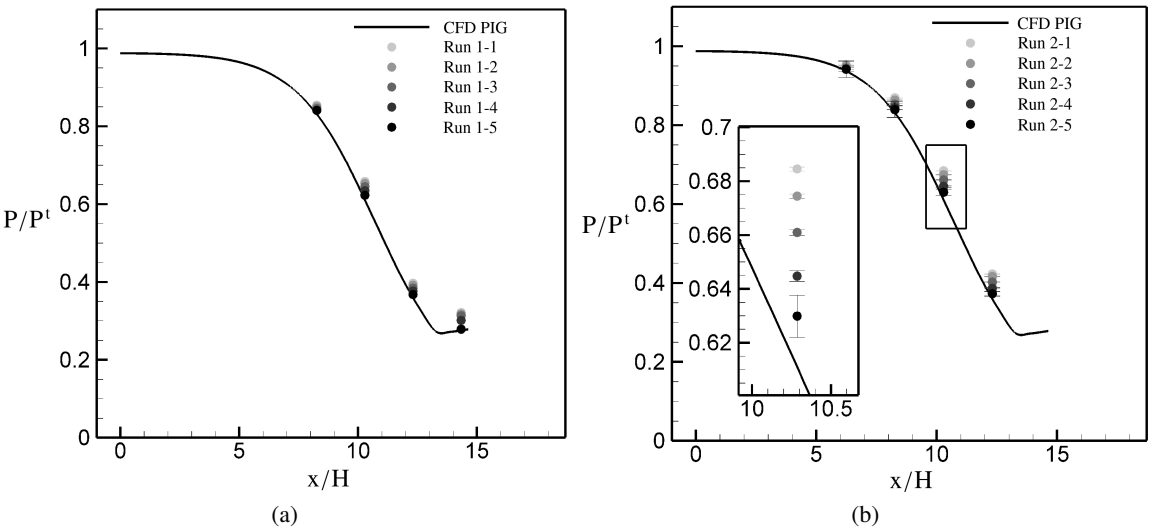

Figure 2.13: Local static to total pressure ratios P/P^t for test conditions reported in Tab. 2.3. For run 2 (b), a detail view of the throat region is provided. CFD results from PIG simulations are reported for reference

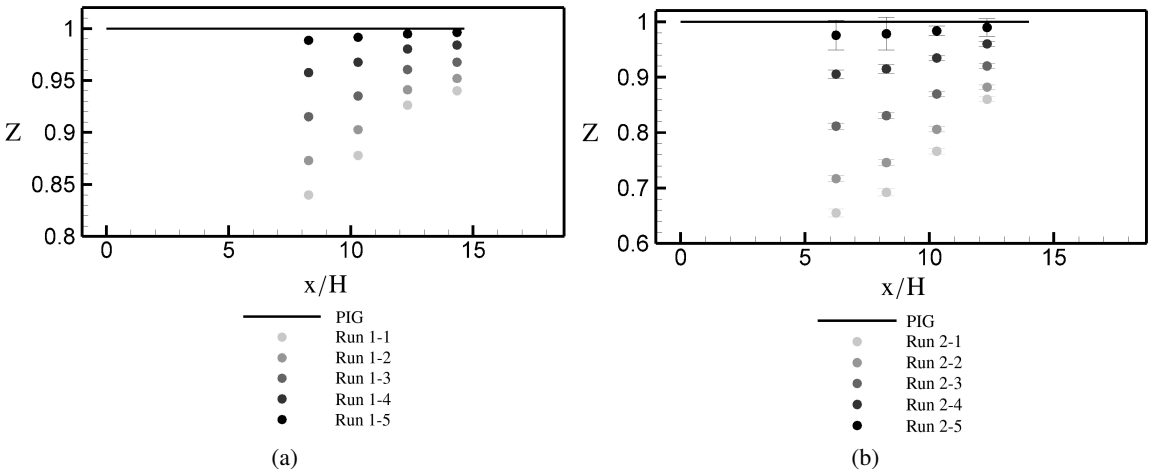

Figure 2.14: Compressibility factors for test conditions reported in Tab. 2.3. The PIG value of the compressibility factor ($Z = 1$) is reported for reference

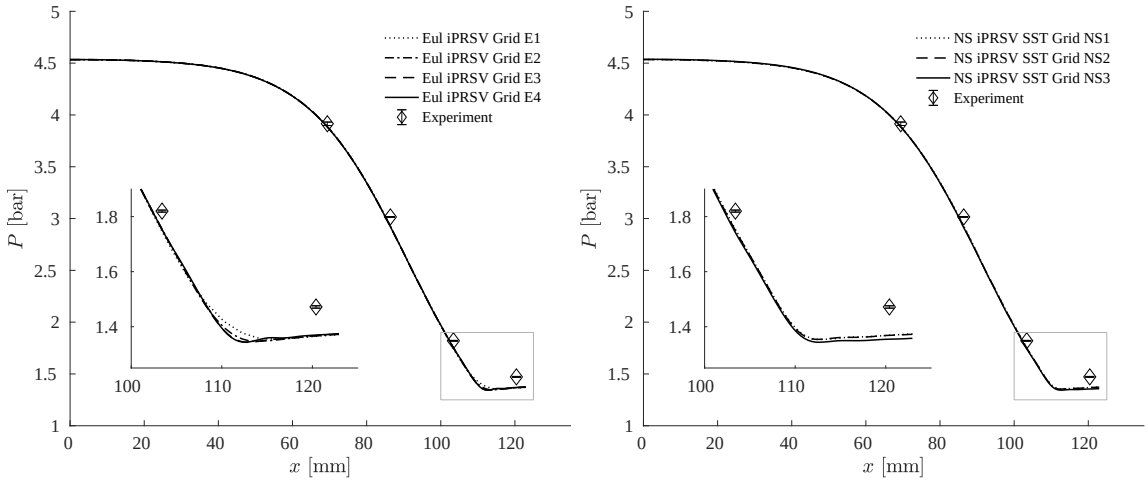

Figure 2.15: Grid convergence results for (a) inviscid and (b) viscous simulations. The computed pressure profiles along the nozzle axis is compared to experimental data. Operating conditions are identified as run 1-1 in Tab. 2.1

expansion proceeds along the nozzle, and approaches unity at the outlet. The rather obvious result of constant $Z = 1$ from the PIG model is plotted for reference.

In the remainder of the chapter, experimental data are compared to numerical simulations of nozzle flows using non-ideal EoS. The flow condition labelled as run 1-1 in Tab. 2.1 is chosen here as reference to assess the suitability of a set of numerical models to the simulation of the flow-field within the TROVA nozzle in the NICFD regime. CFD simulations use both the Euler and the full Reynolds-averaged compressible Navier-Stokes equations, complemented with the iPRSV EoS and with the SW EoS by Thol *et al.* (2017). Results of viscous simulations are reported for two different turbulence models, namely the k-ω SST and the Spalart-Allmaras (SA) turbulence models. For the planar nozzle geometry of interest in the present investigation, two-dimensional simulations are considered to be sufficient to capture the flow behavior at the middle section of the wind tunnel, where the interaction with the sidewall boundary layer is expected to be negligible, as documented by Gori *et al.* (2017*b*).

A grid dependence study on the pressure along the nozzle axis is presented first. Inviscid simulations are run over four triangular grids referred to as grid E1 (516 elements and 307 points), grid E2 (1 969 elements and 1 081 points), grid E3 (7 607 elements and 3 995 points) and grid E4 (29 860 elements and 15 310 points) using the iPRSV EoS, and viscous simulations are run over three quadrilateral grids referred to as grid NS1 (16 988 elements and 17 250 points), grid NS2 (35 340 elements and 35 750 points), and grid NS3 (80 223 elements and 80 840 points) using the iPRSV EoS and the k-ω SST turbulence model. Results are reported in Fig. 2.15, in which the pressure trends computed along the nozzle axis are compared to experimental data. No significant differences are observed among the pressure profiles computed using the different grids, though minor discrepancies are observed close to the exhaust section. This suggests that an adequate level of grid resolution was reached and that the solution does no longer depend on the spatial resolution of the grid. Results presented in the remainder of the chapter are obtained from Euler simulations run over the E3 grid and from Navier-Stokes simulations run over the NS2 grid.

The effect of the thermodynamic model on the computed pressure profiles is then studied by comparing the results of Euler simulations using the PIG, iPRSV and SW EoS, as shown in

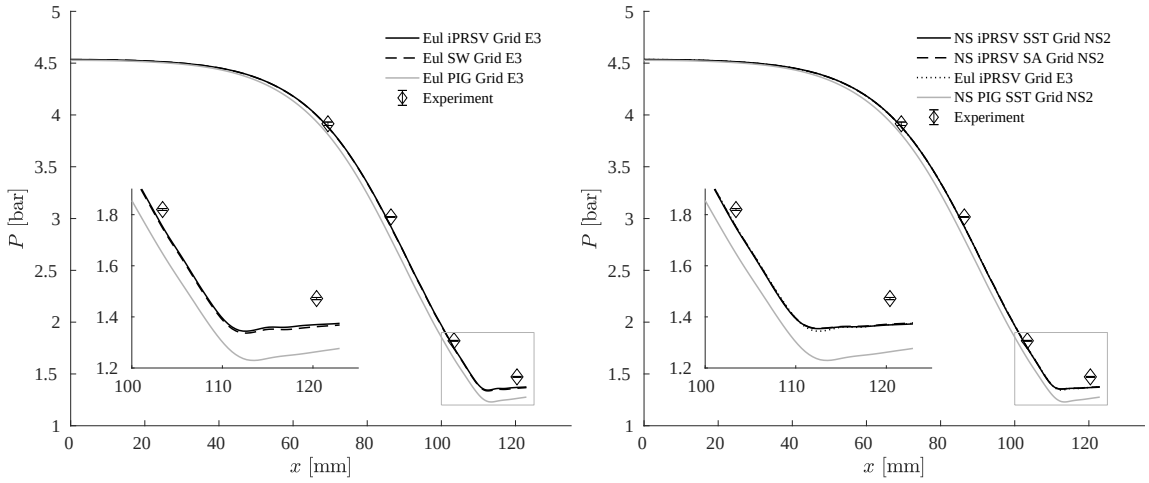

(a) (b)

Figure 2.16: Effect of thermodynamic (a) and turbulence (b) modelling on the computed pressure profile along the nozzle axis. Experimental data are reported for comparison. Operating conditions are identified as run 1-1 in Tab. 2.1

Fig. 2.16a. The iPRSV and SW EoS produce similar results that better represent the measured pressure profile, thus confirming the need of including complex thermodynamic models in CFD simulations to represent NICFD flows properly. Results reported in Fig. 2.16b show instead the influence of turbulence modelling on the computed pressure profiles. Navier-Stokes simulations run using the iPRSV EoS and both the k-ω SST and the Spalart-Allmaras turbulence models are reported and compared to an Euler simulation using the same thermodynamic model and to a Navier-Stokes simulation using the k-ω SST turbulence model and the PIG EoS. Currently, only the Spalart-Allmaras turbulence model is available in SU2 if the SW EoS is used for Navier-Stokes simulations, thus no comparison between results of different turbulence models can be drawn if the SW EoS is adopted. Results of Fig. 2.16b clearly show that the influence of the EoS on the computed profile is dominant with respect to the influence of viscosity and of the turbulence model. Final remarks concern the computational time. An Euler simulation on the E3 grid using the iPRSV EoS takes 9s on 12 Cores of Intel Xeon CPU X5650, 2.67 GHz. On the same architecture, an Euler simulation on the E3 grid using the SW EoS takes 34m 18s. This relevant difference in computational time is mostly due to the fact that, while the iPRSV is directly coded in SU2, the SW EoS is implemented in the RefProp library and called by SU2 through an interface software. The Navier-Stokes simulations run on the NS2 grid using the Spalart-Allmaras turbulence model and the iPRSV and SW EoS take 22m 9s and 23h 36m 27s, respectively. For comparison, Euler and Navier-Stokes simulations on the same grids using the PIG EoS take 8s and 18m 24s, respectively.

For test conditions defined by run 1-1 in Tab. 2.1, an Uncertainty Quantification (UQ) analysis is performed, with the aim of quantifying the statistical variability of the pressure profile along the nozzle axis due to both aleatory and epistemic uncertainties. Aleatory uncertainties include the uncertainties on measured values, and are due to the fact that it is impossible, in practice, to retrieve the exact state of the fluid through measurements. Epistemic uncertainties account for approximations made in the mathematical model of the flow, due to a lack of knowledge of the physics of the problem. Experimental uncertainties, expressed as Gaussian probability distribution functions, are propagated through the CFD code, in order to compare numerical and experimental

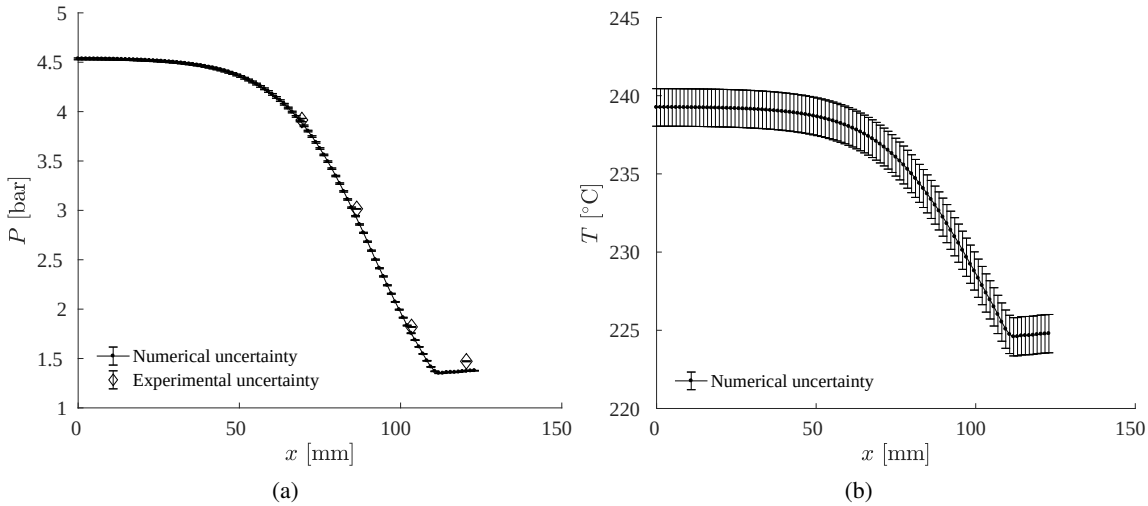

(a) (b)

Figure 2.17: Comparison of experimental and numerical error bars on the (a) pressure and (b) temperature profiles along the nozzle axis. Numerical error bars result from an UQ analysis performed in test conditions identified as run 1-1 in Tab. 2.1

error bars. To this purpose, SU2 is coupled with the non-intrusive library *RobUQ* from INRIA (Institut national de recherche en informatique et en automatique). *RobUQ* includes state-of-the-art methods for robust Uncertainty Quantification, see Congedo *et al.* (2012). In the present analysis, only the uncertainties on P^t and T^t are propagated in the CFD simulation, since, according to Cinnella *et al.* (2010), uncertainties on the thermodynamic model can be neglected with respect to other sources of uncertainty. The assumption of a Gaussian distribution for measurement uncertainties results from the calibration process of pressure transducers and thermocouples. In order to propagate the measurement uncertainties associated to P^t and T^t readings, the single deterministic computation run for the nominal values of the boundary conditions is replaced with a whole set of computations, each one of those being run for specific values of the uncertain conditions. Results from the UQ analysis on the numerical solution are reported in Fig. 2.17. Results refer to Navier-Stokes simulations, run using the SW model. In the pressure profile of Fig. 2.17a, a very good agreement with respect to experimental data is observed, which proves robust and predictive solution ($< 0.01\%$ deviation from the nominal trend). Temperature measurements along the nozzle axis are not available. However, Fig. 2.17b reveals that the deviation from the nominal temperature trend caused by the uncertainty on the inlet total temperature lies below 0.2%.

In order to highlight non-ideal compressible-fluid effects, it is interesting to compare the expansion process occurring at maximum Z^t with those at lower Z^t, up to the minimum value. For all the analyzed cases, the pressure ratio P/P^t along the expansion is higher than the ideal-gas one (at maximum Z^t) and increases with increasing departure from ideality, as Z^t decreases. Such trend is ascribed to non-ideal effects and has no relation with measuring accuracy. The described trend of measured pressure ratio shows a very good quantitative consistence with the results of a two-dimensional Euler simulations using the SW model. Experimental and numerical results are compared in figure 2.18. Uncertainty bars are also shown to indicate the accuracy of the measurements. The dependency of the flow field from the inlet conditions is found to be not negligible, for both cases of moderate and high deviation from the ideal-gas state.

For the two analyzed tests, the flow Mach number M in the diverging portion of the nozzle is directly measured along the nozzle centreline, as described in paragraph 2.1.2. Mach number measurements are available from schlieren images corresponding to the same Z^t selected for the

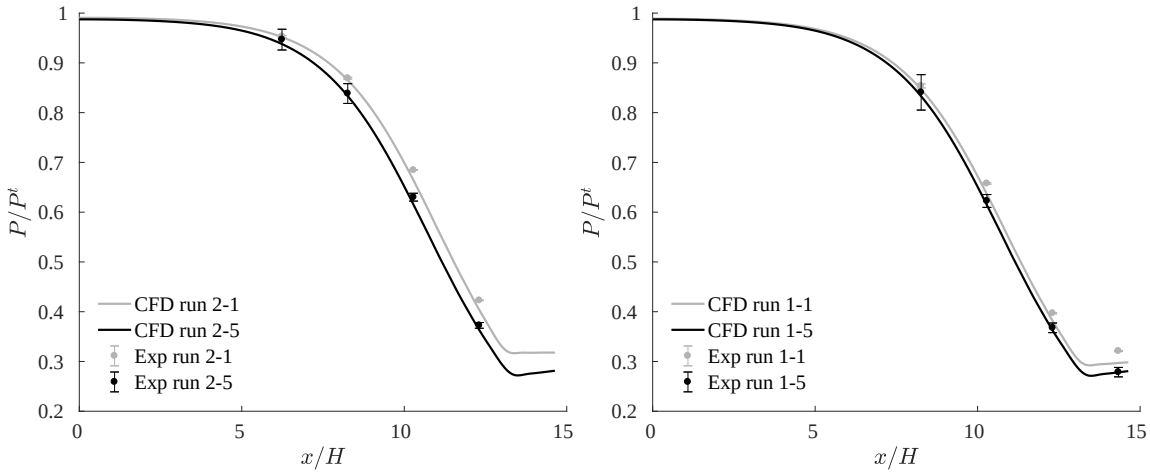

(a) (b)

Figure 2.18: Comparison between experimental and CFD values of P/P^t at the nozzle axis as a function of x/H. Test conditions are reported in Tab. 2.1 and 2.3

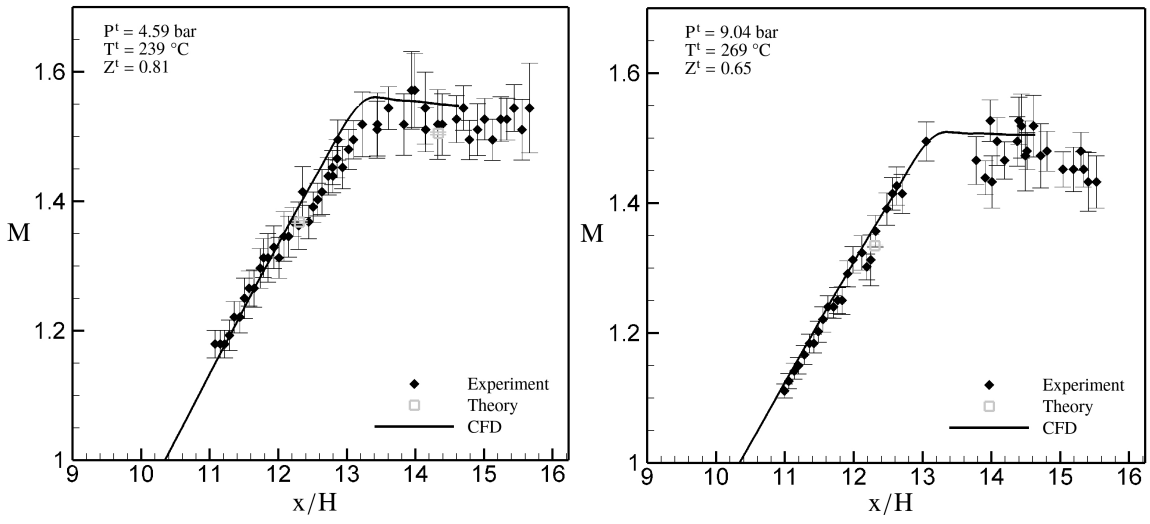

(a) (b)

Figure 2.19: Measured Mach number distribution in the diverging portion of the nozzle, along the nozzle centreline. Operating conditions at nozzle inlet are reported on the plot.

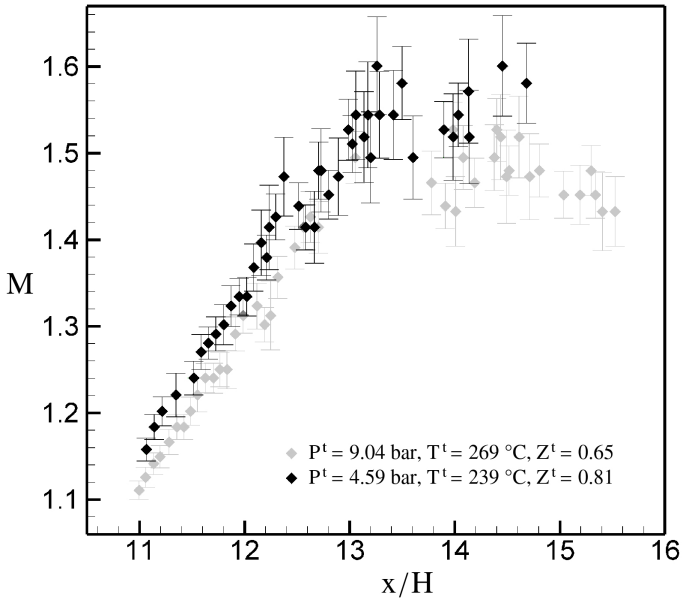

Figure 2.20: Comparison between measured Mach number distribution at the axis of the nozzle in the diverging portion for test conditions defined by P^t = 9.04 bar, T^t = 269 °C, Z^t = 0.65, and P^t = 4.59 bar, T^t = 239 °C, Z^t = 0.81

analysis of pressure ratios. In Fig. 2.19, the measured Mach number is compared to the Mach number profile obtained from a Navier-Stokes simulation and to the Mach number calculated by resorting to the isentropic hypothesis for nozzle expansion. Both CFD and theoretical results are obtained using the SW model. Results show a good agreement, thus confirming the accuracy of the thermodynamic model employed.

Figure 2.20 contains a comparison between the local Mach number measured at the nozzle axis for test conditions defined by P^t = 9.04 bar, T^t = 269 °C, Z^t = 0.65 and P^t = 4.59 bar, T^t = 239 °C, Z^t = 0.81. These values were chosen as the minimum and the maximum compressibility factors at which schlieren images quality is good enough to allow the detection of Mach lines. The comparison shows that as the non-ideal effects increase, the Mach value level decreases with respect to its perfect gas counterpart. Although a partial overlap of uncertainty bars is present, especially at the expansion end, where the exit conditions are reached, the trend is clearly visible, in particular, within the region of higher gradients, up to $M \approx 1.55$. This represents a further proof of the dependency of the nozzle flow-field on the stagnation conditions, for a given geometry and working fluid.

2.5 Conclusions

Results of an experimental campaign carried out to study the NICF flow of siloxane vapour MDM in a converging-diverging nozzle were presented. The nozzle was designed using the method of characteristics, complemented with state-of-the-art non-ideal EoS. Operation of the nozzle was verified by several tests performed in the nozzle test section of the Test Rig for Organic VApors (TROVA) and by numerical simulations using SU2. The flow-field in the nozzle was characterized by means of total temperature and pressure measurements in the wind-tunnel settling chamber, of static pressure measurements along the nozzle axis, and of schlieren visualizations, which provided a direct measurement of the Mach number at the nozzle centreline. Numerical simulations

using state-of-the-art thermodynamic models and theoretical predictions based on the isentropic hypothesis for nozzle expansions agree well with experimental data. For the NICFD numerical solver SU2, an Uncertainty Quantification analysis proved the accuracy and robustness of the numerical predictions. The nozzle flow is proven to be non-ideal, since the inlet thermodynamic conditions are seen to significantly affect both the pressure ratio and the Mach number distribution along the nozzle axis, contrarily to the well-known behavior of perfect gases. Hence, the design and analysis of aerodynamic devices operating with molecularly complex vapours should account for non-ideal effects, especially if the devices operate in thermodynamic conditions featuring non-ideal flow behaviour.

3 *Influence of a recessed step at the throat section of supersonic nozzles*

In the expansion of a fluid through a converging-diverging duct, the viscous boundary layer displaces the so-called inviscid core from the duct walls by its thickness or mass defect, thus modifying the area and pressure distributions through the duct and the position and shape of the sonic line, with respect to the inviscid-flow design. The maximum massflow discharged by the duct, which is proportional to the throat area, is slightly reduced due to the contraction of the minimum-area passage. In this respect, a significative influence on the massflow is due to the shape of the nozzle. Moreover, operating conditions (e.g. the reservoir or discharge pressure) are subject to small variations over time, which in turn cause boundary layer unsteadiness. Boundary layer unsteadiness can possibly be controlled by the introduction of a geometry singularity such as a sharp corner or a recessed step, which triggers separation of the boundary layer at the singularity location.

In the present chapter, the supersonic expansion of dilute dry air and siloxane vapour MDM in two planar converging-diverging nozzles is examined. For both nozzles, adapted flow conditions are considered. Separation of the boundary layer at the nozzle throat is imposed by the introduction of a small recessed step at the minimum-area section. Both nozzles are tested in the TROVA supersonic wind-tunnel and simulated numerically with SU2. Pressure measurements along the nozzle axis, schlieren visualizations and numerical simulations are performed to investigate the influence of the recessed step at the throat on the supersonic flow-field. In the experiments, the height of the recessed step is 0.1 *mm for both nozzles, and the nozzle height at the throat is* 10 *mm for the air nozzle and* 16.8 *mm for the MDM nozzle. For the air nozzle, numerical simulations examine also* 0.05 *mm and* 0.2 *mm step heights. A perturbation wave pattern originates from the step, which results in a perturbation of the measured pressure profile close to the throat section. In the diverging portion, sufficiently far from the throat section, the pressure profile of the recessed-step nozzle matches the one of the clean configuration.*

The present chapter is structured as follows. The flow in the nozzle operating with air is analyzed first. In paragraph 3.1, the operation of the nozzle in adapted flow conditions is examined and results for the clean and recessed step configuration are compared. A closer investigation to the flow pattern originating at the step edge is presented in paragraph 3.1.1. In paragraph 3.1.2, the effect of the step height is examined. Results for supersonic expansions in a recessed-step nozzle in the non-ideal compressible-fluid regime are presented in paragraph 3.2. Paragraph 3.3 provides concluding remarks.

Part of the contents of this chapter appear in:

Cozzi, F., Spinelli, A., Carmine, M., Cheli, R., Zocca, M. & Guardone, A. 2015 Evidence of complex flow structures in a converging-diverging nozzle caused by a recessed step at the nozzle throat. In 45th AIAA Fluid Dynamics Conference

Zocca, M., Spinelli, A., Cozzi, F. & Guardone, A. Influence of a recessed step at the throat section of a supersonic nozzle. Approved for publication in The Aeronautical Journal (2018)

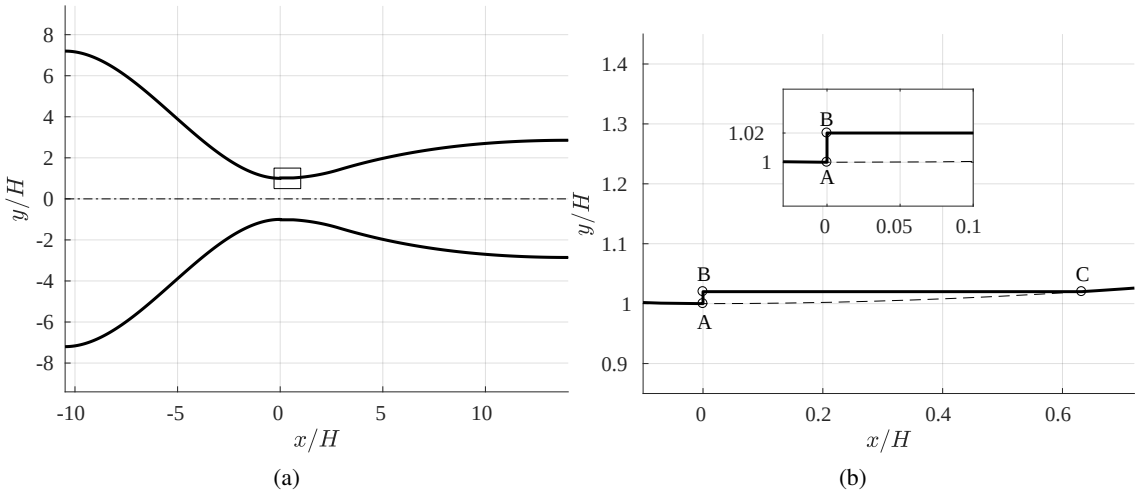

Figure 3.1: Non-dimensional geometry of the converging-diverging nozzle operating with air. (a) Complete geometry. (b) Detail view of the throat section and of the recessed step

3.1 Ideal-gas adapted nozzle flows for the clean and recessed-step configurations

In the present paragraph, expansions of dilute dry air in a supersonic nozzle featuring a recessed step at the throat section are considered, and the effects of the recessed step on the nozzle flow in adapted conditions are examined. The analysis is based on experiments carried out in the TROVA wind tunnel and on numerical simulations performed with SU2. Both the experimental test-rig and the numerical tool are described extensively in chapter 2.

Two different nozzle geometries are considered, one with the recessed step and one with a smooth profile at the throat (clean configuration). The non-dimensional geometry of the converging-diverging nozzle is shown in Fig. 3.1a. The normalization parameter is the throat half-height H. The nozzle is designed to operate with dilute dry air. In adapted conditions, the reservoir to ambient pressure ratio $\beta = P^t/P_a$ is 20 and the exhaust design Mach number is 2.59. The Reynolds number computed using the throat half-height H as the reference length and sonic flow conditions is $\mathrm{Re} = 3.73 \times 10^5$. The diverging portion of the nozzle is designed by applying the method described in paragraph 2.3, while the profile of the converging portion is defined by a 3$^{\mathrm{rd}}$ order polynomial curve. At the throat section, the profiles of the converging and diverging portions match with horizontal tangent. The throat half-height is 5 mm and the nozzle is 18.7 mm wide, which results in a throat area of 187 mm^2. The inlet to throat area ratio or, equivalently, the contraction ratio of the converging portion is 7.2, while the exit to throat area ratio is 2.86. The axial location of the geometrical throat is coincident with the third pressure tap along the nozzle axis and the exhaust section is located past the seventh pressure tap (cf. Fig. 2.8). The overall nozzle length is 122.6 mm and the ratio of the length of the diverging portion to that of the converging one is 1.34.

The geometry with the recessed step at the throat is obtained by machining the top and bottom contoured profiles as shown in the detail view of Fig. 3.1b. The height of the recessed step at the geometrical throat is $h = 0.1$ mm, which corresponds to 2% of the throat half-height.

In all experiments reported in the present paragraph, the fluid is air and the pressure in the high pressure vessel is 12 bar. The flow is throttled through a control valve to reach a total pressure of 4 bar in the settling chamber. The fluid exiting from the nozzle is discharged into the low pressure vessel, where the pressure at the beginning of the test is about 0.1 bar. The downstream reservoir fills during the experiment, hence the pressure downstream of the nozzle increases gradually

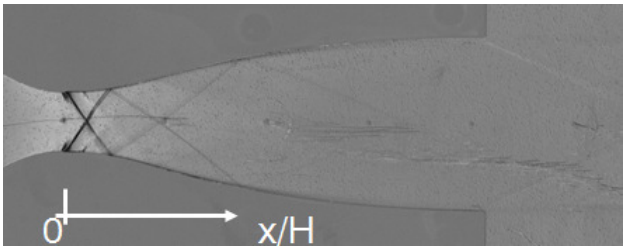

(a)

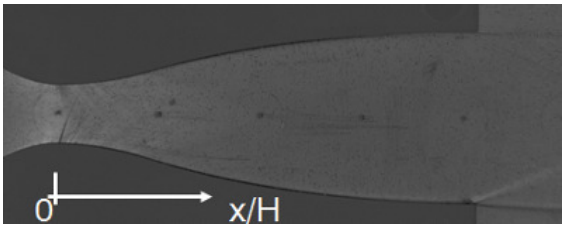

(b)

Figure 3.2: Schlieren visualization of the adapted nozzle flow, $\beta = 20$. (a) Recessed-step configuration. (b) Clean configuration

until equilibrium is reached. The nozzle flow regimes change accordingly from under-expanded conditions to an un-chocked, fully subsonic flow.

Figure 3.2 reports the schlieren visualizations of the flow field in adapted conditions for both the recessed-step and the clean configurations. Images include about 10 mm of the converging portion, the divergent and 31.6 mm of the downstream ambient. Density gradients parallel to the nozzle axis are visualized. Darker gray levels are associated to positive density gradients (compressions) and lighter gray levels to negative ones (expansions).

For the recessed-step geometry, the schlieren visualization reported in Fig. 3.2a reveals the occurrence of a complex flow pattern in the throat region of the nozzle. It is a perturbation wave system originating at the step edge (point A in figure 3.1b) and propagating towards the exit section of the nozzle with multiple reflections at the nozzle walls and mutual interactions at the nozzle axis. For comparison, the same adapted flow conditions of Fig. 3.2a are replicated in Fig. 3.2b for the clean configuration. As expected, the flow in the diverging portion is free of shocks and no perturbation waves originate in the throat region of the nozzle. Indeed, the schlieren image of the clean configuration distinctly shows the Mach lines in the supersonic portion of the nozzle, especially in the throat region, where the strongest density gradients are attained. In both Fig. 3.2a and Fig. 3.2b, the equally spaced dark spots along the nozzle axis mark the location of the static pressure taps.

According to schlieren visualizations, the clean and recessed-step nozzles exhibit markedly different flow arrangements even in adapted flow conditions. However, schlieren visualizations cannot be used to determine the relative intensity of these flow features. To this purpose, static pressure measurements along the nozzle axis and numerical simulations of the overall nozzle flow are now used to quantify the influence of the recessed step on the static pressure field.

Nozzle flow simulations are performed using SU2 on both the clean and recessed-step configurations. The computational domain reproduces the test section of the TROVA. For the planar nozzle geometry of interest here, two-dimensional simulations are considered to be sufficient to capture the flow behavior at the middle section of the wind tunnel, where the interaction with the sidewall boundary layer is expected to be negligible. Therefore, two-dimensional simulations are performed in the domain defined by the converging-diverging profile reported in Fig. 3.1, with and

Table 3.1: Computational grids for the simulation of the clean and recessed-step configurations

Designation	Geometry	Type	N_{nodes}	N_{elements}
C1	Clean	Quadrilateral	28 272	27 911
C2	Clean	Quadrilateral	81 792	81 196
C3	Clean	Quadrilateral	105 435	104 728
C4	Clean	Quadrilateral	304 545	303 380
S1	Step	Hybrid	162 009	280 721
S2	Step	Hybrid	392 433	550 796

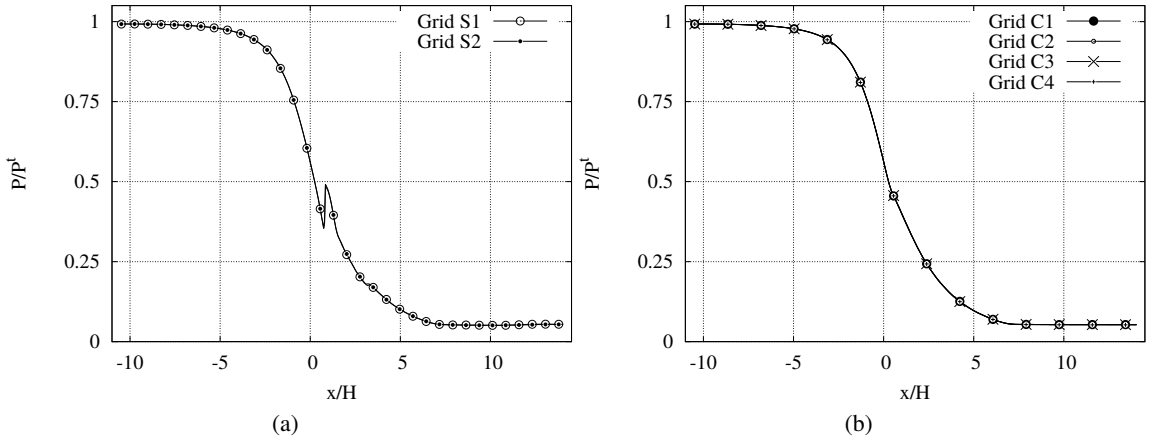

Figure 3.3: Grid convergence evaluated on the pressure profile along the nozzle axis. (a) Recessed-step configuration. (b) Clean configuration

without the recessed step at the throat. Stagnation pressure and temperature are assigned at the nozzle inlet section. They are 4 bar and 288 K, respectively. At the nozzle exhaust section, static pressure is imposed, which in adapted conditions is 0.2 bar ($\beta = 20$). Turbulence is modeled using the k-ω SST turbulence model.

A grid dependence study on the pressure along the nozzle axis in adapted conditions is shown in Fig. 3.3. The pressure is computed in both the clean and the recessed-step configuration using the computational grids listed in Table 3.1. For the clean configuration, four quadrilateral grids are used. The recessed-step geometry is simulated instead on two different hybrid quadrilateral-triangular grids. For both geometries, the first grid point is placed in the viscous sublayer, so that no wall functions are used. From Fig. 3.3a and Fig. 3.3b, the independence of the calculated pressure profile on the computational grid is apparent. In the following, the C2 grid (made of 81 792 nodes and 81 196 elements) is adopted for all the simulations of the clean configuration.

In addition to an accurate representation of the overall nozzle flow, the simulation of the recessed-step nozzle also requires to correctly reproduce the flow past the geometry singularity at the throat. While the overall nozzle flow has a characteristic length of $\mathcal{O}(10$ mm) (i.e. the height of the throat section), the flow past the recessed step has a much smaller characteristic length of $\mathcal{O}(0.1$ mm) (i.e. the step height). At the recessed-step location, the incoming boundary layer separates and forms a recirculation region, which ends at the reattachment point on the bottom wall downstream of the obstacle, as observed e.g. by Hama (1966) and Wu *et al.* (1971). For the recessed-step nozzle, the dependence of the solution within the recirculation region on

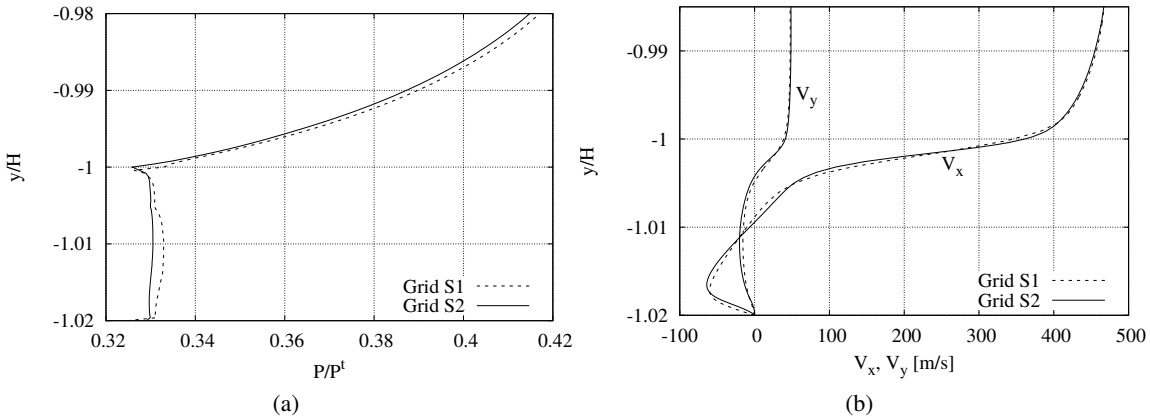

Figure 3.4: Grid convergence results for the recessed-step configuration. (a) Pressure profile along the step vertical wall ($x/H = 0, -1.02 < y/H < -0.98$). (b) Velocity profiles along y/H and at one step height downstream of the throat. ($x/H = h, -1.02 < y/H < -0.98$)

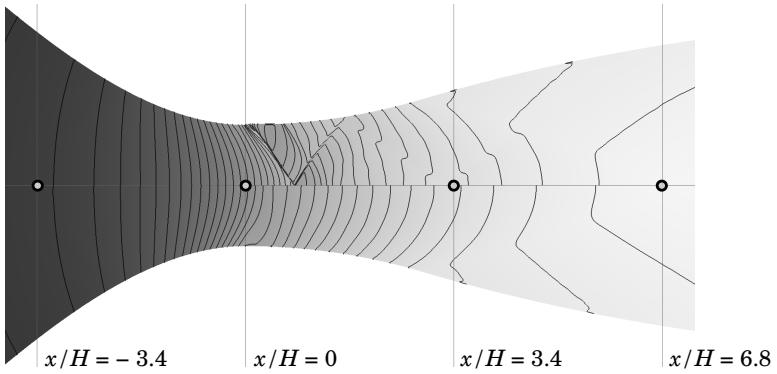

Figure 3.5: Static to total pressure ratio in adapted conditions for the recessed-step (upper portion) and the clean (lower portion) configuration

the grid resolution is also checked as follows. Figure 3.4a reports the pressure profile along the vertical wall of the step on the lower nozzle wall, from the step base ($y/H = -1.02$) to a point located at a distance of one step height from the minimum-area section ($y/H = -0.98$). The numerical profiles of the two velocity components along y/H and at one step height downstream of the throat ($x/H = h$) are also shown in Fig. 3.4b. The pressure in the recirculation region past the recessed-step is expected to keep a constant value, except in the close proximity of the bottom wall and of the step edge. Such behaviour appears to be better captured by the pressure profile computed on the finest (S2) grid (Fig. 3.4a). From Fig. 3.4b, grid independence of the velocity profiles at $y/H > -1$ is apparent. More prominent differences are observed in the velocities calculated within the recirculation region ($y/H < -1$). In the following, the S2 grid (made of 392 433 nodes and 550 796 elements) is adopted for all the simulations of the recessed-step configuration.

Numerical results for the static to total pressure ratios P/P^t for the adapted flow regime are

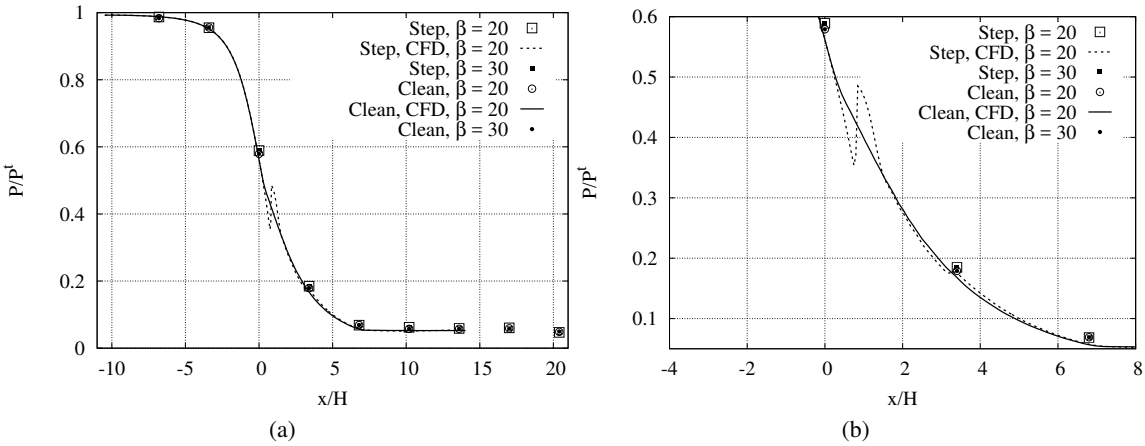

Figure 3.6: (a), (b) P/P^t along the nozzle axis in adapted and underexpanded conditions for the clean and the recessed-step configurations. (b) Detail view of the throat region

showin in Fig. 3.5. In the top portion of the plot, numerical results for the recessed-step configuration are reported. The complex wave structure observed in the experiments (cf. Fig. 3.2a) is clearly visible. For the clean configuration, numerical results confirm a smooth subsonic-to-supersonic transition in the throat region. For consistency, pressure isolines refer to the same pressure levels for both the clean and the recessed-step configuration.

In Fig. 3.6a, the static pressure measured along the nozzle axis in adapted and under-expanded conditions is compared to numerical simulations for the clean and recessed-step configuration. Since the simulations concern the flow inside the nozzle, under-expanded and adapted conditions are the same, difference being expected past the nozzle exit section. Experimental results are reported over 9 different pressure taps. Fig. 3.6b provides a detail view of the pressure profile in the throat region and in a portion of the divergent. Both charts clearly show that, in the diverging portion and sufficiently far from the throat section, the recessed-step nozzle attains the same pressure level of its smooth counterpart. This result suggests that the perturbation introduced by the recessed step acts only locally and does not alter significantly the flow in the diverging portion. In other terms, the perturbation introduced by the recessed step, which is very evident in the qualitative schlieren images, is in fact small if compared to the main expansion process.

3.1.1 Flow features in the throat region

A closer investigation including both schlieren visualizations and numerical simulations is now performed to unveil the nature of the perturbation wave system observed in the previous section. A Schlieren visualization of the throat region in adapted conditions is shown in figure 3.7a. This enlarged schlieren image is recorded by replacing the lens designated as Lens 2 in Fig. 2.3 (150 mm focal length) with a lens of 1000 mm focal length and by adjusting the camera position accordingly. Contrary to the schlieren images reported in the previous paragraph, the knife position is adjusted in such a way that light rays deflected by positive density gradients are left unblocked. Hence, expansions appear as darker regions, compressions as lighter ones. In figure 3.7b, the computed isolines of the density gradient in the streamwise direction are superimposed to the schlieren image, showing indeed a fine agreement.

With reference to Fig. 3.7a and 3.7b, and to the qualitative representation of the flow configuration reported in Fig. 3.8, the flow pattern in the throat region can be understood. The boundary layer separating at the step edge (point A in in Fig. 3.8) reattaches on the downstream bottom wall

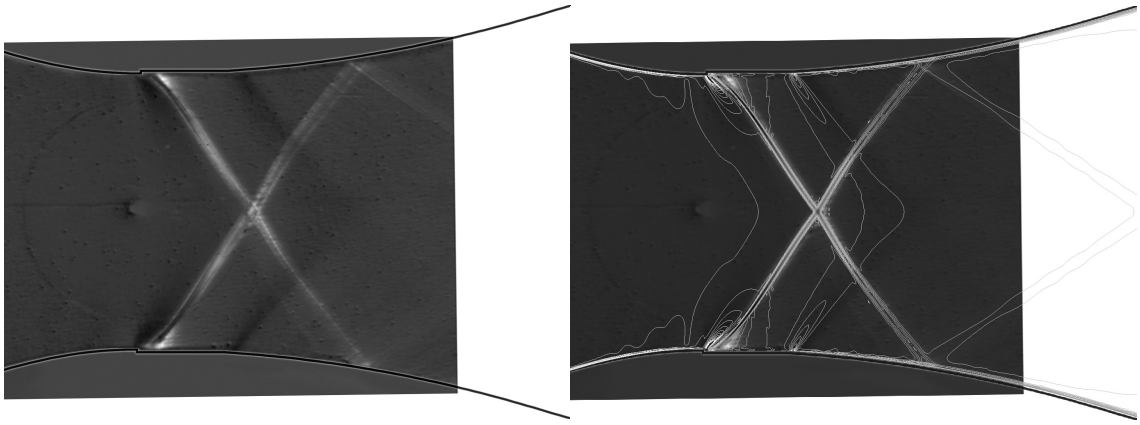

(a) (b)

Figure 3.7: (a) Schlieren visualization of the throat region. (b) Isolines of the density gradient in streamwise direction (from CFD simulation) superimposed to the Schlieren visualization

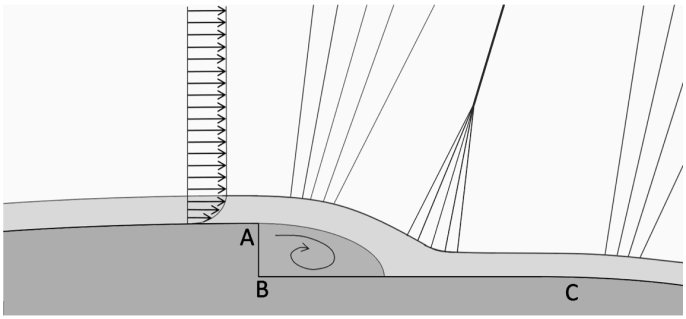

Figure 3.8: Qualitative representation of the supersonic flow at the recessed step location, according to Stanewsky (1973)

and encloses a separation bubble past the vertical wall of the step. A Prandtl-Meyer expansion fan is centered at the step corner. The fluid then expands over the separated region and it recompresses again near the reattachment point through a series of weak compression waves. The compression waves eventually coalesce into an oblique shock, which is clearly observed in the schlieren visualization of Fig. 3.7a (white curve originating at the recessed step location). Away from the step, the oblique shock is curved and bent upstream due to the interaction with the expansion fan emanating from the step edge (point A in Fig. 3.8). This interaction is clearly visible from both Fig. 3.7a and 3.7b. At the location identified as point C in Fig. 3.8, the recessed step ends and a second expansion fan is formed.

In addition to the flow features outlined previously, the presence of a so-called lip-shock at the onset of boundary layer separation past backward-facing obstacles is documented in the experimental and numerical studies by Hama (1966) and Halupovich *et al.* (1999). Across the lip shock, the pressure of the expanded flow past the step corner increases to reach its so-called base value at the bottom of the step. At the reattachment point, the fluid is further compressed by the compression wave-oblique shock system described previously, often referred in literature as wake shock (see e.g. Hama (1966)).

As a further assessment of the capabilities of the adopted numerical method to capture nozzle flows in the recessed-step configuration, supersonic channel flows experiencing an expansion past a backward-facing step are simulated with SU2. Results are validated by comparison between

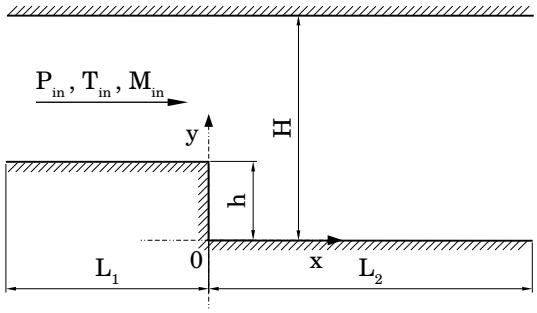

Figure 3.9: Computational domain for the simulation of uniform supersonic flows past recessed-step obstacles. The geometry of the domain is taken from Halupovich *et al.* (1999)

Table 3.2: Simulation data for supersonic channel flow test cases. Test case 1 and Test case 2 reproduce test case 22 and 5 reported by Halupovich *et al.* (1999), respectively

	Test case 1	Test case 2
P_{in} [Pa]	101 325	34 800
T_{in} [K]	250	167
M_{in}	3	2
h [mm]	10	3.18
L_1	$25.3h$	$4.6h$
L_2	$9.05h$	$9.05h$
H	$9.08h$	$6.6h$
Re_h	600 000	103 300

experimental results of planar laser-induced iodine fluorescence (PLIIF) measurements of Hartfield *et al.* (1993) and CFD simulations of Halupovich *et al.* (1999). The computational domain is shown in Fig. 3.9 and simulation parameters are given in Table 3.2. Numerical results of test case 1 are reported in Fig. 3.10. The normalized pressure profile along the bottom wall behind the step is given in Fig. 3.10a versus the non-dimensional abscissa. The origin is set at the step base and the normalization parameter for unit length is the step height. In the base region immediately downstream of the step, the pressure is significantly lower than free-stream. The flow pressure attains its free-stream value close to the reattachment point. Fig. 3.10b reports the normalized pressure profile along the vertical wall of the step. The flow experiences a pressure drop near the step edge, down to a value that is lower than the base pressure. The base pressure value is then restored by the lip shock and remains constant along the vertical wall.

SU2 calculations are reported over two different hybrid quadrilateral-triangular grids and compared to the CFD results documented by Halupovich *et al.* (1999). The coarse grid is made of 120 974 nodes and 173 138 elements and the fine one of 588 893 nodes and 864 094 elements. In both SU2 grids, the first grid point is placed in the viscous sublayer. The reference CFD results of Halupovich *et al.* (1999) are obtained using the PHOENICS CFD code, which instead implements a k-ε turbulence model with a wall treatment based on the wall-function approach. The computational grid of the reference simulation is a quadrilateral grid of $\mathcal{O}(10^4)$ nodes and elements. In the separated flow region, where the k-ε model coupled with a wall-function approach is expected to give less accurate results than the k-ω SST turbulence model, there is poor agreement between the

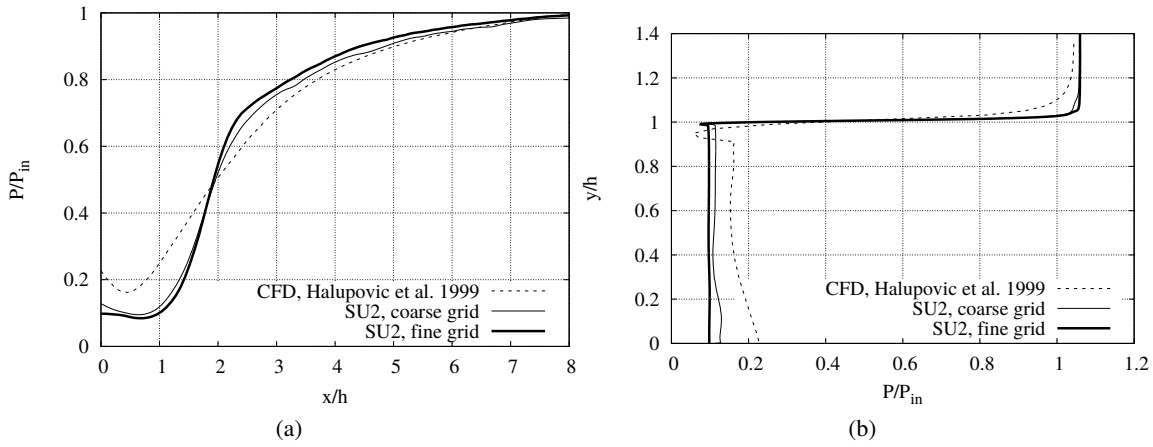

Figure 3.10: SU2 results for Test case 1 compared to CFD results reported by Halupovich *et al.* (1999). (a) Normalized pressure profile along the bottom wall behind the step. (b) Normalized pressure profile along the vertical wall of the step

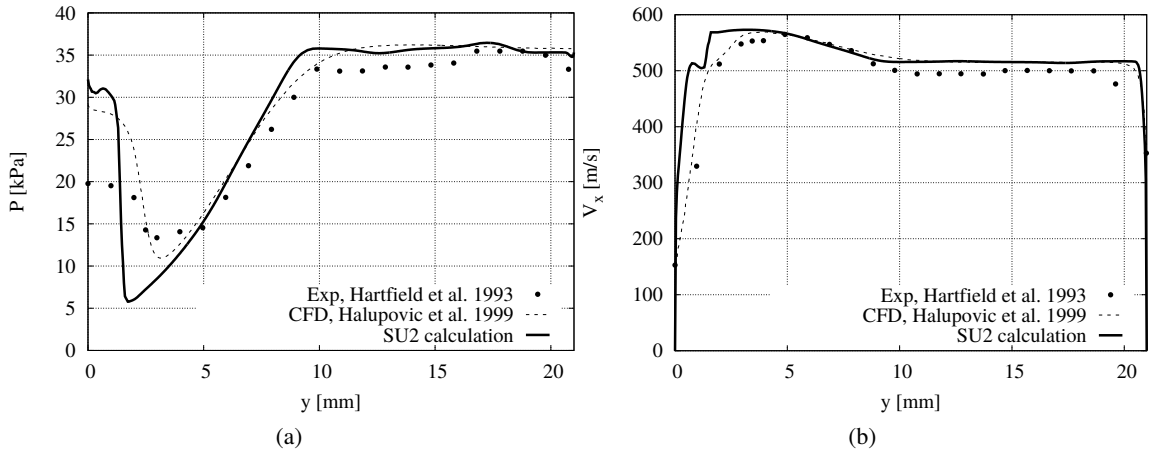

Figure 3.11: SU2 results for Test case 2 compared to the CFD results reported by Halupovich *et al.* (1999) and the PLIIF measurements of Hartfield *et al.* (1993). (a) Pressure and (b) streamwise velocity profiles in a direction parallel to the vertical wall of the step and 10 mm downstream of the step base

SU2 and the reference calculations. Outside of the separated flow region, the agreement between the pressures predicted by the two codes is better. Among the SU2 results, a grid dependence of the pressure levels achieved in the recirculation region is observed. As expected, the fine grid better captures the typical pressure distribution attained in recirculation regions.

Results of test case 2 (see Table 3.2) are presented here to assess the SU2 calculations against the experimental data of Hartfield *et al.* (1993) and the CFD results of Halupovich *et al.* (1999). The pressure and streamwise velocity profiles in a direction parallel to the vertical wall of the step and 10 mm downstream of the step base are reported in Fig. 3.11. The grid spacing adopted in the SU2 simulation (418 465 nodes and 674 722 elements) is the same as that of the fine grid of test case 1. The vertical line along which the pressure and velocity profiles of Fig. 3.11 are extracted crosses the wake shock and is located downstream of the reattachment point. The presence of the wake shock is detected by both PHOENICS and SU2, though the two solvers

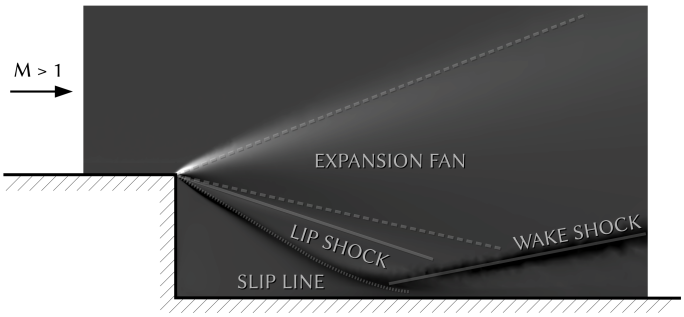

Figure 3.12: Qualitative representation of the supersonic flow at the recessed step location according to the schematization proposed by Hama (1966)

predict a significantly higher pressure drop than the measured one.

The results obtained from the two channel flow test cases provide valuable insights into the qualitative description of the flow around the step corner in the case of the recessed-step nozzle. Similarly to the pressure profile reported in Fig. 3.10b, the pressure profile of Fig. 3.4a shows a dent close to the step edge, i.e. an overexpansion followed by a recompression which can be possibly associated to the presence of the lip shock. The orientation of the lip-shock is strongly dependent on the Mach and Reynolds number of the flow past the step. As documented by Hama (1966) and Wu *et al.* (1971) about uniform supersonic flows around backard-facing obstacles, for a given free stream Mach number, the lip shock is directed downward at the high Reynolds number but turns upward and decreases in strength as the Reynolds number decreases. The flow configuration resulting from test case 1 (Fig. 3.12) closely follows the scheme proposed by Hama (1966), with the lip shock located between the expansion fan and the shear layer dividing the recirculation region and the outer part of the boundary layer. In the case of the recessed-step nozzle of interest here, the relatively low Mach number (~ 1.04) at the step location, combined with the small size (0.1 mm) of the obstacle (the Reynolds number based on the step height is ~ 3500) result in flow features of lower intensity. Thus, the schlieren visualization and the computed flowfield do not clearly display the orientation and shape of the lip shock and the observed flow pattern is the one sketched in Fig. 3.8.

3.1.2 Assessment of the influence of the step height

In all experiments, the height of the recessed step at the nozzle throat is $h = 0.1$ mm (2.0% of the throat half-height). Numerical simulations are used here to examine two recessed-step configurations at varying height of the step, 0.2 mm ($2h$ configuration) and 0.05 mm ($h/2$ configuration). Similarly to the previous paragraphs, the analysis is restricted to adapted flow conditions.

In Fig. 3.13, a detail view of the calculated pressure fields (static to total pressure ratio) in the throat region close to the recessed-step location is reported. Results obtained for the $2h$ and $h/2$ configurations are compared to the reference (h) configuration. Inspection of the calculated flowfield reveals that, as expected, the length of the recirculation region past the step edge decreases at decreasing height of the recessed step. In equivalent terms, the axial position of the reattachment point moves upstream at decreasing height of the obstacle. As a result, the interaction between the wake shock, which originates at reattachment, and the expansion fan emanating from the step corner yields different orientations of the coalesced oblique shocks. Namely, if the reattachment point moves downstream, then the interaction between the expansion fan and the wake shock is more significant and therefore the coalesced shock is deflected farther downstream.

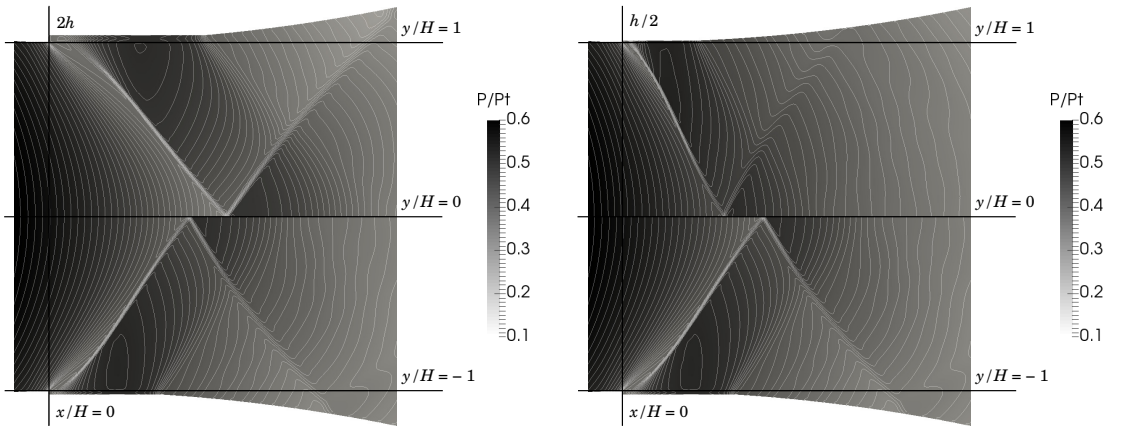

(a) (b)

Figure 3.13: P/P^t in adapted conditions in the throat region, close to the recessed step location. (a) $2h$ (top) and h (bottom) configurations. (b) $h/2$ (top) and h (bottom) configurations

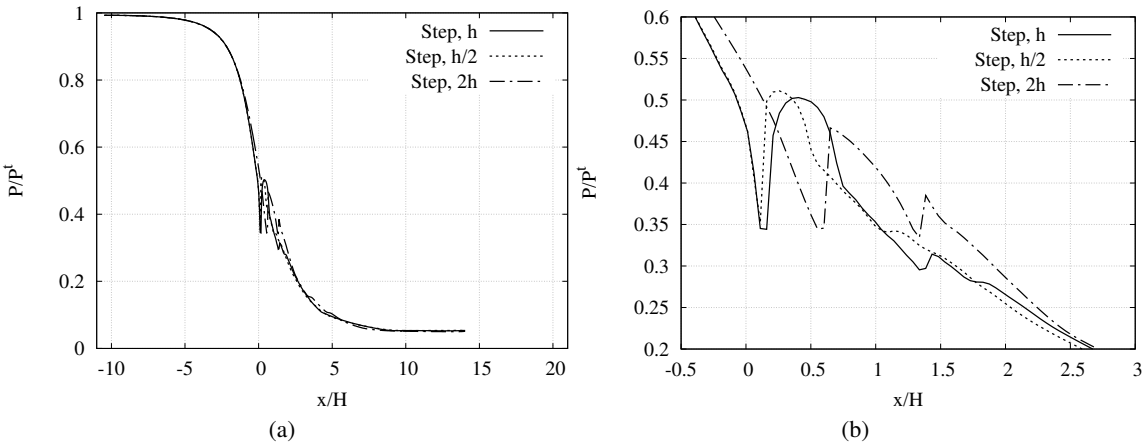

(a) (b)

Figure 3.14: (a), (b) P/P_{T} along an horizontal axis placed at 95% of the throat half-height ($y/H = 0.95$, i. e. 0.025 mm distance from the step corner) in adapted conditions for three recessed-step configurations: $h/2$, h, and $2h$. (b) Detail view of the throat region

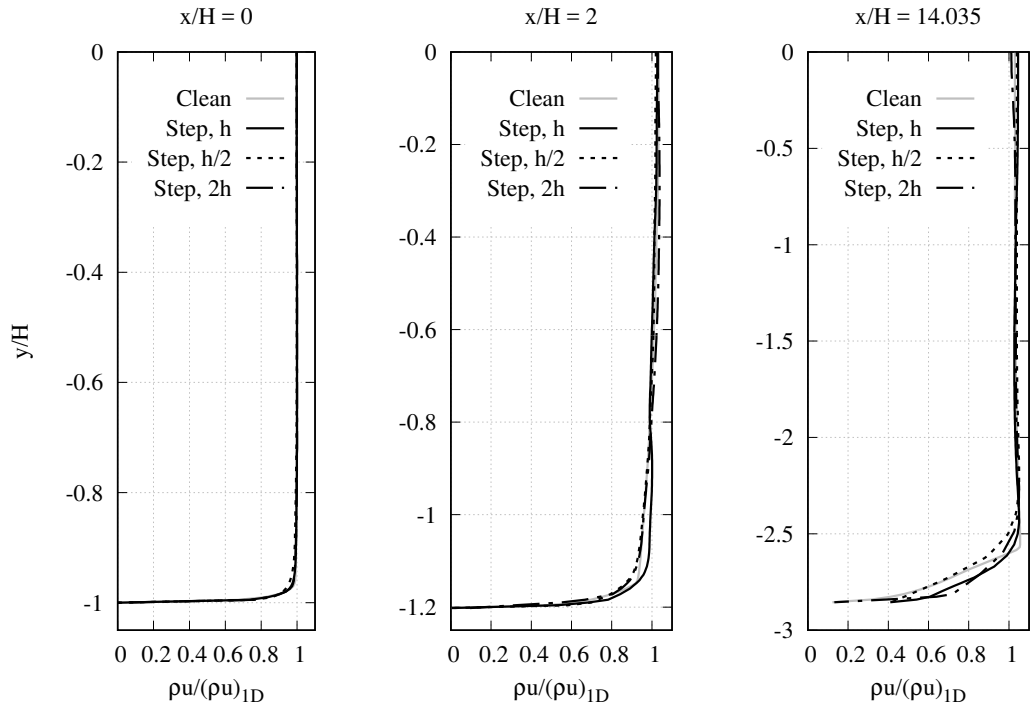

Figure 3.15: Momentum density in streamwise direction at three different stations: $x/H = 0$ (throat), $x/H = 2$ (10 mm downstream of the throat), $x/H = 14.035$ (exhaust)

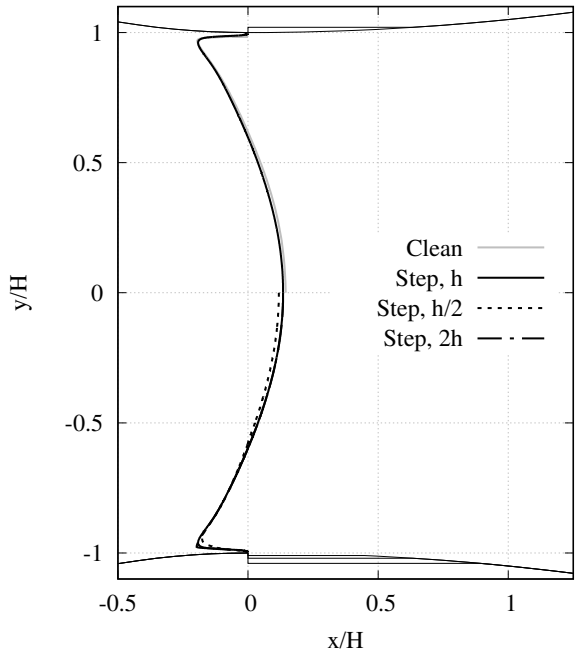

Figure 3.16: Sonic lines for four configurations: clean configuration and h, $h/2$, and $2h$ recessed-step configurations

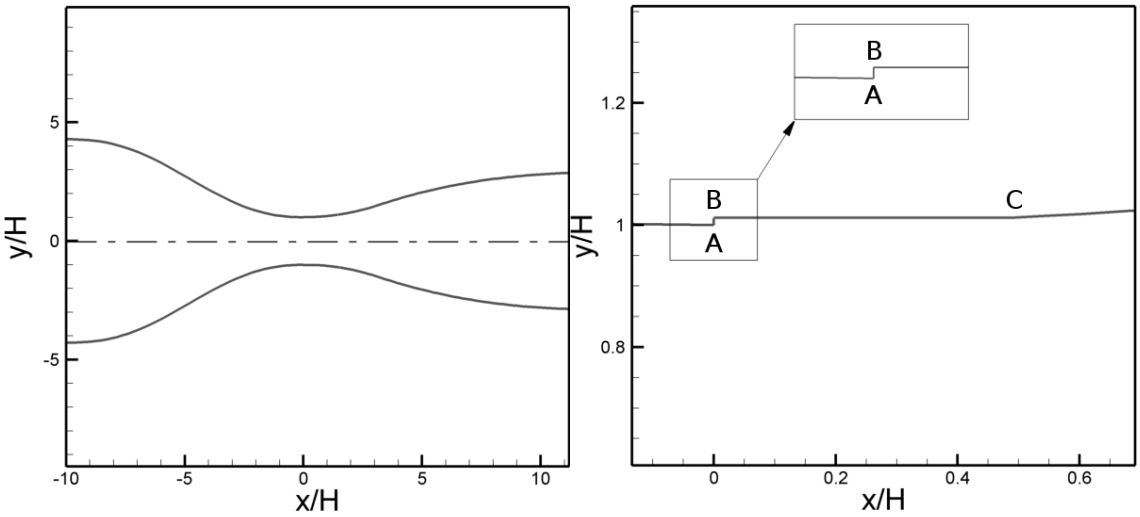

Figure 3.17: Non-dimensional geometry of the converging-diverging nozzle operating with MDM. (a) Complete geometry. (b) Detail view of the throat section and of the recessed step

The influence of the recessed step height on the adapted nozzle flow is evaluated by comparing a set of flow variables calculated in the $2h$, h and $h/2$ configurations.

The pressure along an horizontal axis placed at 95% of the throat half-height ($y/H = 0.95$, i.e. 0.025 mm distance from the step corner) is given in Fig. 3.14a and a detail view of the throat region is provided in Fig. 3.14b. The height of the recessed step influences the position and the intensity of the wake shock (see Fig. 3.14b), namely the wake shock occurs farther downstream and with a lower intensity at increasing height of the step. The perturbation waves originating at the throat exhibit a different reflection pattern at varying height of the step. Though, the pressure profiles of Fig. 3.14a clearly show that, sufficiently far from the throat region, the effect of the perturbation introduced by the step is dissipated and the pressure profiles computed for the three recessed-step nozzles overlap.

In Fig. 3.15, the profile of the momentum density in streamwise direction at the geometrical throat ($x/H = 0$), in the divergent section at $x/H = 2$ and at the nozzle exhaust ($x/H = 14.035$) is reported, while in Fig. 3.16 the sonic lines obtained for the clean configuration and at varying height of the step (h, $h/2$, and $2h$) are compared. Results display no significant differences in the inviscid core. Though, the shape of the throat section is seen to influence the flow in the boundary layer region only, where the most relevant discrepancies between the calculated flow variables are observed.

3.2 Complex flow structures at the nozzle throat in the NICFD regime

In the present paragraph, adapted flows in a recessed-step nozzle operating with siloxane vapour MDM are investigated.

The non-dimensional geometry of the converging-diverging nozzle is shown in Fig. 3.17a. The nozzle is 180.4 mm long, with a width of 18.7 mm. The throat half-height H is 8.4 mm, which gives a throat area of 314 mm^2 (20 mm equivalent diameter). The height at the exit section is 48.1 mm, which results in a exit-to-throat area ratio of 2.869. The nozzle is designed to operate with MDM. In design conditions, it performs an expansion from total pressure $P^t = 4$ bar and

P^t	T^t	Z^t
4.58	247	0.82
4.04	249	0.85
3.39	250	0.88
1.79	232	0.93

Table 3.3: Operating conditions for reference experiments on the MDM recessed-step nozzle. Pressures are expressed in bar, temperatures in °C

temperatrue $T^t = 253.2$°C to an exit pressure of 0.4 bar ($\beta = 10$), which corresponds to an exhaust Mach number of 2.05. The supersonic portion of the nozzle is designed by applying the method described in paragraph 2.3, while the profile of the converging portion is a 5^{th} order polynomial curve, which matches the diverging portion of the nozzle with horizontal tangent and continuous curvature. The height of the recessed step at the geometrical throat is $h = 0.1$ mm, which corresponds to 1.2% of the throat half-height.

Results of wind-tunnel tests performed in the TROVA test rig are available for the recessed-step geometry. For the recessed-step geometry, the pressure profile along the nozzle axis and schlieren visualization of the whole flow-field are compared to numerical results from SU2. Numerical simulations are also run on the clean geometry and the resulting pressure profiles are compared to the ones obtained for the recessed-step nozzle.

Table 3.3 reports the reference test conditions for the present analysis. They result from a test performed at moderate non-ideal conditions, at varying total conditions in the settling chamber. In the following, test conditions are labelled according to the compressibility factor in the total thermodynamic state Z^t.

Schlieren visualizations corresponding to the test conditions of Tab. 3.3 are reported in Fig. 3.18. Visualizations reveal the occurrence of a perturbation wave pattern similar to the one observed in the nozzle operating with dilute dry air (cf. Fig. 3.2). Except for the frame corresponding to the most dilute condition (Fig. 3.18d), visualizations of the flow in the throat region are largely affected by the measuring range issues discussed in paragraph 2.4, which cause expansions to appear as dark regions on the image. From schlieren images, multiple shock reflections on the profiled walls are also clearly visible (at about $11.5 < x/H < 14.0$), as well as weak waves generated in the divergent portion by small perturbation of the flow due to profile wall roughness.

For all the test conditions reported in Tab. 3.3, two-dimensional Navier-Stokes simulations are run on the recessed-step configuration and Euler simulations are run on the clean nozzle. The hybrid quadrilateral-triangular grid used to simulate the recessed-step geometry is made of 536 439 elements and 336 071 nodes, while the triangular grid of the clean nozzle is made of 10 473 elements and 5 480 nodes. For test condition featuring $Z^t = 0.82$, numerical simulations are compared to experimental results. In Fig. 3.19a, density isolines obtained from the Navier-Stokes simulation are superimposed to the corresponding schlieren frame (top portion of the nozzle), showing a fine agreement. In Fig. 3.19b, the static to total pressure ratio P/P^t from experiments is compared to the CFD results for the clean and recessed-step geometry. Both the Navier-Stokes and the Euler simulation reported in Fig. 3.19 are run using the iPRSV EoS. Turbulence is modeled using the k-ω SST turbulence model. Note that no turbulence model is validated against non-ideal flows and a large uncertainty is expected in this respect. Similarly to what observed for the nozzle operating with air (cf. Fig. 3.6 and paragraph 3.1), the presence of the perturbation wave system influences the pressure profile only locally, and the pressure profile of the recessed-step nozzle superimposes to that of the clean one, sufficiently far from the throat section.

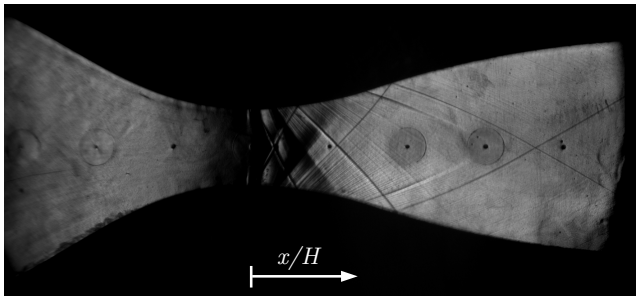

(a)

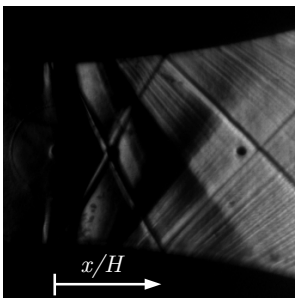

(b)

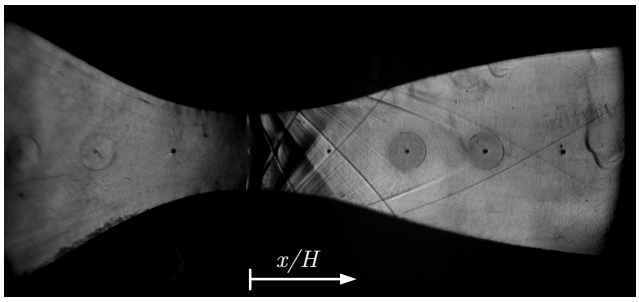

(c)

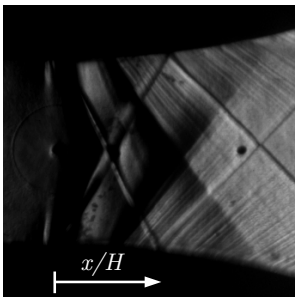

(d)

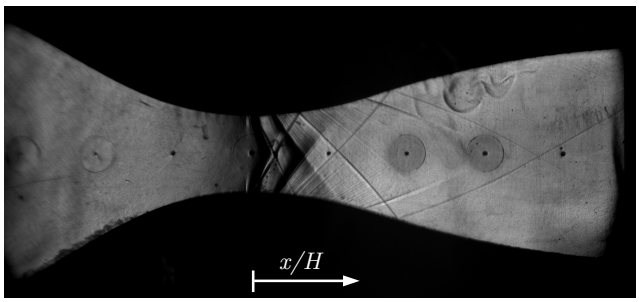

(e)

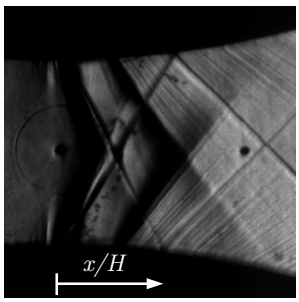

(f)

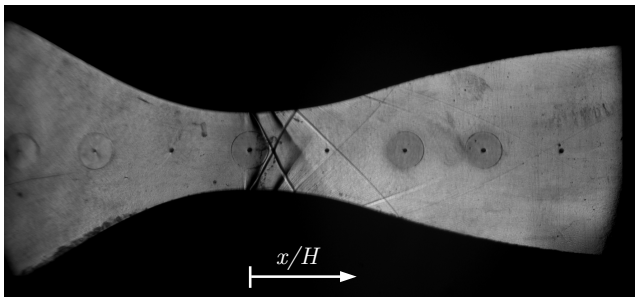

(g)

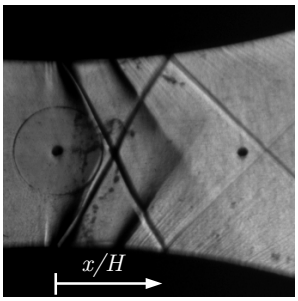

(h)

Figure 3.18: Schlieren visualizations of the flow field in test conditions reported in Tab. 3.3: (a), (b) $Z^t = 0.82$, (c), (d) $Z^t = 0.85$, (e), (f) $Z^t = 0.88$, (g), (h) $Z^t = 0.93$. (b), (d), (f), and (h) are detail views of the throat region

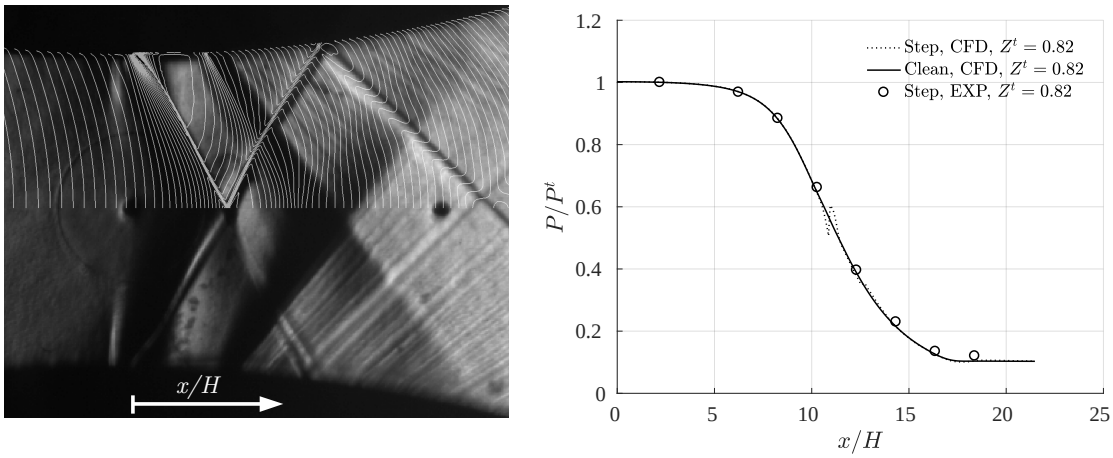

(a) (b)

Figure 3.19: (a) Density isolines from Navier-Stokes simulation superimposed to the schlieren image for $Z^t = 0.82$, (b) P/P^t along the nozzle axis from experiment and from simulations of the clean and recessed-step geometry

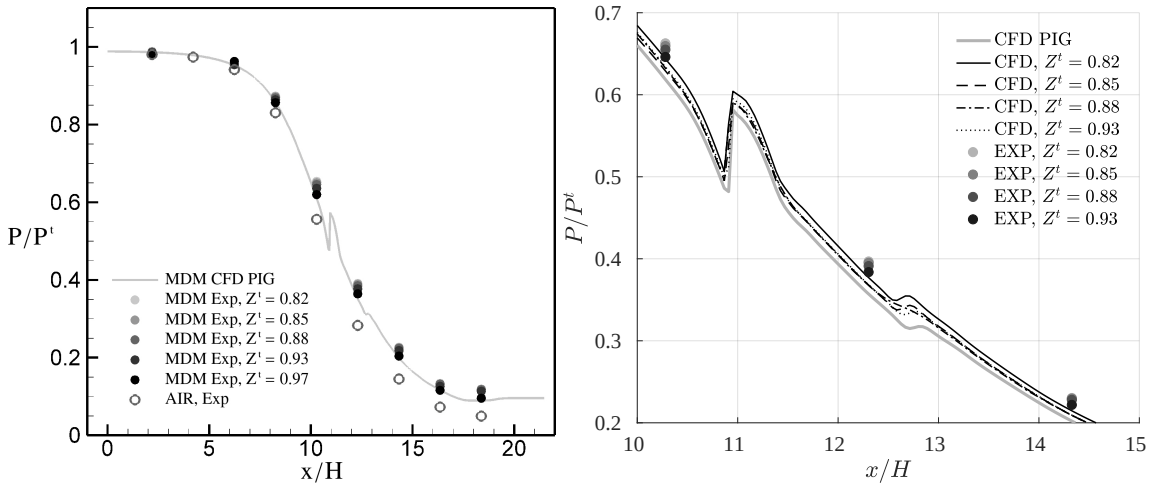

(a) (b)

Figure 3.20: P/P^t along the nozzle axis at varying Z^t from experiments and CFD. (a) Complete nozzle geometry (b) Detail view of the throat region

The expansion processes examined here occur in the non-ideal compressible-fluid regime. The pressure ratio P/P^t measured at the active taps is reported at varying Z^t on Fig. 3.20a. As a reference, the pressure ratio measured by operating the same nozzle with air and the continuous expansion profile from a Navier-Stokes simulation using the PIG EoS are reported. The constant specific heat ratio for MDM is $\gamma = 1.018$. As commented in the previous chapter (cf. paragraph 2.4), the pressure ratio P/P^t along the expansion is higher than the ideal-gas one and increases with increasing departure from ideality, i.e. as Z^t decreases. Consistently, CFD results are well overlapped to data measured at maximum Z^t. The detail view of Fig. 3.20b is now commented to evaluate the influence of flow non-ideality on the perturbation wave pattern at the throat. The plot reports the pressure profiles obtained from Navier-Stokes-iPRSV simulations in all test conditions of Tab. 3.3. The result from the Navier-Stokes-PIG simulation is reported for reference, together with experimental data at the throat pressure tap and at the two pressure taps downstream of the throat. Consistently with experimental data, the calculated pressure profiles corresponding to lower Z^t lie above the curves obtained at higher Z^t, and above the PIG curve. The upstream flow conditions influence the shock configuration at the step location, which in turn determine the configuration of shock reflections at the nozzle wall and their interaction at the symmetry axis. In Fig. 3.20b, this effect can be observed to a lesser extent from the numerical pressure profiles past the throat section, and to a greater extent at $x/H \approx 12.7$, where a small pressure bump due to the presence of two reflected shocks interacting at the nozzle axis is detected. The location of the shock interation point at the nozzle axis is seen to change at varying Z^t, namely it moves downstream as ideal-gas conditions are approached.

3.3 Conclusions

Experiments and numerical simulations were applied to the analysis of the flow in planar converging-diverging nozzles in the presence of a small recessed step at the throat section. The nozzles operated with dilute dry air and siloxane vapour MDM and the height of the recessed step was 0.1 mm for both nozzles, corresponding to 1% and 1.2% of the height of the throat section, respectively. Experimental investigations were carried out in the TROVA wind tunnel and included pressure measurements along the nozzle axis and schlieren visualizations. Adapted flow conditions for the recessed-step and the clean nozzles were simulated numerically with the open-source SU2 software and results compared to experimental data.

The nature of the complex perturbation wave system originating at the step location was investigated by means of schlieren visualizations and numerical simulations. The flow undergoes a supersonic expansion at the step corner. Past the step, the curvature of the separated region originates a system of compression waves, which finally coalesce into an oblique shock.

Pressure measurements along the nozzle axis and numerical results were used to quantify the influence of the presence of the recessed step on the pressure field in the diverging portion of the nozzle. The pressure profile along the axis exhibits a small dent in the close proximity of the throat section (axially located at the intersection of the oblique shocks emanating from the reattachment points), but it superimposes to that obtained in the clean configuration immediately downstream of the nozzle throat.

For the nozzle operating with air, numerical analysis of the nozzle flow in the presence of recessed steps of 0.05 mm and 0.2 mm (respectively half and twice the height of the reference one) pointed again at the local nature of the effects of the obstacle, though a significant variation in the layout of the perturbation wave pattern at varying step height is observed.

Finally, for the nozzle operating with MDM, non-ideal effects on the perturbation wave pattern were also pointed out, namely the dependence of its configuration on the upstream flow conditions.

4 Discharge coefficient for supersonic nozzle flows in the ideal and non-ideal compressible-fluid regimes

The discharged massflow rate is a key parameter for the design and performance analysis of supersonic nozzles. The massflow rate is often expressed as the ratio of the computed, or measured, massflow rate to the maximum massflow rate, namely the massflow rate resulting from quasi-one-dimensional theory. This ratio is termed discharge coefficient.

In this chapter, the influence of the fluid molecular complexity and total thermodynamic state on the discharge coefficient of supersonic nozzles is studied. The adapted operation of supersonic nozzles in both the ideal, dilute-gas regime and in the non-ideal compressible-fluid regime is considered. Guardone (2015) applied the linearized theory of Sauer to solve the transonic perturbation potential equation in the vicinity of the nozzle throat and expressed the discharge coefficient analytically as function of the nozzle radius of curvature at the throat r_t and of the reference (sonic) value of the fundamental derivative of gasdynamics $\bar{\Gamma}$. The analysis presented in this chapter represent a follow-up to the work by Guardone (2015). An analytical expression for the discharge coefficient is proposed, which holds for both planar and axisymmetric nozzles. Adapted nozzle flows at varying fluid molecular complexity, reservoir conditions, and geometrical configuration of the throat region are simulated numerically with SU2, holding fixed the supersonic exhaust Mach number $M_e = 2$. A grid dependence study is carried out to determine the suitable discretization to capture the nozzle massflow rate and an unexpectedly large number of elements (about 1 million) is found to be required for grid convergence. The shape of the sonic line and the computed massflow rate are assessed against the linearized theory of Sauer and, for both ideal and non-ideal flows, a good agreement with the theory is found for the largest r_t, consistently with the range of applicability of Sauer's formulation.

The structure of the chapter is as follows. In section 4.1, an analytical expression for the discharge coefficient of adapted planar and axisymmetric nozzles is derived from small pertubation theory and the procedure for the numerical verification of theoretical predictions is introduced. Results are presented and discussed 4.2. In paragraph 4.3, final remarks and comments are given.

4.1 Methodology

The discharge coefficient of a chocked supersonic nozzle is defined as:

$$C_D = \frac{\dot{m}}{\dot{m}_{1\mathrm{D}}}, \tag{4.1}$$

where $\dot{m}$ is the actual massflow rate per unit height across the throat section and $\dot{m}_{1\mathrm{D}}$ is the massflow rate resulting from quasi-one-dimensional theory. The massflow rate $\dot{m}$ discharged by the nozzle can be evaluated by integrating the momentum density $\rho\mathbf{u}$ across the nozzle throat section, once a solution for the transonic flow in the vicinity of the throat is available.

For a chocked gasdynamic nozzle, the expression of the critical massflow rate resulting from the quasi-one-dimensional theory is $\dot{m}_{1\mathrm{D}} = \rho^* c^* A^*$, where ρ^* and c^* are the density and speed of sound evaluated in sonic conditions and A^* indicates the minimum area section. For ideal-gas flows, the ratio between total and sonic flow variables is constant and depends only on the specific heat ratio γ. For NICFD flows, the expansion process occurring in a de Laval nozzle depends on the value of the fundamental derivative of gasdynamics Γ, which in turn depends on reservoir

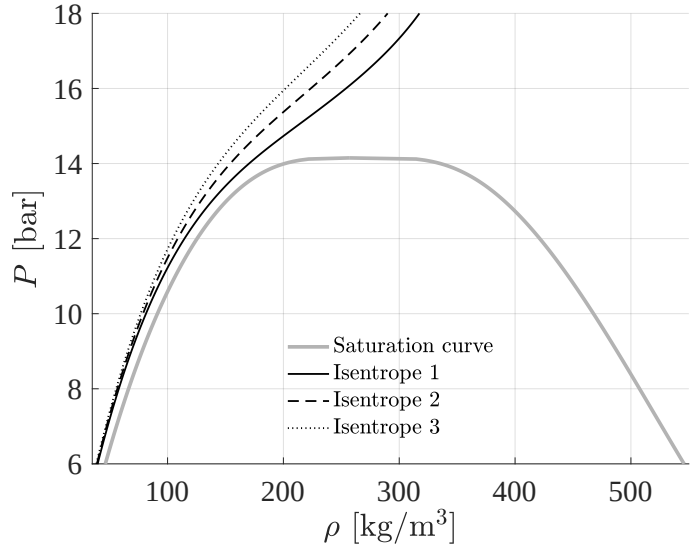

Figure 4.1: P-ρ diagram for siloxane fluid MDM. On the diagram, three isentropes are reported, which represent reservoir thermodynamic states. The diagram is created using the SW EoS of Thol *et al.* (2017)

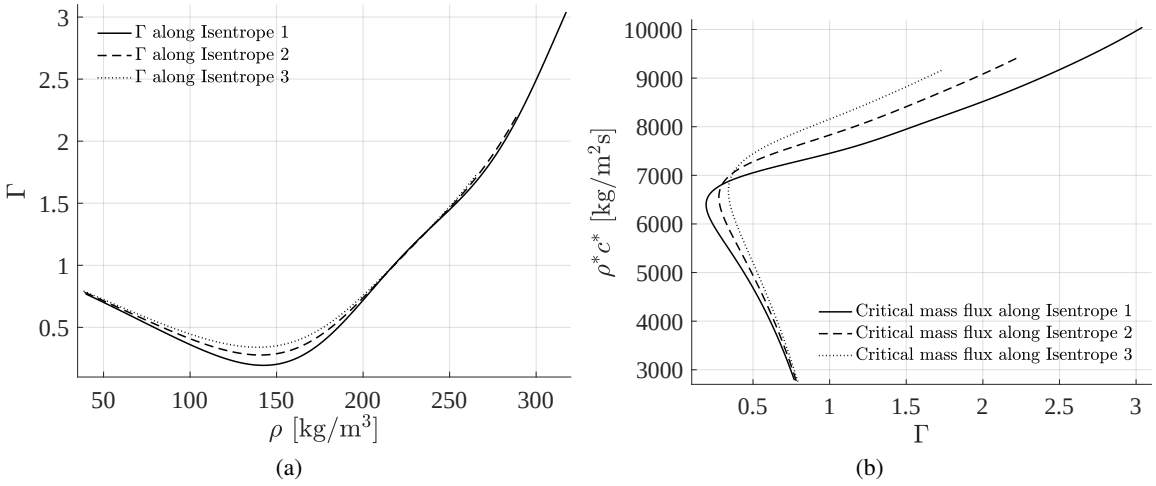

Figure 4.2: (a) Fundamental derivative of gasdynamics Γ as function of density ρ along the three reference isentropes reported in Fig. 4.1 and (b) Critical mass flux per unit area $\rho^* c^*$ as function of the fundamental derivative Γ computed in the reservoir conditions defined by the isentropes of Fig. 4.1

conditions (see paragraph 1.2.2 and eq. 1.33). In the non-ideal regime, the critical massflow rate $\dot{m}_{1D}$ thus depends on both the fluid properties and on the reservoir thermodynamic state.

To unveil such dependence, isentropic expansions taking place in the subcritical and supercritical vapour phase of siloxane fluid MDM (octamethyltrisiloxane $C_8H_24O_2Si_3$) are considered. The thermodynamic states lying along the three isentropes reported on the P-ρ diagram of Fig. 4.1 are taken here as reference reservoir conditions, from which the sonic massflow rate is computed using the quasi-one dimensional flow model. All the isentropes move from supercritical vapour states and enter the non-ideal region of $0 < \Gamma < 1$. Along the three isentropes, the fundamental derivative of gasdynamics varies with density as reported in Fig. 4.2a. The states lying along each

isentrope ($s = \bar{s}$) represent reservoir thermodynamic states ($P^t, \bar{s}$). From ($P^t, \bar{s}$), the specific total enthalpy is calculated as $\bar{h}^t = h^t(P^t, \bar{s})$ using the SW model of Thol *et al.* (2017). The thermodynamic state in sonic conditions, defined by the entropy $\bar{s}$ and by the unknown value of the pressure P^* in sonic conditions, results from the solution of the energy conservation law of the quasi-one-dimensional model, which reads $\bar{h}^t = h(P^*, \bar{s}) - 1/2c^{*2}(P^*, \bar{s})$. In Fig. 4.2b, the critical mass flux per unit area in the sonic state $\rho^* c^*$ is reported as function of the fundamental derivative of gasdynamics Γ. The critical mass flux per unit area given on y-axis is the one resulting from the reservoir states along the three selected isentropes of Fig. 4.1, while the values of Γ reported on the x-axis of Fig. 4.2b are the ones computed along the three isentropes of Fig. 4.1, namely in the reservoir thermodynamic state. The plot of Fig. 4.2b clearly shows that the critical massflow rate strongly depends on Γ, which in turn embeds non-ideal flow behaviour and its dependence on reservoir conditions.

As it will be shown throughout the chapter, the discharge coefficient defined by eq. 4.1 strongly depends on the properties of the working fluid and on the reservoir thermodynamic conditions. However, this parameter does not provide a direct measure of the influence of fluid properties and reservoir conditions on the actual massflow rate discharged by a nozzle. Rather, it is to be interpreted as a measure of the massflow defect caused by flow multi-dimensionality.

In the following analysis, two complementary approaches are applied to the computation of the nozzle discharge coefficient. First, a closed-form expression for the discharge coefficient is derived analytically, in order to highlight the functional dependence between the discharge coefficient and relevant design parameters. Once this functional dependence is made explicit, a set of converging-diverging nozzles is designed at fixed exhaust Mach number and at varying geometrical configuration of the throat section, working fluid and operating conditions. The adapted operation of such nozzles is simulated numerically using SU2 and the massflow rate discharged by each nozzle is computed by integrating the numerical solution across the throat section.

4.1.1 An analytical expression for the discharge coefficient from small pertubation theory

The determination of a closed-form solution to the transonic flow in the throat region of a chocked nozzle can be accomplished by applying a small-perturbation technique to the governing equations for two-dimensional and axisymmetric irrotational flows, provided the total enthalpy h^t and entropy s are uniform over the entire flow-field, as detailed in Guardone (2015). By virtue of the well-known Crocco's theorem, two-dimensional flows featuring uniform total enthalpy h^t and entropy s are irrotational, as it is the case for steady isentropic nozzle flows. The governing equations for two-dimensional irrotational flows read

$$\begin{aligned} &(u^2 - c^2)u_x + (v^2 - c^2)v_y + 2uvu_y = 0 \\ &u_y - v_x = 0 \\ &c = c\left(\|\mathbf{u}\|\right) \end{aligned} \tag{4.2}$$

where x and y are the spatial coordinates, subscripts indicate partial derivatives, c is the speed of sound, and (u, v) are the velocity components in the x and y directions. The functional relationship $c = c(\|\mathbf{u}\|)$ in the third of Eq. 4.2 can be derived from an appropriate EoS. Indeed, as already observed in paragraph 2.3, if the entropy s and enthalpy h are chosen as independent thermodynamic variables, it can be easily shown that, for two-dimensional flows exhibiting uniform h^t and s throughout the domain, the following relation holds:

$$c^2 = c^2(s, h) = c^2\left(s, h^t - \frac{1}{2}\|\mathbf{u}\|^2\right) = c^2\left(\|\mathbf{u}\|^2\right)$$

Since the velocity field $\mathbf{u}$ is irrotational, it can be expressed as the gradient of a scalar potential Φ as:

$$\mathbf{u} = \begin{pmatrix} u \\ v \end{pmatrix} = \nabla\Phi \tag{4.3}$$

Substituting Eq. 4.3 into the first of Eq. 4.2, the well-known velocity potential equation is obtained (see e.g. Zucrow & Hoffman (1977)):

$$(\Phi_x^2 - c^2)\Phi_{xx} + 2\Phi_x\Phi_y\Phi_{xy} + (\Phi_y^2 - c^2)\Phi_{yy} = 0 \tag{4.4}$$

At the nozzle throat, the flow is essentially one-dimensional and sonic, thus a reference state can be set, which is characterized by a velocity module equal to the critical speed of sound $\|\bar{\mathbf{u}}\| = c^*$ and a unit Mach number $\bar{M} = 1$. In the following, the velocity potential and derived quantities are written as a sum of a reference or average contribution, marked with an overbar, and a perturbation variable, marked with a tilde. By setting the sonic state at the throat as the reference state, and by introducing a nondimensional perturbation velocity potential $\tilde{\phi}$ defined by

$$\Phi = \|\bar{\mathbf{u}}\|(x + \tilde{\phi}), \tag{4.5}$$

Guardone (2015) proposed a formulation of the small-perturbation problem for the transonic flow ($\bar{M} \sim 1$) in the vicinity of the nozzle throat, which is valid for non-ideal compressible fluids featuring a value of the fundamental derivative of gasdynamics $\bar{\Gamma}$ in the reference state of $\mathcal{O}(1)$, that reads

$$\left[\bar{M}^2 - 1 + 2\bar{\Gamma}\bar{M}^2\tilde{\phi}_x\right]\tilde{\phi}_{xx} - \tilde{\phi}_{yy} = 0 \tag{4.6}$$

which holds for planar nozzles. For a PIG, Eq. 4.6 reduces to the well-known expression

$$\left[\bar{M}^2 - 1 + (\gamma + 1)\bar{M}^2\tilde{\phi}_x\right]\tilde{\phi}_{xx} - \tilde{\phi}_{yy} = 0 \tag{4.7}$$

Equations 4.6 and 4.7 differ only for the constant multiplying the term $\tilde{\phi}_x\tilde{\phi}_{xx}$. Following Zucrow & Hoffman (1977), a more general expression of Eq. 4.6 is proposed here, which introduces a parameter, δ, whose value is 0 for planar nozzles and 1 for axisymmetric nozzles:

$$y\left[\bar{M}^2 - 1 + 2\bar{\Gamma}\bar{M}^2\tilde{\phi}_x\right]\tilde{\phi}_{xx} - y\tilde{\phi}_{yy} - \delta\tilde{\phi}_y = 0 \tag{4.8}$$

Moreover, since the reference value of Γ is of $\mathcal{O}(1)$, i.e. the same order of the PIG specific heat ratio γ, the approximate solution method proposed by Sauer (1947) can be applied without modifications to the solution of 4.8, to obtain the perturbation potential $\tilde{\phi}$:

$$\tilde{\phi}(\hat{x}, y) = \frac{1}{2}\alpha\hat{x}^2 + \frac{\Gamma\bar{\alpha}^2\hat{x}}{1+\delta}y^2 + \frac{\bar{\Gamma}^2\alpha^3}{2(3+\delta)(1+\delta)}y^4 \tag{4.9}$$

where

$$\begin{aligned} \hat{x} &= x - x_t - \frac{1}{3}\bar{\Gamma}\alpha H^2, \\ \alpha &= \sqrt{\frac{1}{2\bar{\Gamma}r_t H}}, \end{aligned} \tag{4.10}$$

with $r_t = R_t/H$ the *non-dimensional* radius of curvature of the nozzle profile at the throat, given by the ratio of the dimensional throat radius of curvature R_t to the height of the wall H at $x = x_t$, namely at the throat section. The flow velocity components are finally obtained from the nondimensional perturbation velocity potential $\tilde{\phi}$:

$$\tilde{\mathbf{u}}(\hat{x}, y) = \begin{pmatrix} \tilde{u}(\hat{x}, y) \\ \tilde{v}(\hat{x}, y) \end{pmatrix} = \begin{pmatrix} \tilde{\phi}_{\hat{x}} \\ \tilde{\phi}_y \end{pmatrix} = \begin{pmatrix} \alpha\hat{x} + \dfrac{\bar{\Gamma}\alpha^2\hat{x}y}{1+\delta} \\ \dfrac{2\bar{\Gamma}\alpha^2\hat{x}y}{1+\delta} + \dfrac{2\bar{\Gamma}^2\alpha^3}{(3+\delta)(1+\delta)}y^3 \end{pmatrix} \tag{4.11}$$

An analytical expression for the discharge coefficient of planar and axisymmetric nozzles is now derived, following the approach introduced by Guardone (2015) for planar nozzles.

The general definition of discharge coefficient for a chocked supersonic nozzle is given by eq. 4.1. For the case examined here, $\dot{m}_{1\mathrm{D}} = \bar{\rho}\bar{u}$, while the actual massflow rate $\dot{m}$ can be calculated by integrating the momentum density across the throat section. If the origin of the x axis is set the geometrical throat, the expression for $\dot{m}$ reads:

$$\dot{m} = \int_0^H \rho(0, y) u(0, y) \frac{\mathrm{d}y}{H} \tag{4.12}$$

where the momentum density in the x direction, given by the product $\rho(0, y)u(0, y)$ in the integrand function, can be expressed in terms of sonic and perturbation variables as:

$$\begin{aligned} \rho(0, y)u(0, y) &= \left[\bar{\rho} + \bar{\rho}\tilde{\rho}(0, y)\right] \left[\bar{u} + \bar{u}\tilde{u}(0, y)\right] \\ &= \bar{\rho}\bar{u} \left[1 + \tilde{\rho}(0, y) + \tilde{u}(0, y) + \tilde{\rho}(0, y)\tilde{u}(0, y)\right] \end{aligned} \tag{4.13}$$

The function $\tilde{u}(0, y)$ can be immediately derived from eq. 4.11 by evaluating the x-component of the velocity at the throat section, namely at $\hat{x} = -\bar{\Gamma}\alpha H^2/3$ and $y = 0$. The derivation of the expression for $\tilde{\rho}(0, y)$, instead, is less straightforward, since the density needs first to be expressed as function of the flow velocity. Similarly to the speed of sound, the density ρ depends only on the velocity module $\|\mathbf{u}\|$, denoted in the following as w. If the entropy s and enthalpy h are chosen as independent thermodynamic variables, the following relation holds:

$$\rho = \rho(s, h) = \rho\left(\bar{s}, \bar{h}^t - \frac{1}{2}w^2\right) = \rho\left(w^2\right),$$

where the uniform h^t and s throughout the domain are indicated as $\bar{h}^t$ and $\bar{s}$, respectively. An approximate expression for the function $\rho(w^2)$ can be derived from its Taylor-series expansion around the sonic value $\bar{\rho}$:

$$\rho(w^2) = \bar{\rho} + \left.\frac{\mathrm{d}\rho}{\mathrm{d}(w^2)}\right|_{\bar{w}^2} \left(w^2 - \bar{w}^2\right) + \frac{1}{2} \left.\frac{\mathrm{d}^2\rho}{\mathrm{d}(w^2)^2}\right|_{\bar{w}^2} \left(w^2 - \bar{w}^2\right)^2 + \mathcal{O}\left(\left[\Delta w^2\right]^3\right) \tag{4.14}$$

The first and second order derivatives of the perturbation density function can thus be expressed as follows:

$$\begin{aligned} \frac{\mathrm{d}\rho}{\mathrm{d}(w^2)} &= \left(\frac{\partial\rho}{\partial h}\right)_s \frac{\mathrm{d}h}{\mathrm{d}(w^2)} = -\frac{1}{2}\frac{\rho}{c^2} \\ \frac{\mathrm{d}^2\rho}{\mathrm{d}(w^2)^2} &= \frac{3 - 2\bar{\Gamma}}{4}\frac{\rho}{c^4} \end{aligned} \tag{4.15}$$

Combining eq. 4.14 and 4.15 and setting $\bar{M} = \bar{w}/c = 1$, the perturbation density reads:

$$\begin{aligned} \tilde{\rho}(0, y) = &-\frac{1}{2}\left(2\tilde{u}(0, y) + \tilde{u}^2(0, y) + \tilde{v}^2(0, y)\right) \\ &+ \frac{1}{2}\left(3 - 2\bar{\Gamma}\right)\tilde{u}^2(0, y) \\ &+ \mathcal{O}\left(\tilde{u}^3, \tilde{v}^3\right) \end{aligned} \tag{4.16}$$

where only the first and second order terms of the perturbation velocity are retained. Substituting eq. 4.12 into the definition of discharge coefficient eq. 4.1, and substituting the above equation

4.16 into eq. 4.13, the discharge coefficient reads:

$$\begin{aligned} C_D &= 1 + \int_0^H \left(\tilde{\rho}(0,y) + \tilde{u}(0,y) + \tilde{\rho}(0,y)\tilde{u}(0,y)\right) \frac{\mathrm{d}y}{H} \\ &\approx 1 - \int_0^H \left(\bar{\Gamma}\tilde{u}^2(0,y) + \frac{1}{2}\tilde{v}^2(0,y)\right) \frac{\mathrm{d}y}{H} \end{aligned} \tag{4.17}$$

Analytical calculation of the above integral, where the perturbation velocity components $\tilde{u}$ and $\tilde{v}$ (eq. 4.11) are evaluated at the throat section, leads to the final expression for the discharge coefficient:

$$C_D = 1 - C_1 \frac{\bar{\Gamma}}{r_t^3} \left(r_t + C_2\right) \tag{4.18}$$

where C_1 and C_2 are constant coefficients depending only on the parameter δ:

$$\begin{aligned} C_1 &= \frac{2\delta^2 + 2\delta + 3}{15\delta^2 + 90\delta + 135} = \begin{cases} \dfrac{1}{45} & \text{for } \delta = 0 \\ \dfrac{7}{240} & \text{for } \delta = 1 \end{cases} \\ C_2 &= \frac{8\delta + 8}{161\delta^2 + 56\delta + 84} = \begin{cases} \dfrac{2}{21} & \text{for } \delta = 0 \\ \dfrac{6}{301} & \text{for } \delta = 1 \end{cases} \end{aligned} \tag{4.19}$$

The discharge coefficient (eq. 4.18) shows a linear dependence on the fundamental derivative of gasdynamics in the reference sonic state $\bar{\Gamma}$ and a dependence on the radius of curvature at the throat section to the power $1/r_t^2$ and $1/r_t^3$. For planar nozzles ($\delta = 0$), eq. 4.18 simplifies to:

$$C_D = 1 - \frac{1}{45} \frac{\bar{\Gamma}}{r_t^3} \left(r_t + \frac{2}{21}\right) \tag{4.20}$$

which is the same expression derived by Guardone (2015). In the same work, the author proved that retaining higher-order terms in the Taylor-series expansion of the perturbation density (eq. 4.16) does not improve the accuracy of the expression for the discharge coefficient, if compared to the numerical integration of the first of eq. 4.17.

4.1.2 Evaluation of the discharge coefficient from numerical simulations

In the previous paragraph, an analytical expression for the discharge coefficient of planar and axisymmetric nozzles was derived. The discharge coefficient was found to depend on $\bar{\Gamma}$ and r_t. In the remainder of the chapter, the analysis is restricted to planar nozzles. Different nozzle geometries are designed for a fixed exhaust Mach number $M_e = 2$, at varying $\bar{\Gamma}$ and r_t, namely at varying fluid molecular complexity, reservoir conditions and radius of curvature of the nozzle profile at the throat. The SU2 CFD suite is applied to the simulation of the adapted operation of such nozzles, in order to draft comprehensive discharge coefficient charts, giving the discharge coefficient as function of the design parameters $\bar{\Gamma}$ and r_t.

Design and simulation parameters are summarized in Tab. 4.1.

Expansions in the ideal-gas regime are considered first. Euler simulations are performed using the PIG EoS, and the constant specific heat ratio is varied to account for the molecular complexity of different working fluids. The lowest value of γ, namely 1.017, is the constant specific heat ratio for the molecularly-complex siloxane fluid MDM, computed in the dilute-gas limit. The

	γ				$\bar{\Gamma}$
r_t	1.017	1.4	5/3	1.33	2
2	PIG	PIG	PIG	PIG	vdW
5	PIG	PIG	PIG	PIG	vdW
10	PIG	PIG	PIG	PIG	vdW

Table 4.1: Summary of design and simulation parameters. For each case, the thermodynamic model adopted for nozzle design and simulation is specified. PIG: Polytropic Ideal Gas EoS, vdW: van der Waals EoS

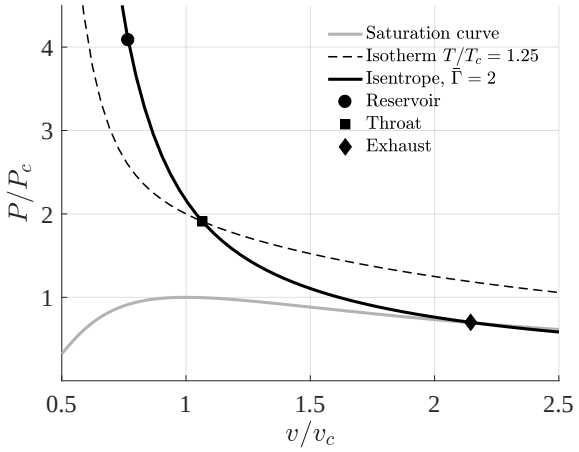

Figure 4.3: Simulated isentropic expansion of CO_2, featuring $\bar{\Gamma} = 2$

other values of γ are 1.4, i.e. the constant specific heat ratio for air, and 5/3, which is the constant specific heat ratio for a monoatomic gas.

An expansion occurring in the non-ideal compressible-fluid regime is then simulated using the vdW EoS. CO_2 is considered as working fluid, which undergoes an expansion from reservoir conditions $P^t = 297$ bar, $T^t = 179°C$ to exhaust conditions $P_e = 52$ bar, $M_e = 2$ and achieves a sonic state characterized by $\bar{\Gamma} = 2$. The same expansion is simulated using the PIG model, within a nozzle designed for $\gamma = 1.33$. The value of γ is chosen so that the parameter $\delta = R/c_v$ is the same in both models. Following Thompson (1988), the parameter R/c_v for CO_2 is set to 0.33, which yields $\gamma = 1 + \delta = 1.33$. In order to analyze the dependence of the discharged massflow rate on flow non-ideality, comparison is drawn between the massflow rates resulting from the expansion processes in the $\bar{\Gamma} = 2$ and $\gamma = 1.33$ nozzles, simulated using the vdW and PIG EoS, respectively. The isentropic expansion of CO_2, modeled using the vdW EoS, is represented in the pressure-specific volume diagram of Fig. 4.3, where pressure and specific volume are made dimensionless with the critical pressure and critical specific volume.

For each parameter combination reported in Tab. 4.3, a different nozzle is designed. The supersonic portions of the nozzles are designed using the method of characteristics presented in paragraph 2.3. The throat region is represented by a circular arc, which is joined smoothly to the inlet section through a 5^{th} order polynomial. Figure 4.4 reports the nozzle geometries designed using the method of characteristics (see chapter 2) under the PIG model for a fixed γ and at varying r_t (Figure 4.4a), and for a fixed r_t and at varying γ (Figure 4.4b). For all nozzles, the contraction ratio, defined as the ratio of the inlet area A_i to the throat area A_t is 2, and the ratio of the convergent length L_c to the divergent length L_d is 1.5. Consistently with results presented in

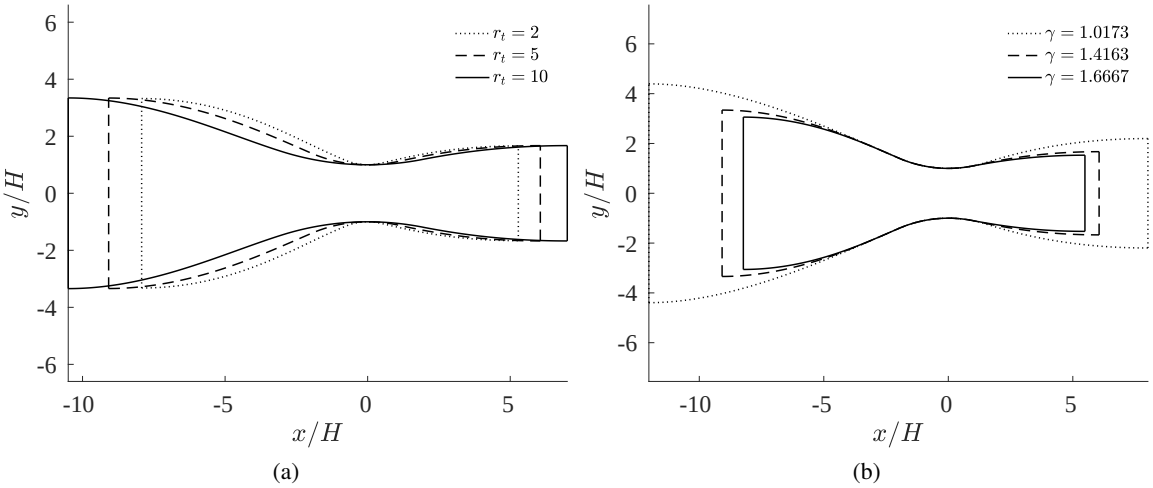

Figure 4.4: Nozzle geometries designed for a fixed exhaust Mach number $M_e = 2$, at varying γ and r_t. (a) $\gamma = 1.4$ is fixed, r_t is varied, (b) $r_t = 5$ is fixed, γ is fixed

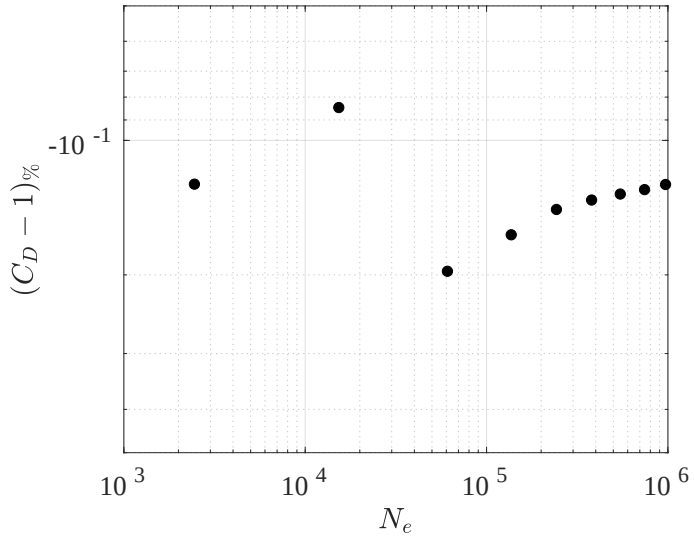

Figure 4.5: Grid convergence evaluated in the case $\gamma = 1.4$, $r_t = 5$. The massflow defect $(C_D - 1)_{\%}$ is reported as function of the number of elements N_e of the computational grid

paragraph 4.4, the higher the fluid molecular complexity, the longer the diverging portion of the nozzle.

For all nozzles, two-dimensional, Euler simulations are run on unstructured triangular grids. The sonic lines computed from numerical simulations are compared to the ones resulting from the solution of the perturbation velocity potential equation. Sonic lines are defined by the following equation, obtained by setting $\tilde{u} = 0$ in eq. 4.11:

$$x = -\frac{\bar{\Gamma}\alpha y^2}{1+\delta}, \tag{4.21}$$

Highly-distorted sonic lines indicate that the corresponding flows deviate significantly from the one-dimensional flow condition, which in turn is characterized by a straight sonic line located at the nozzle geometrical throat. Flows featuring sonic lines approaching the straight segments

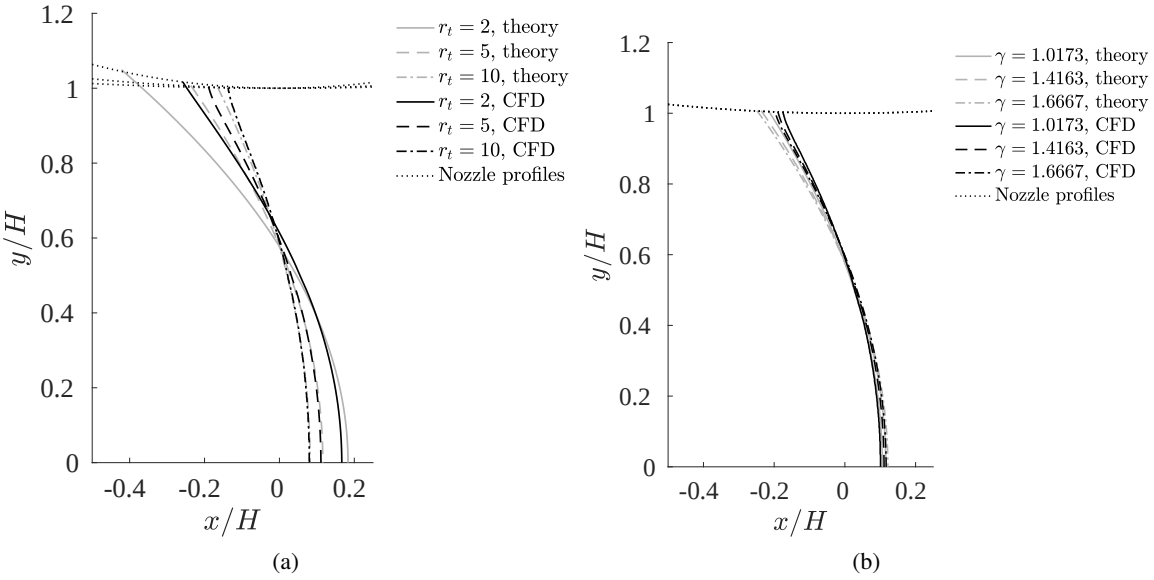

Figure 4.6: Sonic lines from numerical simulations and small-perturbation theory. (a) $\gamma = 1.4$ is fixed, r_t is varied, (b) $r_t = 5$ is fixed, γ is varied

typical of a one-dimensional flow are expected to yield higher massflow rates, since deviation from the one-dimensional flow condition is less significant. The theoretical value of the discharge coefficient, computed from eq. 4.20, is then compared to the one resulting from the numerical solution of the two-dimensional flow-field. Specifically, the nozzle massflow rate is computed by integrating the x-component of the momentum density[1] across the geometrical throat section.

For the case $\gamma = 1.4$, $r_t = 5$, a grid dependence study is carried out to determine the suitable discretization to capture the nozzle massflow rate. Results are reported in Fig. 4.5, which reports the percentage massflow defect $(C_D - 1)_{\%}$ as function of the number of elements N_e of the computational grid. A very large number of elements ($\mathcal{O}(10^6)$) is found to be required for grid convergence. The grid spacing guaranteeing grid convergence is adopted in all simulations. The maximum element size is of $\mathcal{O}(H/100)$, and the minimum element size of $\mathcal{O}(H/200)$.

4.2 Results and discussion

In the following paragraph 4.2.1, the influence of throat radius of curvature, fluid molecular complexity and process conditions on the shape of the sonic line and on the discharge coefficient is discussed. In paragraph 4.2.2, the influence of the shape of the converging portion on the discharged massflow rate is investigated.

4.2.1 Influence of throat radius, fluid molecular complexity and reservoir conditions on the discharge coefficient

Expansions in the ideal-gas regime are analyzed first. The specific heat ratio and throat radius of curvature are varied as indicated by the first three rows and columns of Tab. 4.1. The sonic lines ($M = 1$ isolines) obtained at fixed $\gamma = 1.4$ and at varying r_t are reported in Fig. 4.6a, while the sonic lines obtained at fixed $r_t = 5$ and at varying γ are reported in Fig. 4.6b. Results reported

[1] The x-component of the momentum density results directly from the numerical solution of the flow-field calculated with SU2 (cf. paragraph 2.2)

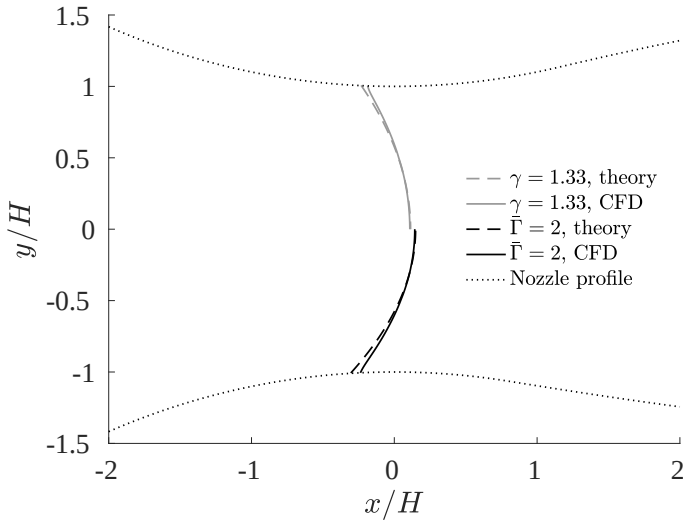

Figure 4.7: Sonic lines from vdW (top) and PIG (bottom) from numerical simulations and small-perturbation theory

in Fig. 4.6 show that the sonic line location approaches the geometrical throat at increasing r_t and at decreasing γ, or, in other words, at increasing fluid molecular complexity. For the flow conditions examined here, the most relevant deviations from the one-dimensional flow behaviour are observed for the monoatomic fluid ($\gamma = 1.6667$), and for a throat curvature radius of $r_t = 2$, as expected from relation 4.20. Agreement between the sonic lines from the inviscid simulation of SU2 and from the small-perturbation theory is better at the nozzle axis than in the close proximity of the nozzle contour. The most relevant deviations between numerical and theoretical results are found for the nozzles having $r_t = 2$. Indeed, the approximate method of Sauer (1947) used to solve the perturbation potential equation in the throat region gives reasonably accurate results for nozzles featuring large r_t.

The sonic lines resulting from an expansion taking place in the non-ideal compressible-fluid regime are reported in Fig. 4.7 to analyze the effect of process non-ideality on the flow configuration in the vicinity of the throat. The thermodynamic conditions for the expansion process are given in paragraph 4.1.2 and are reported in the P-v diagram of Fig. 4.3. In Fig. 4.7, results are reported for a fixed throat radius $r_t = 5$. In the top portion of the plot, the sonic lines for the $\bar{\Gamma} = 2$ nozzle are reported, while the bottom portion shows the sonic lines obtained for the $\gamma = 1.33$ nozzle. The $\bar{\Gamma} = 2$ and the $\gamma = 1.33$ nozzles are designed and simulated for the same process conditions using the vdW and PIG EoS, respectively. The sonic lines obtained for the $\bar{\Gamma} = 2$ nozzle feature a more significant deviation from the one-dimensional configuration as compared to the sonic lines for the $\gamma = 1.33$ nozzle. In both cases, a good agreement with the small-perturbation theory is observed.

In summary, the shape of the sonic line is found to be influenced to a greater extent by the radius of curvature of the nozzle at the throat section and to a lesser extent by the fluid molecular complexity, in accordance with 4.18. When expansions taking place in the non-ideal compressible-fluid regime are considered, the layout of the transonic flow at the throat is seen to be influenced by the thermodynamic model used to perform both the nozzle design and the numerical simulation of the flow-field, once the process conditions and the geometrical configuration of the throat section are held fixed.

For all parameter combinations reported in Tab. 4.1, the discharge coefficients computed from numerical simulations are mapped on the massflow-defect charts of Fig. 4.8. The plots of Fig. 4.8

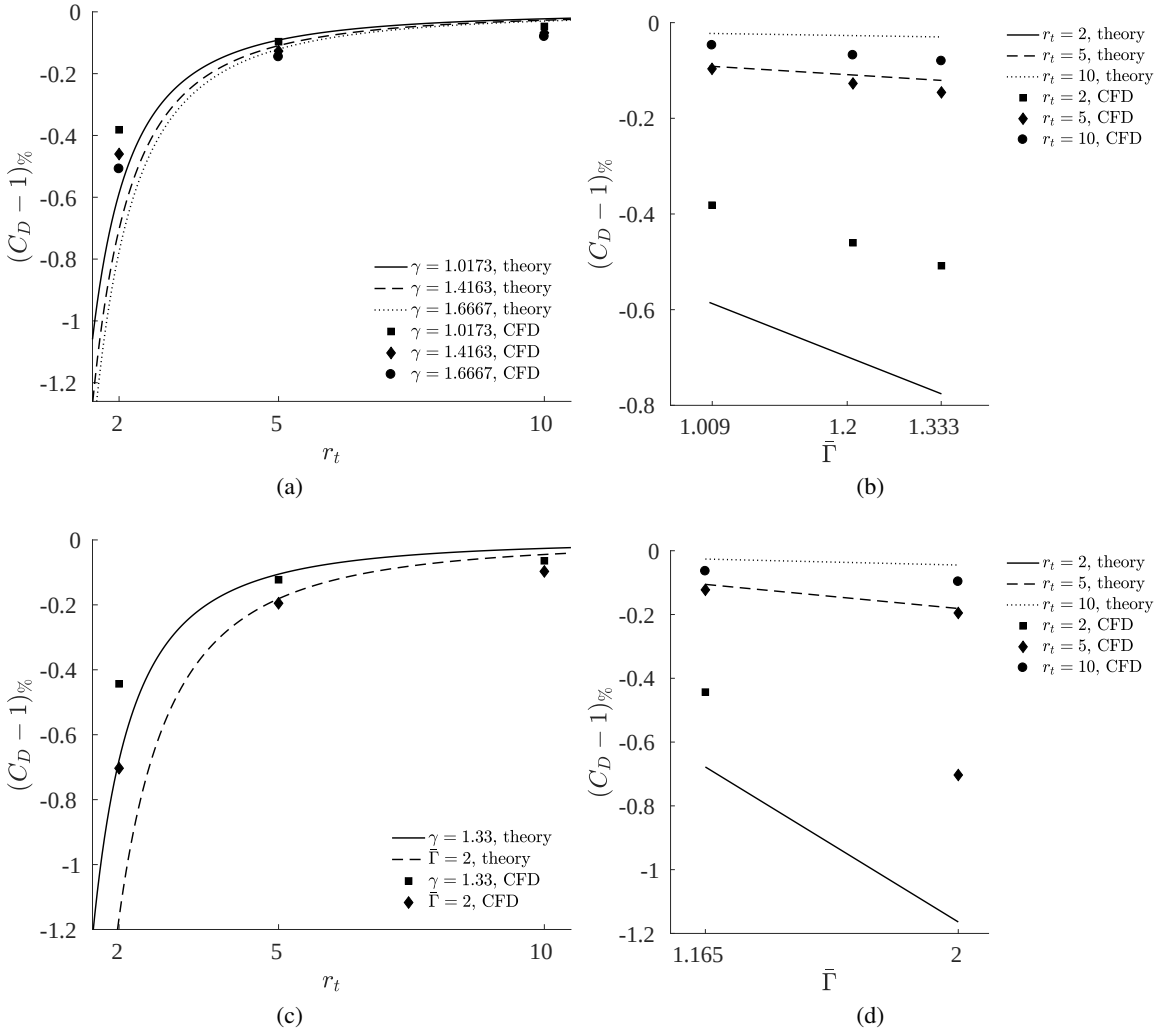

Figure 4.8: Discharge coefficient charts. The percentage massflow defect $(C_D - 1)_{\%}$ from CFD and eq. 4.20 is reported as function of the throat radius r_t (a), (c) and of the fundamental derivative in the sonic state $\bar{\Gamma}$ (b), (d). (a), (b) Ideal-gas case. (c), (d) Non-ideal case: comparison between PIG and vdW treatment of the same expansion process

report the percentage massflow defect $(C_D - 1)_{\%}$ obtained from numerical simulations and from the analytical expression of the discharge coefficient given by eq. 4.20. Comparison between theoretical and numerical results reveals that the numerical method well describes both the dependence of the massflow defect on the fundamental derivative of gasdynamics in the reference state and on the throat radius of curvature. Consistently with the theoretical expression for the discharge coefficient (eq. 4.20), the dependence of the calculated massflow defect on the throat radius of curvature becomes less significant at increasing r_t. It is worth commenting here that the theoretical function expressing the massflow defect is reported on the plots of Fig. 4.8 only for reference, and not for validation purposes. More or less significant deviations between the numerical results and the small-perturbation theory are indeed expected, since numerical simulations solve the complete Euler equations over the entire flow domain, while theoretical results are derived from the solution of a perturbation equation valid in a small portion of the domain in the vicinity of the throat. At the smallest radius of curvature, the deviation between numerical and theoretical results becomes

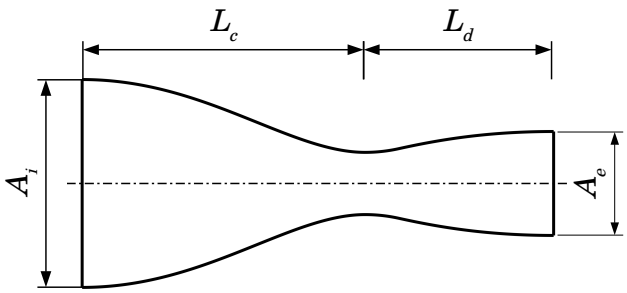

Figure 4.9: Geometrical parameters varied in the design of different converging section, while maintaining the same diverging section designed for $\gamma = 1.4$ and exhaust Mach number $M_e = 2$ using the PIG model

more noticeable, consistently with the range of applicability of the linearized theory of Sauer.

4.2.2 Remarks on the design of the converging portion

The throat region of the nozzles considered so far was defined by a circular arc, joined smoothly to the inlet section through a 5^{th} order polynomial. This design choice was pursued in order to reproduce the geometry of the throat region considered in the theoretical formulation of the small-perturbation problem.

In order to show the dependence of the flow layout in the throat region on the shape of the converging portion, Fig. 4.10 reports the Mach number isolines (white curves) and the sonic lines (black curves) obtained from inviscid simulations run on four different nozzle geometries. The geometry of the diverging portion is the same for all nozzles. Namely, the diverging portion is designed for an exhaust Mach number $M_e = 2$, operating with air modelled as a PIG ($\gamma = 1.4$). The radius of curvature at the throat is $r_t = 5$ and the four different configurations (a)-(d) are obtained by replacing the converging portion. The four converging portions are defined by 5^{th}-order polynomials obtained by imposing derivatives of the geometrical contour up to order second at the inlet and at the throat section. The four convergents are designed at varying ratio of the inlet to exhaust area ratio A_i/A_e and at varying ratio of the length of the converging portion to the length of the diverging portion L_c/L_d (see Fig. 4.9). Qualitatively different configurations for the sonic lines and for the transonic flows in the vicinity of the throat are obtained. The sonic lines are characterized by significantly different shapes and curvatures, thus the four nozzles are expected to discharge four different massflow rates.

It is worth recalling here that, immediately downstream of the throat section, the profile of the diverging portion is defined by a circular arc of nondimensional radius r_t. In this constant-curvature region, named expansion region, the flow is expanded up to the design pressure ratio (cf. paragraph 2.3). For converging portions defined by 5^{th}-order polynomials, the continuity of the radius of curvature (i.e. of the second-order derivative of the profile) is enforced at the throat section, and the profile of the converging portion rigorously assumes the prescribed value of r_t only locally. In this respect, the curvature of the nozzle profile upstream of the throat section is influenced to a greater extent by the overall shape of the convergent rather than by the prescribed value of r_t at the throat section (see Fig. 4.10).

Considering again the design and simulation parameters reported in Tab. 4.1, the numerical analysis presented in the previous paragraph 4.2.1 is repeated here over a new set of nozzle geometries obtained by preserving the previously-designed diverging portions and by replacing the

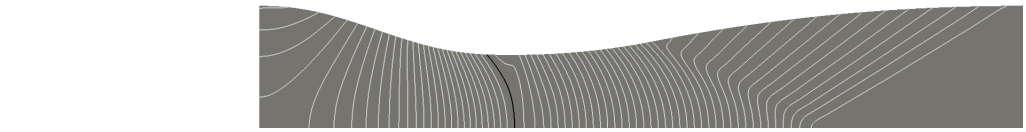

(a) $A_i/A_e = 1$, $L_c/L_d = 0.5$

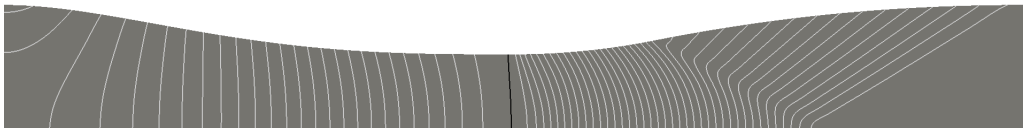

(b) $A_i/A_e = 1$, $L_c/L_d = 0.5$

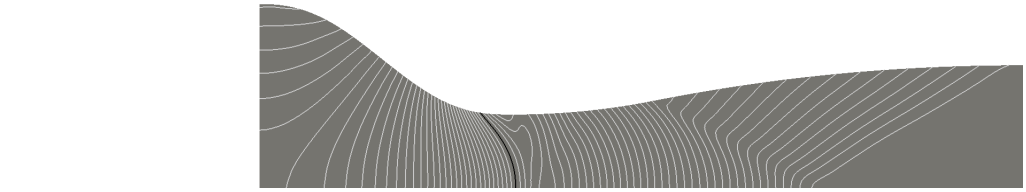

(c) $A_i/A_e = 1.5$, $L_c/L_d = 1$

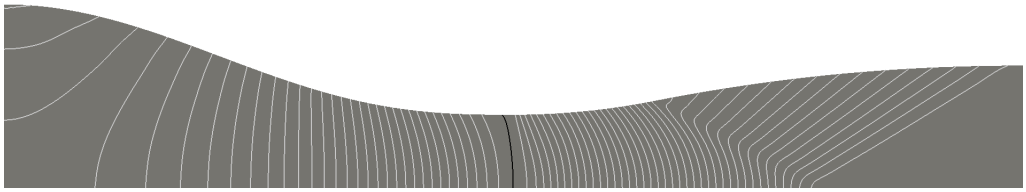

(d) $A_i/A_e = 1.5$, $L_c/L_d = 1$

Figure 4.10: Mach number isolines (white) and sonic line (black) for a set of nozzle geometries. The diverging portion is designed for $M_e = 2$, $\gamma = 1.4$, $r_t = 5$. The four different configurations (a)-(d) are obtained by replacing the converging portion. A_i and A_e indicate the inlet area and the exhaust area, while L_c and L_d indicate the length of the converging and diverging portions.

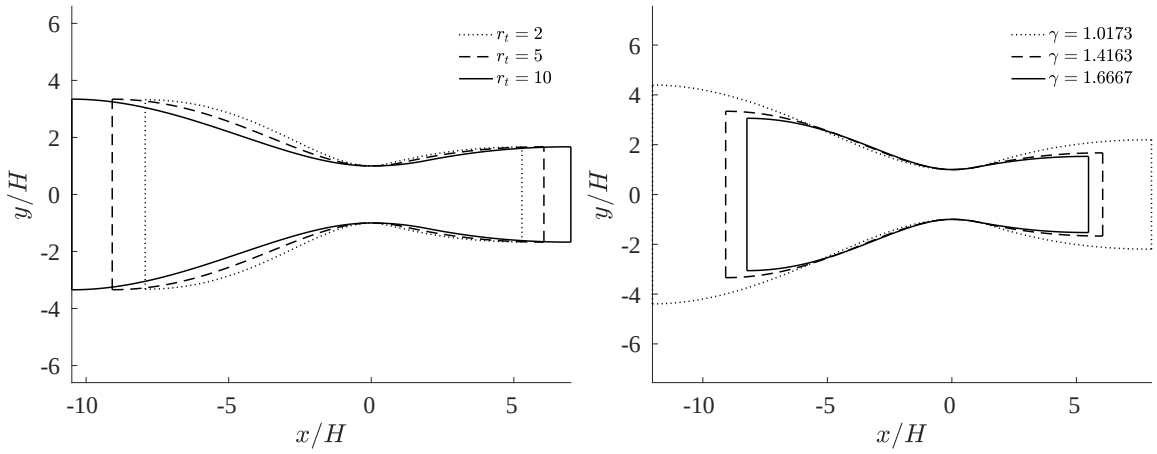

(a) (b)

Figure 4.11: Nozzle geometries designed for a fixed exhaust Mach number $M_e = 2$, at varying γ and r_t. (a) $\gamma = 1.4$ is fixed, r_t is varied, (b) $r_t = 5$ is fixed, γ is fixed. The converging portions are defined by 5^{th}-order polynomials (Type-II convergents)

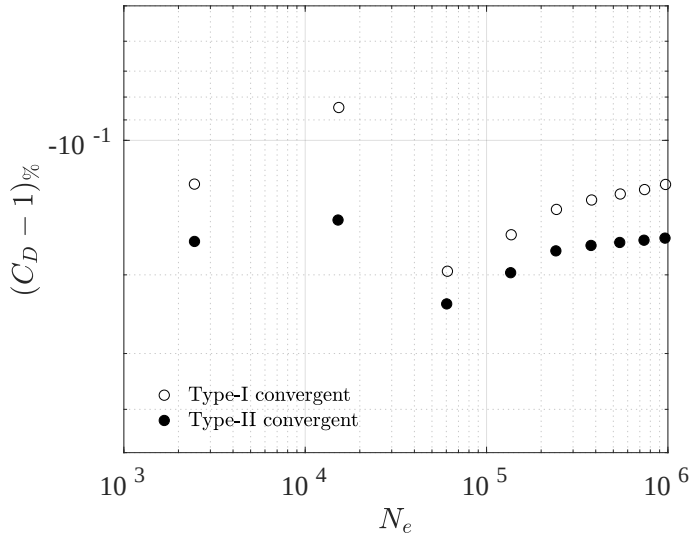

Figure 4.12: Grid convergence evaluated at $\gamma = 1.4$, $r_t = 5$ for convergents of Type-I and Type-II

converging portions only. The new set of converging portions (denoted as Type-II convergents) is defined by 5$^{\text{th}}$-order polynomials performing a smooth transition from the inlet to the throat section. The analysis is restricted here to the ideal-gas case, and simulation parameters are reported in the first three rows and columns of Tab. 4.1. In order to highlight the net dependence of the computed sonic lines and massflow rates on the the shape of the converging portions, the contraction ratio A_i/A_t and the convergent to divergent length ratio L_c/L_d are again set to 2 and 1.5, respectively. Figure 4.11 reports the new nozzle geometries at varying γ and r_t (cf. Fig. 4.4). The solution of the flow-field on the new set of nozzle geometries is expected to exhibit only a slight dependence of the shape of the sonic line and of the computed massflow rate on the design of the converging portion, since, for the chosen aspect ratio parameters, the shape of the converging portion in the throat region matches reasonably well with the curvature of the expansion region.

A grid dependence analysis based on the computed massflow defect is carried out for the case $\gamma = 1.4$, $r_t = 5$. Results are reported in Fig. 4.12, where the massflow defect trend obtained on the original nozzle geometry (characterized by the same divergent and by a different convergent, labelled as Type-I convergent, cf. Fig.4.5) is reported for reference. Similarly to nozzle geometries of Type-I, a large number of elements is found to be required for grid convergence on the computed massflow defect. Moreover, the plot reveals that, independently of grid refinement, the massflow defects computed on the two nozzles having the same divergent and different convergents are different.

Figures 4.13 and 4.14 report the sonic lines obtained at varying γ and r_t and the discharge coefficient chart giving the massflow defect as function of the throat radius of curvature (cf. Fig. 4.6 and 4.8). As expected, the dependence of the shape of the sonic lines on r_t for Type-II geometries (Fig. 4.13a) is less marked than that observed for Type-I geometries (Fig. 4.6a). Finally, the computed values of the massflow defect reported on the discharge coefficient chart of Fig. 4.14 reveal that the dependence of the massflow defect on the fluid molecular complexity is well caught by numerical results also on Type-II geometries, though a less relevant dependence on the throat radius of curvature is observed with respect to results obtained on Type-I nozzles (cf. Fig. 4.8).

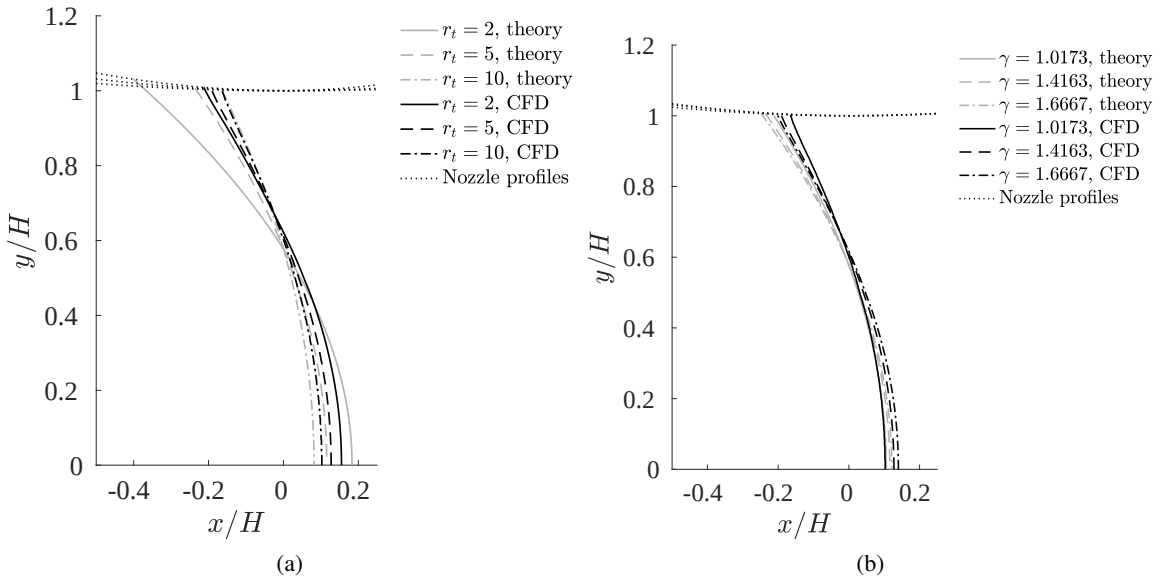

Figure 4.13: Sonic lines from numerical simulations of nozzles with Type-II convergents and small-perturbation theory. (a) $\gamma = 1.4$ is fixed, r_t is varied, (b) $r_t = 5$ is fixed, γ is varied.

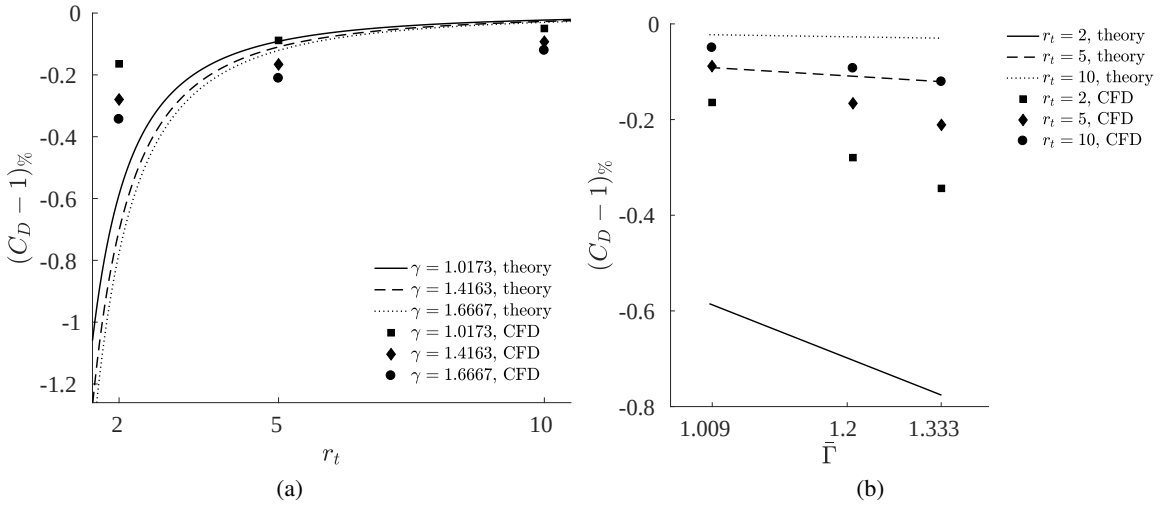

Figure 4.14: Discharge coefficient chart. The massflow defect $(C_D - 1)_{\%}$ from CFD and eq. 4.20 is reported as function of the throat radius r_t (a) and of the fundamental derivative in the sonic state $\bar{\Gamma}$ (b) for Type-II geometries

4.3 Conclusions

Starting from the solution of the perturbation potential equation in the throat region of planar and axisymmetric nozzles, an analytical expression for the discharge coefficient of adapted nozzles was derived. The discharge coefficient was found to depend explicitly on the fundamental derivative of gasdynamics in the sonic state $\bar{\Gamma}$ and on the radius of curvature r_t of the nozzle profile at the throat section. The fundamental derivative of gasdynamics embeds both the molecular complexity of the working fluid and the non-ideal character of process conditions.

The functional dependence of the discharge coefficient on $\bar{\Gamma}$ and r_t was verified numerically, both in the ideal and non-ideal flow regimes. Grid-independent results were obtained using a high grid refinement, which was indeed found to be required to capture the shape of the sonic line and to correctly estimate the nozzle discharge coefficient.

Finally, the discharge coefficient was found to be affected by the shape of the converging portion of the nozzle, even in the case of smooth convergents. Indeed, the shape of the sonic line, and therefore the massflow rate discharged by the nozzle, was found to be dependent on the overall shape of the converging portion, and not only on the local curvature of the nozzle profile at the throat section.

Part II

Oblique waves in the non-ideal regime

5 *Experimental observation of supersonic non-ideal compressible-fluid flows around a diamond-shaped airfoil*

Supersonic NICF flows around a diamond-shaped airfoil are observed experimentally in the TROVA wind tunnel. The airfoil, with semi-aperture $7.5°$ *at leading edge and* $10°$ *at the trailing edge is placed in a uniform supersonic stream (*$M = 1.5$*) of siloxane fluid MDM. The present flow arrangement produces two oblique shocks at the airfoil leading-edge and centered expansion fans at the shoulder. Oblique waves are characterized through independent measurements of pressure, temperature and Mach number, in order to compile a first experimental database dealing with oblique waves in the non-ideal regime, which can be used by the NICFD community for future assessment of thermodynamic models and CFD tools for NICFD flows.*

In all experiments, the fluid is a single-phase vapour. Upstream of the airfoil, the flow conditions are well within the so-called non-ideal compressible-fluid region, thus the shock-expansion pattern originating on the airfoil occurs in the non-ideal regime. Oblique shock waves and expansion fans are studied at varying upstream stagnation conditions, for a set of flow deviation angles obtained by changing the attitude of the model with respect to the wind tunnel axis. Total pressure and temperature are measured in the settling chamber upstream of the nozzle, while the pre-shock, post-shock and post-expansion static pressures are measured at the wind-tunnel lateral wall, at selected locations around the airfoil. Direct measurement of the flow Mach number is provided by schlieren visualizations, which clearly show the Mach waves in the supersonic regions of the flow-field. Experimental results are assessed against the shock-expansion theory for two-dimensional steady flows, complemented with state-of-the-art thermodynamic models.

The present chapter is structured as follows. Paragraph 5.1 describes the experimental set-up, while paragraph 5.2 describes the tested flow regimes and the criteria for data representation. In paragraph 5.3, results are assessed against the inviscid shock-expansion theory and comments upon the non-ideal nature of the oblique waves under scrutiny are provided. Concluding remarks are given in paragraph 5.4.

5.1 Experimental set-up

All the experiments described in the present chapter are carried out in the TROVA wind tunnel. The reader is referred back to paragraph 2.1 for details about the test-rig and measurement techniques implemented, and to paragraph 2.4 for reference results on non-ideal expansions in supersonic nozzles. In the experimental campaign presented in this chapter, the layout of the test section presented in paragraph 2.3 is modified to accommodate the model of a supersonic airfoil. A brief description of the test rig and instrumentation is recalled, while here focus is placed on the new geometrical configuration of the test section for the observation of oblique waves in the non-ideal compressible-fluid regime.

In the present campaign, the TROVA is operated as a conventional blow-down supersonic wind tunnel. The de Laval nozzle discharges a uniform supersonic stream in a constant-area duct, where a diamond-shaped airfoil is placed. Figure 5.1a shows the installed test section, while Fig. 5.1b shows the mirror-polished steel plate accommodating the planar nozzle and the diamond airfoil. The locations marked with white dots in Fig. 5.1b correspond to the pressure taps used for static pressure measurements. Pressure transducers are mounted as illustrated in Fig. 5.1c.

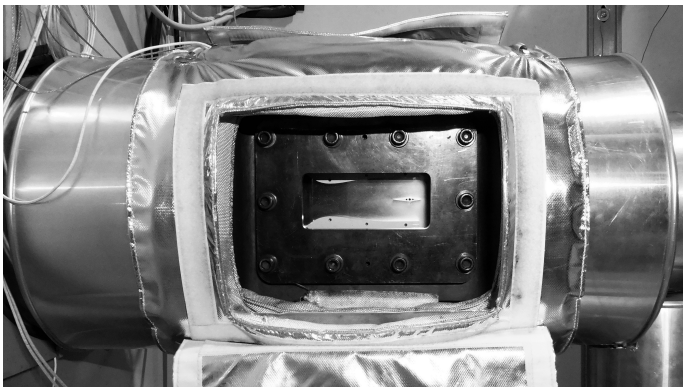

(a)

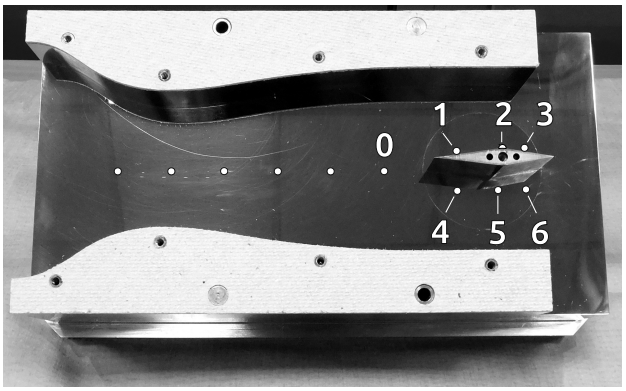

(b)

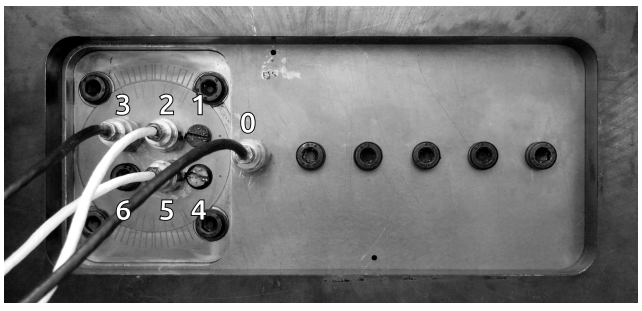

(c)

Figure 5.1: (a) Test section. Flow direction is from left to right. (b) Mirror-polished back-closure of the test section with converging-diverging nozzle and diamond-shaped airfoil. Static pressure taps are highlighted: 0 to 6. (c) Back closure of the test section and view of the pressure transducers as mounted.

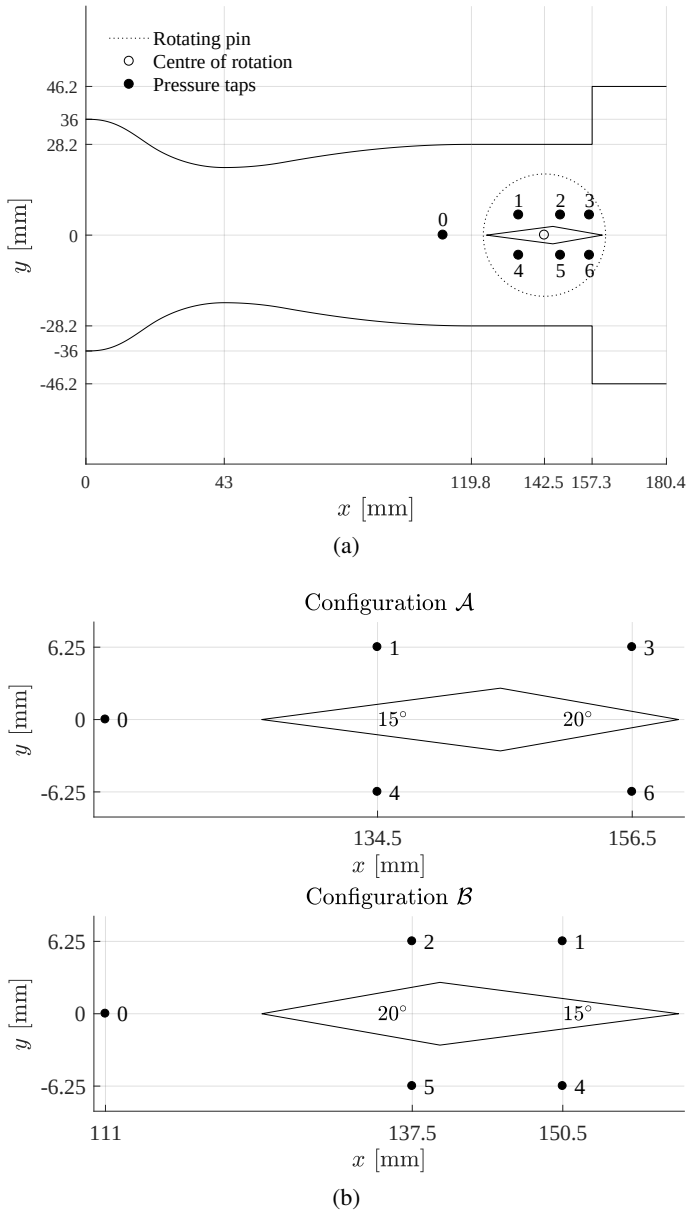

Figure 5.2: (a) Geometry of the test section in dimensional units. (b) Geometry of the diamond airfoil and position of the static pressure taps in configurations $\mathcal{A}$ and $\mathcal{B}$.

Similarly to the experiments on non-ideal nozzle expansions, a J-type thermocouple placed at the symmetry axis of the settling chamber measures the total temperature. At the same axial location of the thermocouple, total pressure is measured from a static pressure tap at the wall of the settling chamber. Schlieren visualizations of the flow within the test section are performed using the same set-up described in paragraph 2.1.2, to complement pressure and temperature measurements. The parameters of the high-speed CMOS camera used to record the schlieren images are slightly changed with respect to experiments presented in chaper 2: the frame rate is set to 25 fps, the exposure time to 1 ms and the image resolution to 1936 x 1216 pixels, which gives 12.7 px/mm.

The geometry of the test section is reported in Fig. 5.2a in dimensional units. A planar converging-diverging nozzle discharges a uniform supersonic stream towards a diamond-shaped

airfoil. As it is well known, the present flow arrangement produces two oblique shocks at the airfoil leading-edge and centered expansions at the shoulder. Measurements are taken to characterize the flow around the airfoil.

In design conditions, the wind-tunnel de Laval nozzle performs an expansion from total conditions $P^t = 10$ bar and $T^t = 277$ °C to pressure $P_e = 3.21$ bar and exhaust Mach number $M_e = 1.5$. The profile of the diverging portion of the nozzle is designed by applying the method of characteristics presented in paragraph 2.3. At the throat, located at 43 mm from inlet, the profiles of the converging and diverging portions match with horizontal tangent and continuous curvature. The converging portion is a 5^{th}-order polynomial curve, matched smoothly with a circular arc of radius 42 mm at the throat, i.e. twice the throat half-height (21 mm).

The nozzle discharges the flow into a 37.5 mm-long constant-area duct, where the airfoil is placed. The duct ends at 157.3 mm from inlet and eventually discharges into the downstream ambient. The airfoil, of chord $c = 36$ mm, is cantilever mounted on a rotating pin, whose attidude with respect to the horizontal axis of the test section can be adjusted manually with a resolution of 1°. A detail view of the airfoil is reported in Fig. 5.2b. In configuration $\mathcal{A}$, the semi-apertures at the leading and trailing edge are 7.5° and 10°, respectively. In configuration $\mathcal{B}$, the semi-aperture at the leading edge is 10° and at the trailing edge is 7.5°. The position of the rotating pin is sketched in Fig. 5.2a. A 180° rotation of the pin allows to switch from configuration $\mathcal{A}$ to configuration $\mathcal{B}$.

Pressure measurement points are marked with black dots in Fig. 5.2a. The static pressure in the flow upstream of the airfoil is measured on the nozzle axis, at the pressure tap identified as 0. Pressure taps 1 to 6 are machined in the rotating pin, and rotate with the airfoil at changing attitude. In each of the two possible configurations, $\mathcal{A}$ and $\mathcal{B}$, four out of six pressure taps around the airfoil are active. The active pressure taps for each configuration are reported in Fig. 5.2b. Pressure is measured at taps labelled as 1, 4, 3, 6 in configuration $\mathcal{A}$, and at taps 2, 5, 1, 4 in configuration $\mathcal{B}$.

5.2 Operating conditions and data representation

As commented in chapter 2, the batch operating mode of the TROVA is such that, at each time instant during a test run, a different dataset including total temperature, total and static pressures and schlieren images is acquired. Consistently with the nomenclature introduced in chapter 2, datasets are labelled as run i-j, where i identifies the test run and j the flow conditions attained at different time instants during the test.

At the design point, the wind-tunnel nozzle discharges a uniform supersonic flow at $M = 1.5$, whose thermodynamic state is defined by $P = 3.21$ bar, $T = 258$ °C. In terms of reduced variables, the thermodynamic state upstream of the airfoil is $P_r = P/P_c = 0.223$ and $T_r = T/T_c = 0.939$, where P_c and T_c are the critical pressure and temperature of MDM. The corresponding compressibility factor $Z = Pv/RT$ is 0.892.

A schematic representation of the flow pattern around the airfoil is given in Fig. 5.3. At the leading edge of the airfoil, the supersonic flow discharged by the nozzle is compressed and deflected by two oblique shock waves. At the shoulder, the flow is expanded by two centred expansion fans. At the trailing edge, the flow is again compressed and deflected by two oblique shocks. In each test, the active pressure taps are placed in the five uniform flow regions identified as A, B, B′, D, and D′ in Fig. 5.3. Specifically, pre-shock pressure P_A is measured at tap 0, post-shock pressures P_B and $P_{B'}$ are measured at taps 1 and 4 in configuration $\mathcal{A}$ (5 and 2 in configuration $\mathcal{B}$), and post-expansion pressures P_D and $P_{D'}$ are measured at taps 3 and 6 in configuration $\mathcal{A}$ (4 and 1 in configuration $\mathcal{B}$).

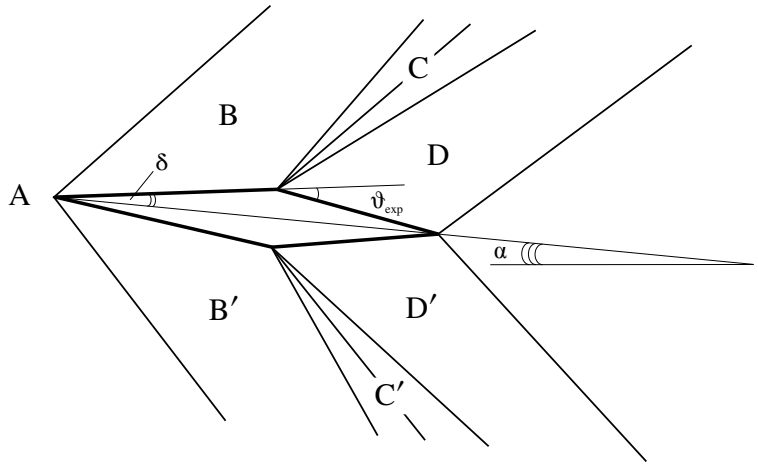

Figure 5.3: Wave pattern for a uniform supersonic flow around a diamond-shaped airfoil

Throughout the chapter, measurements are compared to the shock-expansion theory (see Thompson (1988) for reference), complemented with the SW EoS including the updated parameters by Thol *et al.* (2017). From the total pressure and temperature (P^t, T^t) measured in the settling chamber, the total enthalpy h^t and the entropy s are calculated using the SW model: $h^t = h(P^t, T^t)$ and $s = s(P^t, T^t)$. The total enthalpy and the entropy are constant along the expansion in the nozzle ($h^t = \bar{h}^t$ and $s = \bar{s}$). The thermodynamic state of the flow in region A is fully determined by the measured pressure P_A and by the calculated value of the entropy $\bar{s}$. The flow velocity in region A is determined by enforcing the energy conservation law of the quasi-one-dimensional model for steady isentropic nozzle flows (see paragraph 1.2.2), giving $u_A = \sqrt{2[\bar{h}^t - h(P_A, \bar{s})]}$. The thermodynamic state and the flow velocity in region A, together with the flow deviation angle $\vartheta = \delta - \alpha$ imposed by the compression ramp on the top (bottom) surface of the airfoil, define the pre-shock state $(P_A, v_A, \mathbf{u}_A, \vartheta)$. Once the pre-shock state and a suitable EoS for MDM providing $h = h(P, v)$ are set, the post-shock state $(P_B, v_B, \mathbf{u}_B, \beta)$, where β indicates the wave angle, is obtained from the Rankine-Hugoniot relations (see paragraph 1.2.3). From the set of variables $(P_B, s_B, \mathbf{u}_B, \bar{h}^t, \vartheta_{\text{exp}})$, where ϑ_{exp} is the deviation imposed by the expansion ramp, the post-expansion state $(P_D, v_D, \mathbf{u}_D)$ is calculated by resorting to the expression of Prandtl-Meyer expansions for general fluids reported in paragraph 1.2.3.

Figure 5.4 reports the saturation dome of MDM and selected isolines of the compressibility factor Z in the T-s diagram. On the diagram, the pre- and post-shock states obtained from a test in configuration $\mathcal{A}$, at attitude $\alpha = 0°$ are reported. The pre- and post-shock states reported on the diagram are attained at different time instants during the test and are characterized by an increasing value of the compressibility factor.

5.3 Results and discussion

In the present paragraph, measured data are presented and compared to results from the shock-expansion theory. For each test, four datasets including P_A^t, T_A^t, P_A, P_B, P_D and the corresponding schlieren images are provided. Each dataset describes a steady-state flow arrangement obtained at increasing value of the pre-shock compressibility factor, for which pre-shock, post-shock and post-expansion states can be determined following the procedure described in the previous paragraph. For the i-th test run, the four datasets are identified by the calculated value of the pre-shock

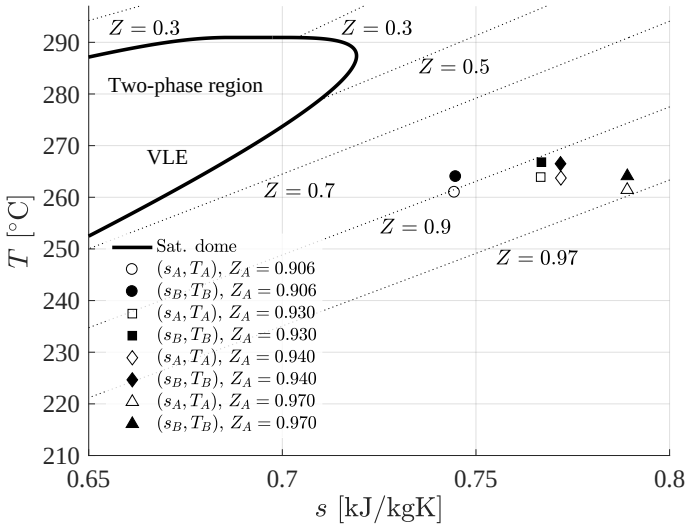

Figure 5.4: Saturation dome of MDM and measured pre-shock (subscript $(\cdot)_A$) and post-shock states (subscript $(\cdot)_B$)

compressibility factor Z_A and are labelled progressively as run i-1, run i-2, run i-3, run i-4.

Tests are run in configuration $\mathcal{A}$ at attitudes $\alpha = 0°,\ 1°$, and in configuration $\mathcal{B}$ at attitudes $\alpha = 0°,\ 1°,\ 2°$, giving the following set of deviation angles for the compression ramps: $\vartheta = 6.5°$, 7.5°, 8°, 8.5°, 9°, 10°, 11°, 12°. Expansion fans always realize flow turning by an angle $\vartheta_{\text{exp}} = 17.5°$.

Schlieren visualizations revealed the occurrence of three different flow patterns at varying attitude and configuration of the airfoil. Figure 5.5 reports schlieren visualizations of the flow-field in configuration $\mathcal{A}$, $\alpha = 0°$ (Fig. 5.5a), in configuration $\mathcal{B}$, $\alpha = 0°$ (Fig. 5.5b), and in configuration $\mathcal{B}$, $\alpha = 1°$. The three frames are associated to pre-shock compressibility factors of $Z_A = 0.906$, $Z_A = 0.930$, and $Z_A = 0.925$, respectively. In Fig. 5.5a and Fig. 5.5b, the flow pattern closely resembles the one expected from the inviscid shock-expansion theory: two oblique shocks form at the airfoil leading-edge and two centred expansion fans form at the shoulder. The flow deviation angles imposed by the compression ramps are $\vartheta = 7.5°$ and $\vartheta = 10°$, respectively. In Fig. 5.5c, the wave pattern on the bottom surface of the airfoil is qualitatively different from the expected one, possibly due to blockage effects or to flow conditions exceeding the maximum deviation angle. In the configuration depicted in Fig. 5.5c, the flow deviation angles imposed by the compression ramps are $\vartheta = 9°$ on the top surface and $\vartheta = 11°$ on the bottom surface of the airfoil. In all the tested configurations, compression ramps deflecting the flow through angles less than or equal to 10° originate oblique leading-edge shocks closely matching the ones expected from the shock-expansion theory. For flow deviation angles $\vartheta > 10°$, the flow layout is qualitatively similar to the one observed on the bottom surface of the airfoil in Fig. 5.5c.

The flow visualizations of Fig. 5.5a, Fig. 5.5b and the top portion of Fig. 5.5c reveal two distinct flow patterns at the boundaries of the constant-area duct, where the two leading-edge shocks interact with the wall boundary layer. For the test in configuration $\mathcal{A}$ (Fig. 5.5a), interaction of the leading-edge shocks with the upper and lower walls of the test section is of the normal type and results in two reflected shocks, which eventually intersect downstream of the airfoil. For the tests in configuration $\mathcal{B}$ (Fig. 5.5b and Fig. 5.5c) instead, flow visualizations reveal that the reflected shocks cross the uniform flow region downstream of the centred expansion fans, right upstream of the pressure taps where post-expansion pressures P_D and $P_{D'}$ are measured (taps 4 and 1). Therefore, pressure readings downstream of the expansion fans are strongly affected

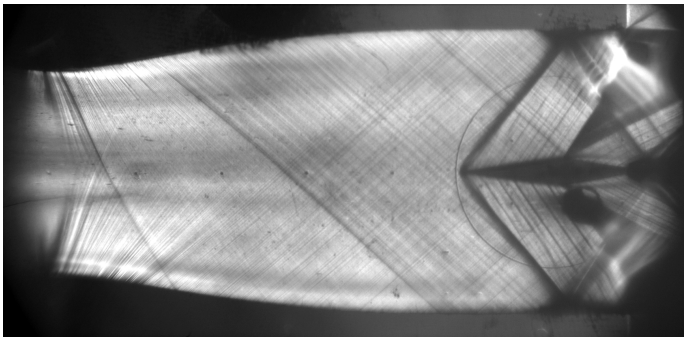

(a)

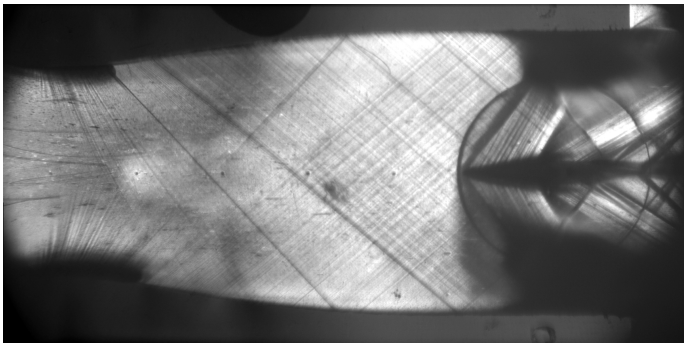

(b)

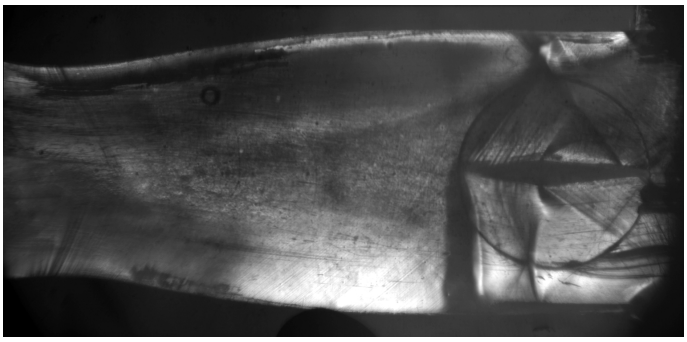

(c)

Figure 5.5: Schlieren visualizations. (a) Configuration $\mathcal{A}$, $\alpha = 0°$, $Z_A = 0.906$, (b) Configuration $\mathcal{B}$, $\alpha = 0°$, $Z_A = 0.930$, (c) Configuration $\mathcal{B}$, $\alpha = 1°$, $Z_A = 0.925$

ϑ	$P_A^t \pm U_{P_A^t}$	$T_A^t \pm U_{T_A^t}$	$P_A \pm U_{P_A}$	$P_B \pm U_{P_B}$	Z_A	run
6.5	6.4247 ± 0.0091	255.5 ± 1.2	2.0566 ± 0.0030	2.5359 ± 0.0036	0.924	1-1
6.5	5.9847 ± 0.0091	255.6 ± 1.2	1.8995 ± 0.0030	2.3347 ± 0.0036	0.930	1-2
6.5	4.9525 ± 0.0091	254.8 ± 1.2	1.5505 ± 0.0030	1.9011 ± 0.0036	0.944	1-3
6.5	2.8405 ± 0.0091	250.5 ± 1.2	0.8679 ± 0.0030	1.0819 ± 0.0036	0.969	1-4
7.5	8.7076 ± 0.0091	277.6 ± 1.2	2.8799 ± 0.0032	3.5271 ± 0.0034	0.906	2-1
7.5	7.0109 ± 0.0091	279.1 ± 1.2	2.2326 ± 0.0032	2.8170 ± 0.0034	0.930	2-2
7.5	6.1849 ± 0.0091	278.4 ± 1.2	1.9380 ± 0.0032	2.4361 ± 0.0034	0.940	2-3
7.5	3.3633 ± 0.0091	274.6 ± 1.2	1.0085 ± 0.0032	1.2998 ± 0.0034	0.970	2-4
8	6.0510 ± 0.0092	256.9 ± 1.2	1.9160 ± 0.0030	2.4930 ± 0.0036	0.930	3-1
8	5.5659 ± 0.0092	259.6 ± 1.2	1.7378 ± 0.0030	2.2830 ± 0.0035	0.938	3-2
8	4.6788 ± 0.0092	259.1 ± 1.2	1.4367 ± 0.0030	1.9064 ± 0.0036	0.949	3-3
8	2.8452 ± 0.0091	250.6 ± 1.2	0.8493 ± 0.0030	1.1499 ± 0.0036	0.969	3-4
8.5	6.4247 ± 0.0091	255.5 ± 1.2	2.0566 ± 0.0030	2.6384 ± 0.0034	0.924	4-1
8.5	5.9847 ± 0.0091	255.6 ± 1.2	1.8994 ± 0.0030	2.4473 ± 0.0034	0.930	4-2
8.5	4.9525 ± 0.0091	254.8 ± 1.2	1.5505 ± 0.0030	2.0025 ± 0.0034	0.944	4-3
8.5	2.8405 ± 0.0091	250.5 ± 1.2	0.8679 ± 0.0030	1.1256 ± 0.0034	0.969	4-4
9	6.3010 ± 0.0091	253.4 ± 1.2	1.9993 ± 0.0030	2.7184 ± 0.0036	0.925	5-1
9	5.9354 ± 0.0092	254.4 ± 1.2	1.8834 ± 0.0030	2.5296 ± 0.0036	0.930	5-2
9	4.8687 ± 0.0092	254.3 ± 1.2	1.5088 ± 0.0030	2.0643 ± 0.0036	0.945	5-3
9	2.8289 ± 0.0092	249.8 ± 1.2	0.8537 ± 0.0030	1.1701 ± 0.0036	0.969	5-4
10	6.4802 ± 0.0092	259.3 ± 1.2	2.0699 ± 0.0030	2.9230 ± 0.0035	0.926	6-1
10	6.1910 ± 0.0092	261.4 ± 1.2	1.9787 ± 0.0030	2.7415 ± 0.0035	0.930	6-2
10	4.6625 ± 0.0092	261.1 ± 1.2	1.4471 ± 0.0030	2.0199 ± 0.0035	0.950	6-3
10	3.0088 ± 0.0092	258.2 ± 1.2	0.9120 ± 0.0030	1.2948 ± 0.0035	0.969	6-4

Table 5.1: Pre- and post-shock states from experiments. Pressures are expressed in bar, temperatures in °C, and angles in degrees. The values of Z_A are computed using the SW EoS from the measured values of P_A^t, T_A^t and P_A and assuming that both the entropy and total enthalpy are constant from the reservoir to the pressure tap upstream of the airfoil

by the presence of the reflected shocks and cannot be compared to Prandtl-Meyer predictions of a single rarefaction fan. Figure 5.5c shows that the interaction of the leading-edge shock with the boundary layer on the upper wall of the test section originates a lambda-type shock, which eventually hits the top surface of the airfoil on the expansion ramp. In Fig. 5.5b, the interaction of the leading edge shocks with the upper and lower walls of the test section is not clearly visible. However, the presence of the two reflected shocks in the uniform flow region downstream of the centred expansion fans may suggest the occurrence of lambda-type shocks on the upper and lower walls similar to the one observed in the top portion of Fig. 5.5c. Except for the test in configuration $\mathcal{A}$, $\alpha = 0°$, which corresponds to the schlieren frame of Fig. 5.5a, the reflected shock waves are located upstream of the pressure taps where post-expansion pressures are measured.

Experimental results for shock waves deflecting the flow through angles $\vartheta < 10°$ are summarized in Tab. 5.1. For each deviation angle, the table reports the pre- and post-shock states measured in four different flow conditions. Data of Tab. 5.1 are represented graphically in Fig. 5.6, which gives the pressure ratio across the shock P_B/P_A as function of the flow deviation angle ϑ.

$P_B \pm U_{P_B}$	$P_D \pm U_{P_D}$	run
3.5271 ± 0.0034	2.2101 ± 0.0038	2-1
2.8170 ± 0.0034	1.6569 ± 0.0038	2-2
2.4361 ± 0.0034	1.4978 ± 0.0038	2-3
1.2998 ± 0.0034	0.7541 ± 0.0038	2-4

Table 5.2: Post-expansion states for run 2, in flow conditions 2-1, 2-2, 2-3, 2-4. Deviation angle is $\vartheta_{\text{exp}} = 17.5°$. Pressures are expressed in bar, temperatures in °C, and angles in degrees.

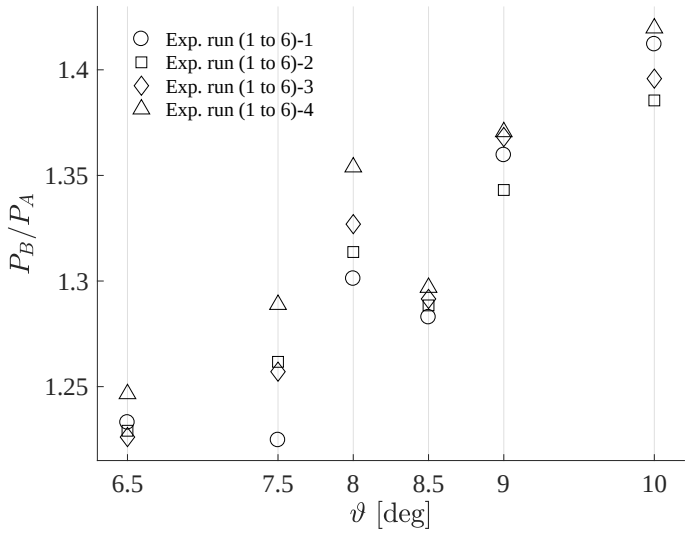

Figure 5.6: Pressure ratio P_B/P_A as function of the deviation angle ϑ. Flow conditions are given in Tab. 5.1

$M_A \pm U_{M_A}$	$M_B \pm U_{M_B}$	$M_B \pm U_{M_B}$	run
1.544048 ± 0.040974	1.396502 ± 0.027448	1.600781 ± 0.070594	2-1
1.600781 ± 0.040372	1.362002 ± 0.028970	1.666667 ± 0.065893	2-2
1.526879 ± 0.031863	1.308265 ± 0.016118	-	6-2

Table 5.3: Mach number measurements in flow conditions 2-1, 2-2, and 6-2 of Tab. 5.1

As commented beforehand, the presence of reflected shock waves upstream of the post-expansion pressure taps affected the measurement of the post-expansion pressure in most of the tests. Unbiased measurements of the post-expansion pressure are available only for the test in configuration $\mathcal{A}$, $\alpha = 0°$. Table 5.2 gives the post-expansion states measured during run 2, in flow conditions 2-1, 2-2, 2-3, 2-4. Across the expansion fan, the flow is deviated by an angle $\vartheta_{\text{exp}} = 17.5°$.

Results of Tab. 5.1 and Tab. 5.2 are compared to the shock-expansion theory and summarized in the two scatter plots of Fig. 5.7 and Fig. 5.8. In the two plots, the measured pressure ratios P_B/P_A (Fig. 5.7) and P_D/P_B (Fig. 5.8) are compared to the ones resulting from the solution to the Rankine-Hugoniot jump relations and from the integration of the Prandtl-Meyer function across the expansion fan. The spread of theoretical predictions with respect to the measured values is within ±5% for the shock waves and ±10% for the expansion fans. Uncertainty bars are not reported to improve legibility of the plots, since uncertainty bars are smaller than the data labels.

Schlieren visualizations of the tested configurations (cf. Fig. 5.5) clearly display the Mach

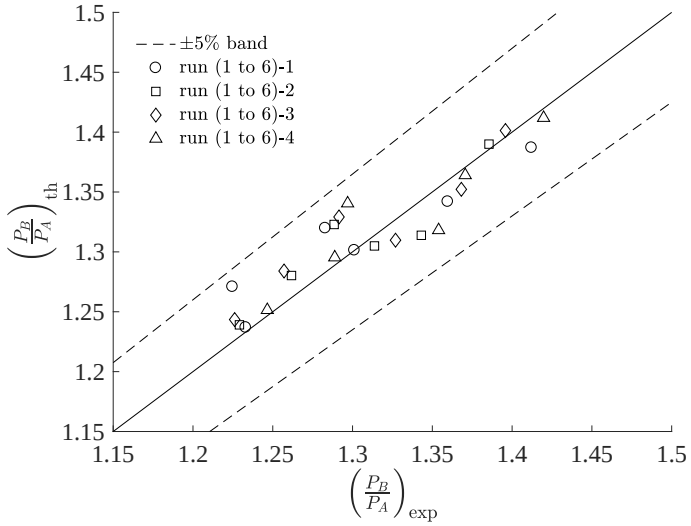

Figure 5.7: Scatter plot for test results on oblique shock waves. The measured pressure ratio P_B/P_A is compared to the one resulting from the Rankine-Hugoniot jump relations. Flow conditions are given in Tab. 5.1

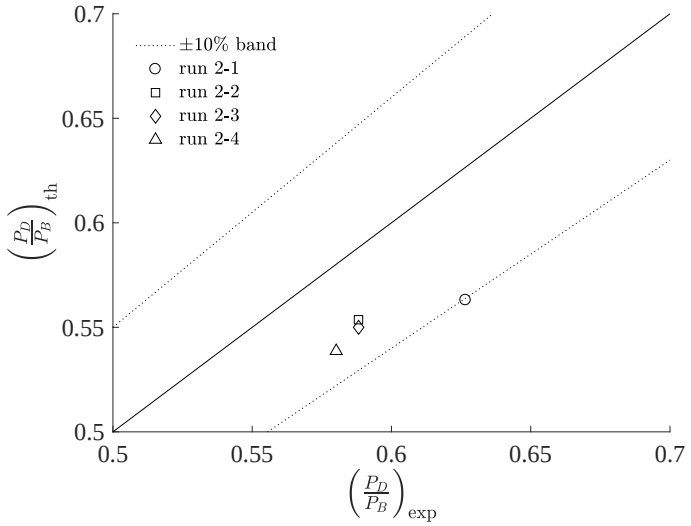

Figure 5.8: Scatter plot for test results on expansion fans. The measured pressure ratio P_D/P_B is compared to the one resulting from the theoretical solution of the Prandtl-Meyer expansion. Flow conditions are given in Tab. 5.2

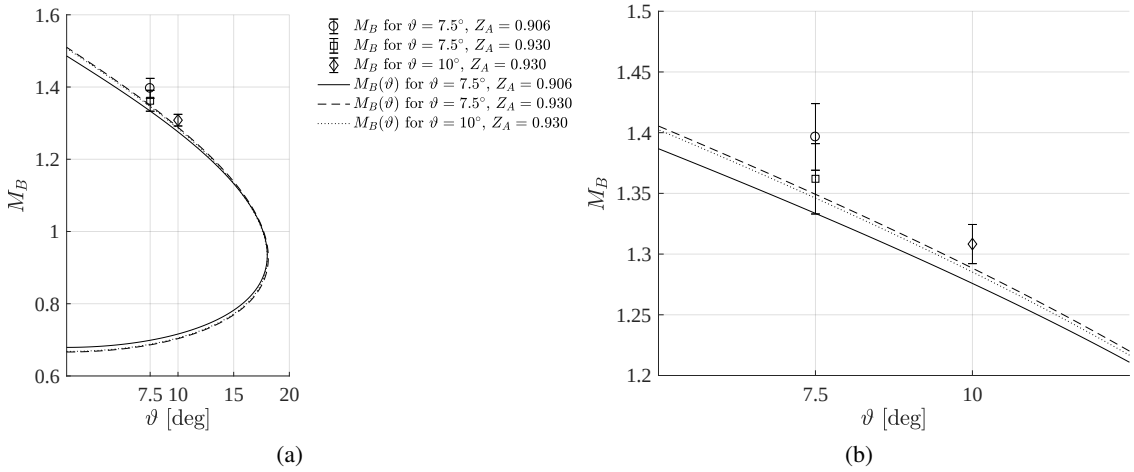

(a) (b)

Figure 5.9: Mach number–deviation polar (from theory) and measured post-shock Mach numbers

waves in the diverging portion of the nozzle and around the airfoil. The slope of the Mach waves with respect to the local flow direction provides a direct measurement of the local Mach number, as described in paragraph 2.1.2. The quality of the schlieren images acquired in flow conditions 2-1, 2-2, and 6-2 of Tab. 5.1 is good enough to allow the detection of Mach waves in the diverging portion of the nozzle and in the flow around the airfoil. The Mach number in the pre-and post-shock states M_A and M_B measured from the schlieren images of Fig. 5.5a and Fig. 5.5 (run 2-1 and run 6-2), and from the schlieren visualization of the test in configuration $\mathcal{A}$, $\alpha = 0°$, $Z_A = 0.930$ (run 2-2) are reported in Tab. 5.3. For runs 2-1 and 2-2, also the post-expansion Mach number M_D is provided, which corresponds to the post-expansion state reported in Tab. 5.2. In Fig. 5.9, the Mach number measured in the post-shock state M_B is superimposed to the corresponding Mach number–deviation $M_B(\vartheta)$ polar. The reported polar curves are those corresponding to the pre-shock states attained in the three mentioned test runs. The measured M_B are compared here with the calculated polar curves, showing that the measured post-shock states lie on the weak-shock branch of the Rankine-Hugoniot curve.

5.3.1 Non-ideal compressible-fluid effects

In a perfect gas, the properties of oblique shock waves depend uniquely on the upstream Mach number M_A and on the value of the specific heat ratio γ, which is constant for a given fluid regardless of its thermodynamic state. As opposite, flows with shock waves described by non-ideal EoS show a more or less noticeable dependence of the post-shock state on the upstream thermodynamic state. In all the tests examined here, not only the upstream thermodynamic state in each test condition is different, but also the pre-shock Mach number M_A, due to the non-ideal nature of the expansion occurring in the nozzle, as discussed in chapter 2. Specifically, the nozzle exhaust Mach number increases as test proceeds, or, in other words, as total conditions in the settling chamber move towards dilute, ideal conditions. To provide evidence of the increase of the nozzle exhaust Mach number at increasing value of the compressibility factor Z_A, the Mach number measured in the diverging portion of the nozzle in conditions 2-1 and 2-2 (see Tab. 5.1) is reported in Fig. 5.10. In flow condition 2-2, less measurement points are available with respect to flow condition 2-1, since the Mach waves become less visible as flow conditions approach the dilute-gas region.

None of the flow variables describing pre-shock and pre-expansion states remains constant

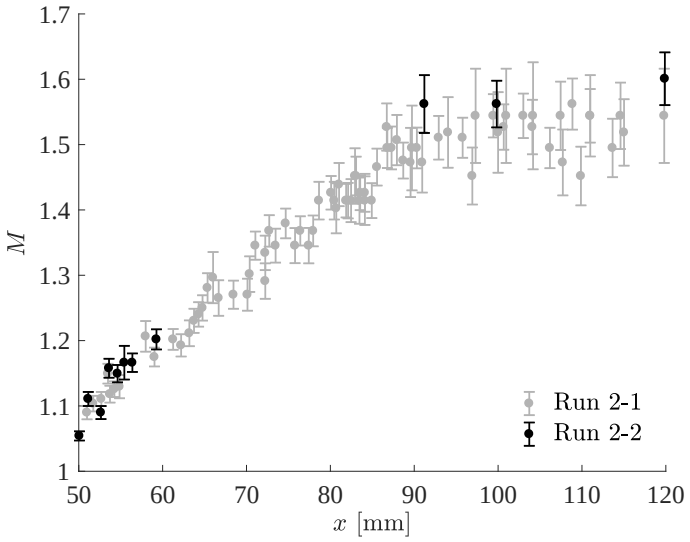

Figure 5.10: Mach number distribution along the diverging portion of the nozzle, for flow conditions 2-1 ($Z_A = 0.906$) and 2-2 ($Z_A = 0.930$) (see Tab. 5.1)

Shock wave

		Experiment	SW EoS	PIG EoS
P_B/P_A	run 2-1	1.2247 ± 0.0018	1.2709 ± 0.0062	1.3069 ± 0.0072
	run 2-4	1.2889 ± 0.0052	1.2954 ± 0.0084	1.3067 ± 0.0090
M_B/M_A	run 2-1	0.9044 ± 0.0299	0.8980 ± 0.0024	0.8680 ± 0.0030
	run 2-4	-	0.8884 ± 0.0033	0.8795 ± 0.0036
u_B/u_A	run 2-1	-	0.8748 ± 0.0040	0.8701 ± 0.0033
	run 2-4	-	0.8828 ± 0.0038	0.8815 ± 0.0038
c_B/c_A	run 2-1	-	0.9742 ± 0.0033	1.0023 ± 0.0015
	run 2-4	-	0.9937 ± 0.0020	1.0023 ± 0.0016

Expansion fan

		Experiment	SW EoS	PIG EoS
P_D/P_B	run 2-1	0.6266 ± 0.0012	0.5612 ± 0.0029	0.5315 ± 0.0029
	run 2-4	0.5801 ± 0.0033	0.5381 ± 0.0032	0.5288 ± 0.0032
M_D/M_B	run 2-1	1.1463 ± 0.0553	1.2523 ± 0.0151	1.3289 ± 0.0045
	run 2-4	-	1.2768 ± 0.0126	1.3005 ± 0.0048
u_D/u_B	run 2-1	-	1.3183 ± 0.0161	1.3212 ± 0.0047
	run 2-4	-	1.2923 ± 0.0128	1.2930 ± 0.0049
c_D/c_B	run 2-1	-	1.0527 ± 0.0028	0.9942 ± 0.0011
	run 2-4	-	1.0122 ± 0.0015	0.9942 ± 0.0011

Table 5.4: Ratios of downstream to upstream flow conditions for shock wave and expansion fan observed in run 2, conditions 2-1 and 2-4

during a test run. If the variation of the specific heat ratio γ among two different test conditions, e.g. run 2-1 and 2-4 is considered, the pre-shock state and the ratios P_B/P_A and P_D/P_B do not remain constant during a test even if the flow is modelled under the PIG assumption. In the present paragraph, the non-ideal nature of the oblique shock waves and expansion fans originating on the airfoil in two independent flow conditions is investigated by examining the ratios of downstream (post-shock and post-expansion) to upstream (pre-shock and pre-expansion) flow variables. In Tab. 5.4, the ratios of the post-shock (subscript $(\cdot)_B$) and post-expansion (subscript $(\cdot)_D$) states to pre-shock (subscript $(\cdot)_D$) and pre-expansion (subscript $(\cdot)_B$) states observed in conditions 2-1 and 2-4 (see Tab. 5.1) are reported. Flow deviation angles are $\vartheta = 7.5°$ for the shock wave and $\vartheta_{\text{exp}} = 17.5°$ for the expansion fan. The pre-shock state is calculated using the steady one-dimensional isentropic flow model. The non-ideal case is studied using the SW EoS of Thol *et al.* (2017). The pre-shock state is computed from the measured pressure $P_A = 2.8799$ bar, to give $M_A = 1.4855$, $u_A = 186.43$ m/s, $c_A = 125.50$ m/s for run 2-1 and from $P_A = 1.008$ bar (measured value), $M_A = 1.5478$, $u_A = 207.60$ m/s, $c_A = 134.13$ m/s for run 2-4. In the ideal-gas case, the specific heat ratios γ of the PIG EoS are 1.01757 for run 2-1 and 1.01762 for run 2-4, as obtained at the corresponding measured pressures P_A, in the dilute gas limit. The pre-shock Mach number, flow velocity and speed of sound are $M_A = 1.4817$, $u_A = 206.86$ m/s, $c_A = 139.61$ m/s for run 2-1 and $M_A = 1.5466$, $u_A = 215.27$ m/s, $c_A = 139.19$ m/s for run 2-4. Together with experimental data, Tab. 5.4 reports the ratios of downstream to upstream flow variables, calculated using the shock-expansion theory and both the PIG and the SW EoS. Uncertainties on the calculated flow variables are obtained by propagating the uncertainties on the measured P_A^t, T_A^t and P_A, and on the flow deviation angle ϑ in the solution of the Rankine-Hugoniot jump relations and in the integration of the Prandtl-Meyer function across the expansion fan. To this purpose, a standard Monte Carlo method is applied. The uncertainties on P_A^t, T_A^t, and P_A are considered Gaussian, $\pm 2\sigma$, while for the uncertainty on the flow deviation angle (due to the manual orientation of the airfoil) a uniform probability distribution is assumed, with extreme values $\pm 0.25°$.

As expected, measurements reveal that shock waves compress and slow the flow, while expansion fans expand and accelerate the flow. However, results obtained using the SW EoS show that the speed of sound decreases upon compression and increases upon expansion. This behaviour of the speed of sound, which is typical of the non-ideal classical regime, is qualitatively and quantitatively different from the one predicted by the PIG EoS.

5.4 Conclusions

Non-ideal oblique shock waves and expansion fans were characterized experimentally in the TROVA blow-down wind tunnel. The wind tunnel operated with the molecularly-complex organic compound MDM. Oblique waves occurring in a uniform supersonic flow at Mach number 1.5 were studied for a set of flow deviation angles through independent measurements of temperature, pressure and Mach number. If the envisaged oblique shock/fan configuration is attained in the regions where pressure taps are located, pressure and Mach number measurements agree with the inviscid shock-expansion theory, complemented with an equation of state accounting for non-ideal flow behaviour. Reference experimental data are provided for oblique shocks realizing flow turning by six angles in the range $\vartheta = 6.5°$-$10°$, for upstream thermodynamic states featuring compressibility factors in the range 0.91-0.97, and for a centered expansion around a sharp corner imposing a flow deviation of $\vartheta_{\text{exp}} = 17.5°$. The centered rarefaction fan was characterized for upstream Mach numbers in the range $M = 1.33$-1.38 and compressibility factors in the pre-expansion state in the range $Z = 0.879$-0.958.

The jump in selected flow variables across shock waves and expansion fans was analyzed by

means of experimental data and the shock-expansion theory. As expected, measurements showed that shock waves compress and slow the flow, while expansion fans expand and accelerate the flow. Though, the speed of sound calculated with the SW model in all the tested conditions was found to decrease across compressions and to increase upon expansions, contrarily to the one predicted by the PIG model, thus further confirming the non-ideal nature of the flow.

6

Oblique waves in the non-ideal compressible-fluid regime

Non-ideal supersonic flows over a diamond-shaped airfoil were observed experimentally in the TROVA wind tunnel. Results of experiments were discussed in detail in chapter 5. In the present chapter, wind-tunnel tests are reproduced numerically using the SU2 suite. The numerical method is first assessed against the experimental data presented in chapter 5 and then etensively applied to the analysis of the observed flow patterns. Numerical results include Euler and Navier-Stokes simulations, which are run using both state-of-the-art thermodynamic models and the PIG EoS.

Non-ideality of wind-tunnel flows and blockage effects are discussed. Non-ideality of the expansion in the wind-tunnel nozzle is seen to significantly influence the wave pattern originating on the airfoil. In addition to non-ideal effects, the wave pattern observed on the airfoil is heavily influenced by blockage effects, which play a significant role in determining the interaction of the shock waves generated within the test section with the wall boundary layer. The non-ideal nature of the wave pattern originating on the airfoil is studied by comparing numerical results obtained using the PIG and iPRSV EoS. In the non-ideal yet classical regime investigated here, shock waves compress and slow the flow, while expansion fans expand and accelerate the flow. However, EoS accounting for non-ideal flow behaviour yield a distribution of the speed of sound across shock waves and expansion fans which departs from its PIG counterparts both quantitatively and qualitatively. Namely, the speed of sound decreases across shock waves and increases across expansion fans in all the examined test conditions.

The structure of the chapter is the following. In paragraph 6.1, the flow within the TROVA test section is simulated numerically at varying geometrical configuration and operating conditions. The numerical method first assessed against experimental data (paragraph 6.1.1) and the effects of flow non-ideality and wall blockage are discussed (paragraphs 6.1.2 and 6.1.3). The non-ideal nature of the oblique wave pattern originating on the airfoil is discussed in paragraph 6.2 for one exemplary test condition. Final comments are given in paragraph 6.3.

6.1 Numerical simulation of wind-tunnel tests

Experiments described in chapter 5 are reproduced numerically to investigate the flow mechanisms involved in the experimental observation of supersonic flows with oblique waves in the NICF regime. Non-ideality of wind-tunnel flows is discussed by analyzing the operation of the wind-tunnel nozzle and the wave pattern originating on the diamond airfoil at varying operating conditions.

6.1.1 Assessment of the numerical method

The suitability of a set of numerical methods to the simulation of the flow-field within TROVA test section is discussed here for two reference test conditions chosen among the experimental results presented in chapter 5, namely those reported in Tab. 6.1[1]. The computational domain includes the wind-tunnel de Laval nozzle, the constant-area duct housing the diamond airfoil, and a portion of the downstream ambient. Dimensions of the flow domain are reported in Fig. 5.2a. CFD simulations use both the Euler and the full Reynolds-averaged compressible Navier-Stokes

[1] Throughout the present chapter, test conditions are labelled according to the nomenclature introduced in chapter 5.

	$P_A^t \pm U_{P_A^t}$	$T_A^t \pm U_{T_A^t}$	$P_A \pm U_{P_A}$	Γ_A	run ID
Conf. $\mathcal{A}$, $\alpha = 0°$	8.7076 ± 0.0091	277.6 ± 1.2	2.8799 ± 0.0032	0.920	2-1
Conf. $\mathcal{B}$, $\alpha = 0°$	6.1910 ± 0.0092	261.4 ± 1.2	1.9787 ± 0.0030	0.944	6-2

Table 6.1: Reference test conditions. Measured P_A^t and T_A^t, measured P_A, and Γ_A computed from thermodynamic model. Measurements are reported with the corresponding expanded uncertainties. Pressures are expressed in bar, temperatures in °C.

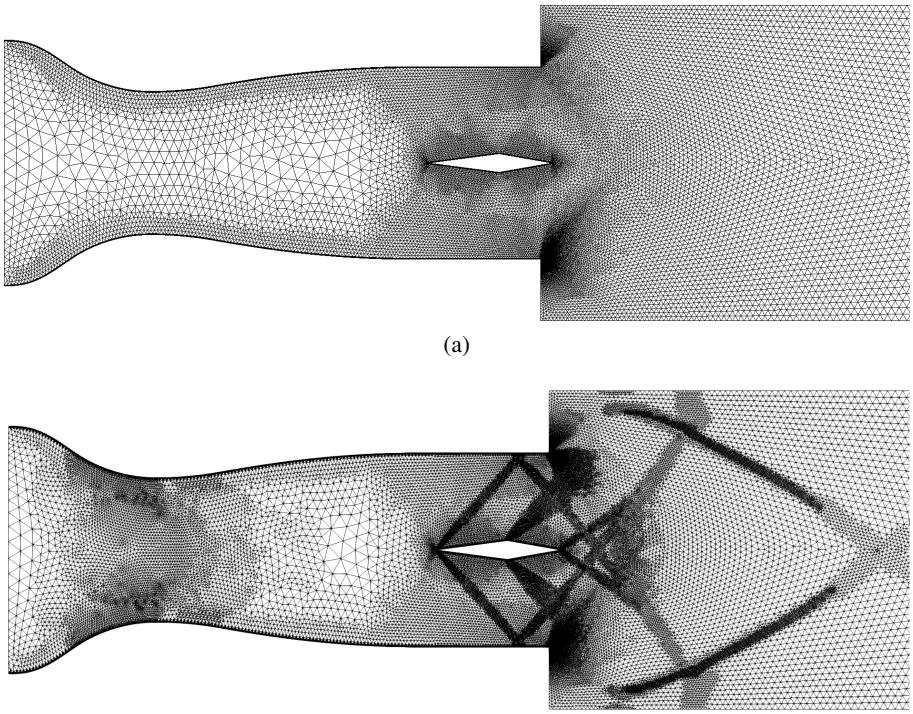

(a)

(b)

Figure 6.1: Computational grid. (a) Baseline (54k elements), (b) Adapted (236k elements)

equations, complemented with the iPRSV EoS and with the EoS by Thol *et al.* (2017). Navier-Stokes simulations adopt the Spalart-Allmaras turbulence model. Similarly to results reported for supersonic expansions in de Laval nozzles (cf. chapter 2), all numerical simulations reported here are two-dimensional. Indeed, the planar configuration of the wind-tunnel test section can be exploited to run two-dimensional simulations instead of three-dimensional ones, without sacrificing the accuracy of results in the inviscid core of the flow, where experimental data are available for comparison.

In Navier-Stokes (Euler) simulations, no-slip (slip) boundary conditions are set on the upper and lower nozzle profiles and on the airfoil boundary. On the vertical and horizontal walls delimiting the downstream ambient, slip boundary conditions are set both in Euler and Navier-Stokes simulations. At the inflow and outflow boundaries, characteristics-based boundary conditions are enforced (cf. paragraph 2.2). Total pressure and temperature are imposed at the nozzle inlet boundary, while a supersonic outlet flow is set at the domain outflow boundary. The supersonic outflow condition is enforced by assigning a uniform pressure distribution characterized by an arbitrarily low value on the outflow boundary. However, the assumption of a uniform outlet pressure is inconsistent with the presence of a finite-strength wave pattern around the airfoil (cf Fig. 5.5),

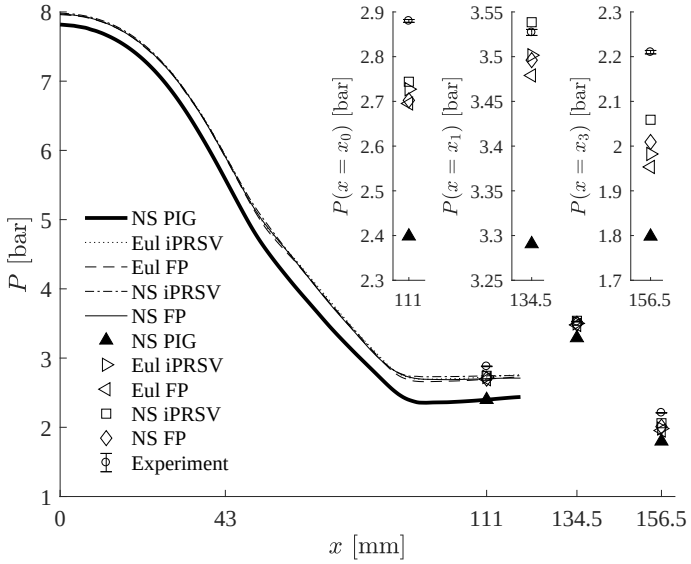

(a)

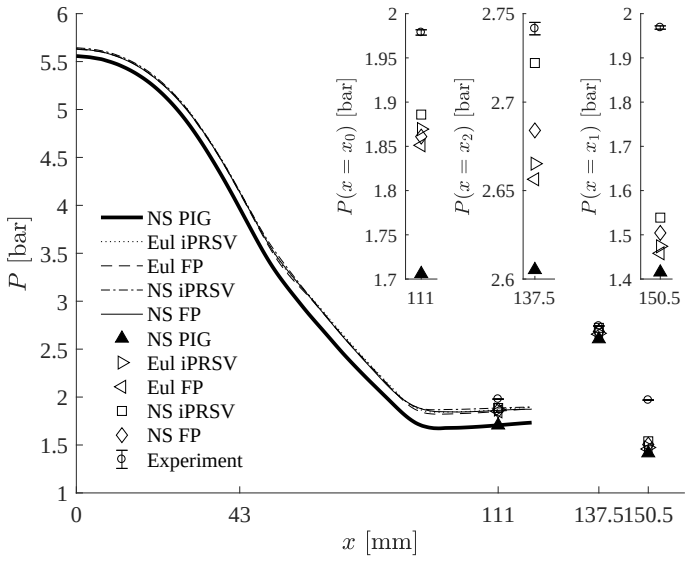

(b)

Figure 6.2: Pressure along the nozzle axis and in the post-shock and post-expansion states from numerical simulations and experiments. (a) Run 2-1, (b) Run 6-2. Test conditions are given in Tab. 6.1

which is reasonably expected to propagate downstream with multiple reflections at the wind tunnel walls. To overcome this inconsistency, the length of the computational domain is artificially extended up to five times the length of the test section (5×180.4 mm, cf. Fig. 5.2a) where the pressure can be assumed to be approximately constant. Moreover, thanks to the supersonic nature of the flow, no perturbances are expected to travel upstream towards the airfoil region of interest here. Starting from the baseline computational grid of Fig. 6.1a, the mesh adaptation procedure of Dussin *et al.* (2009) is applied to properly resolve shock waves and expansion fans. After three levels of adaptive refinement, the final grid of Fig. 6.1b is obtained. The baseline and the final, adapted grids are made of 54k and 236k elements, respectively.

Figures 6.2, 6.3 and 6.4 report experimental and numerical results obtained in the two refer-

ence test conditions of Tab. 6.1. In Fig. 6.2, pressures measured at the pre-shock, post-shock and post-expansion pressure taps (0, 1, 3 for run 2-1 and 0, 2, 1 for run 6-2) are compared to pressure profiles along the nozzle axis and to the local pressures obtained from numerical simulations at the same locations of the pressure taps. Numerical results are obtained from steady-state Euler (Eul) and Navier-Stokes (NS) simulations using different EoS, namely the PIG and iPRSV EoS, and the EoS by Thol *et al.* (2017), available from the FluidProp library (FP). The specific heat ratio γ for the PIG simulations is 1.018, as obtained in the temperature range of interest for the reference test conditions of Tab. 6.1.

Results of run 2-1 (Fig. 6.2a) are analysed first. The pressure profile obtained using the PIG EoS significantly departs from experimental measurements, while simulations run using the more complex iPRSV and FP EoS capture farily well the experimental data. Among simulations run using the same thermodynamic model, results from Navier-Stokes simulations are closer to the experimental ones. However, results of Fig. 6.2a clearly show that the computed pressure values are influenced more by the EoS than by viscous effects, at least in the so-called inviscid core of the flow, where pressure measurements are carried out. The same considerations apply to the results of run 6-2 (Fig. 6.2b). However, differently from run 2-1, the agreement between the measured and calculated post-expansion pressures is poor, even for simulations run with the iPRSV and FP EoS.

Figure 6.3 reports comparisons between schlieren images and computed flow-fields for run 2-1 and run 6-2. Specifically, pressure isolines from Navier-Stokes (white lines) and Euler (black lines) simulations are plotted over schlieren images. All simulations reported here are run using the iPRSV EoS. For each of the two runs, pressure isolines of the Navier-Stokes and Euler simulation cover the same pressure range and are given the same spacing, thus they refer to the same pressure levels. In the inviscid core of the flow, numerical simulations correctly capture the flow layout observed in the experiments. Euler simulations yield a leading-edge shock angle and an expansion pattern at the airfoil shoulder which closely match the ones resulting from Navier-Stokes simulations. Moreover, the flow-fields depicted in Fig. 6.3 confirm that, as expected, the pressure field is reasonably uniform in regions where static pressure taps are located. However, prominent viscous effects arise at the duct walls, where the leading-edge shocks interact with the wall boundary layer. Even though Navier-Stokes simulations are able to reproduce, at least qualitatively, the shock-boundary layer interaction, the simulated wave patterns downstream of the two shock reflections on the upper and lower walls depart significantly from the experimental ones. Shock/boundary-layer interaction is indeed a very complex, unsteady phenomenon and the current RANS approximation is not expected to capture it appropriately. Moreover, turbulence in the non-ideal regime is still a matter of debate, and the applicability of turbulence models for ideal turbulence in the non-ideal regime is questionable. For both runs 2-1 and 6-2, simulations predict the intersection of the two reflected shock waves at the symmetry axis, at a distance of about $1/3$ airfoil chord from the airfoil trailing-edge. Though schlieren images do not clearly show the interaction between the leading-edge shock waves and the wall boundary layer, reflected shocks can be observed in Fig. 6.3 downstream of the expansion fans. In run 2-1 (Fig. 6.3a), reflected shocks intersect immediately downstream of the airfoil, without overlapping pressure taps 3 and 6. Although numerical simulations only loosely describe the shock reflection mechanism, uniform flow regions downstream of the expansion fans are seen to occur both in the experiment and in the simulations. Within the uniform region on the top surface of the airfoil, the computed values of pressure at tap 3 agree well with the experimental measurement (cf. Fig. 6.2a). In run 6-2 (Fig. 6.3b), instead, reflected shocks hit the expansion ramps of the airfoil and give rise to a reflection pattern which totally deviates from the expected one. In this case, post-expansion pressures from numerical simulations do not match the experimental ones (cf. Fig. 6.2b), and the reason is twofold. First, measurement of the post-expansion pressure is strongly affected by the presence

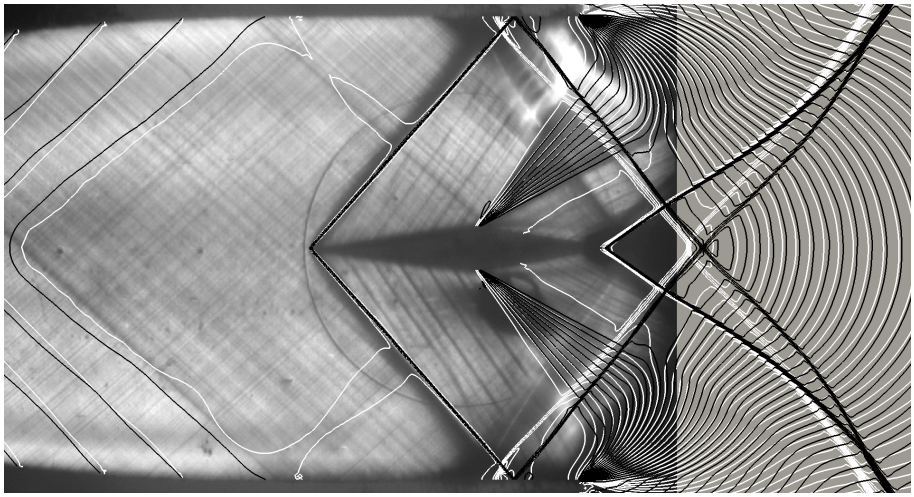

(a)

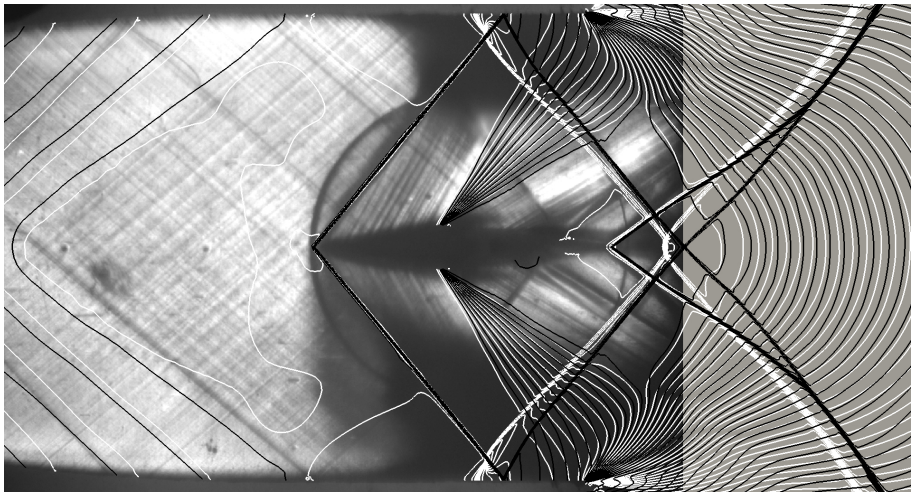

(b)

Figure 6.3: Schlieren visualization and pressure isolines from Euler iPRSV (black) and Navier-Stokes iPRSV (black) simulations. (a) Run 2-1, (b) Run 6-2. Test conditions are given in Tab. 6.1

of a shock wave (reflection of the leading-edge shock from the upper wall) upstream of tap 1. Second, simulations predict a qualitatively different flow layout downstream of shock reflection at the wall, and the computed values of pressure at tap 1 significantly depart from the measured one.

Numerical results for runs 2-1 and 6-2 are further assessed by comparing the computed flow Mach number to the available measurements, as shown in Fig. 6.4. The local flow Mach number is measured in the supersonic portion of the domain, where a fine pattern of Mach waves is visible from schlieren visualizations (Fig. 5.5) and the measurement procedure described in chapter 2 can be applied. Numerical results fall within experimental uncertainty bars in the whole domain.

For test conditions labelled as run 2-1 in Tab. 6.1, propagation of experimental uncertainties through the CFD code is studied, in order to compare numerical and experimental error bars. The same analysis presented in paragraph 2.4 for de Laval nozzles is now repeated for the flow domain and test conditions of interest here. Again, only the uncertainties on P^t and T^t are propagated in the CFD simulation, since, according to Cinnella *et al.* (2010), uncertainties on the thermodynamic model can be neglected with respect to other sources of uncertainty. Results are obtained from

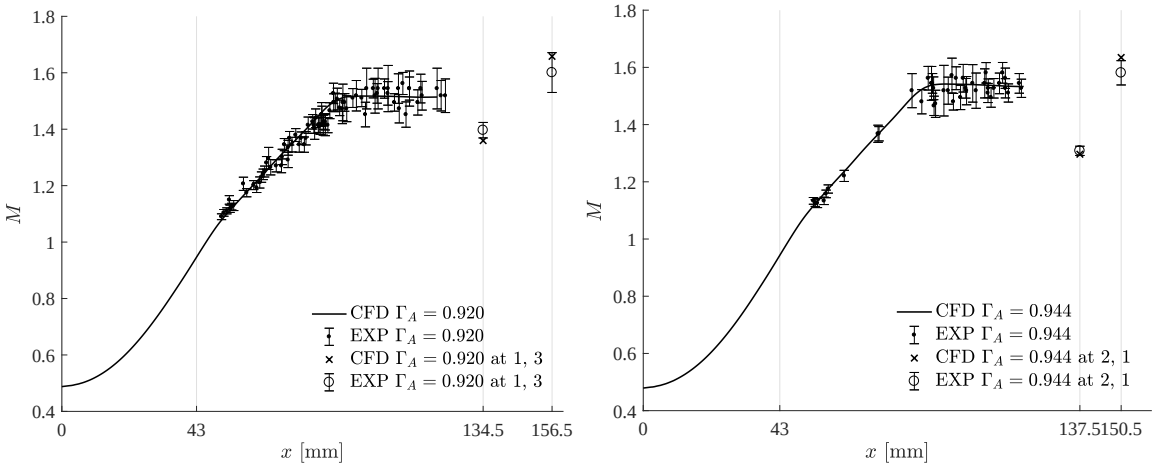

(a) (b)

Figure 6.4: Mach number along the nozzle axis and in the post-shock and post-expansion states from experiments and simulations. (a) Run 2-1, (b) Run 6-2. Test conditions are given in Tab. 6.1

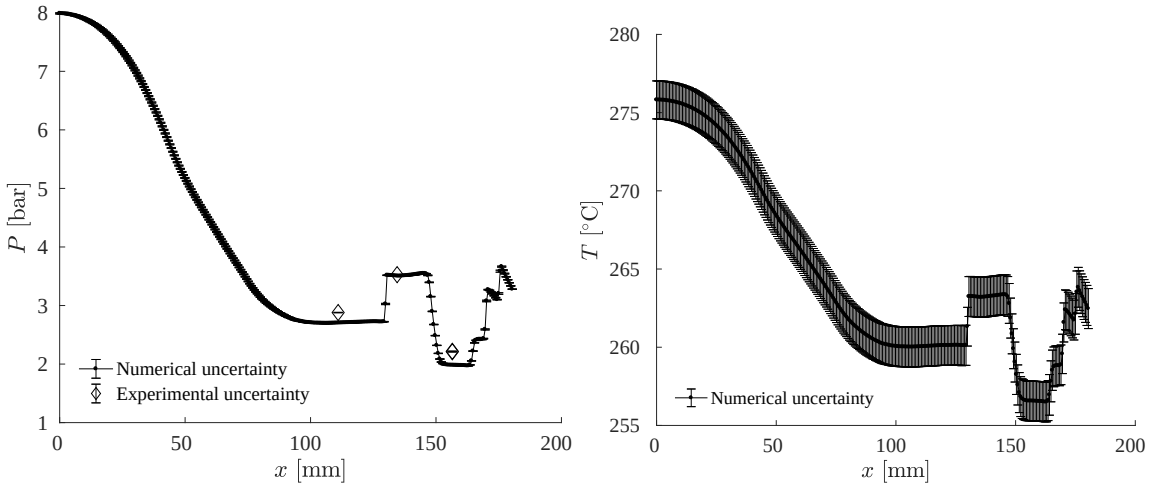

(a) (b)

Figure 6.5: Comparison of experimental and numerical error bars on the (a) pressure and (b) temperature profiles along a horizontal axis parallel to the nozzle symmetry axis, at a distance of 6.25 mm from centreline. Numerical error bars result from an UQ analysis performed in test conditions identified as run 2-1 in Tab. 6.1

$P_A^t \pm U_{P_A^t}$	$T_A^t \pm U_{T_A^t}$	$P_A \pm U_{P_A}$	Γ_A	run ID
8.7076 ± 0.0091	277.6 ± 1.2	2.8799 ± 0.0032	0.920	2-1
7.0109 ± 0.0091	279.1 ± 1.2	2.2326 ± 0.0032	0.944	2-2
6.1849 ± 0.0091	278.4 ± 1.2	1.9380 ± 0.0032	0.953	2-3
3.3633 ± 0.0091	274.6 ± 1.2	1.0085 ± 0.0032	0.981	2-4

Table 6.2: Test in configuration $\mathcal{A}$, $\alpha = 0°$. Measured P_A^t, T_A^t, measured P_A, and Γ_A from thermodynamic model. Pressures are expressed in bar, temperatures in °C.

Navier-Stokes simulations performed using the SW model, and are reported in Fig. 6.5 in terms of pressure (Fig. 6.5a) and temperature (Fig. 6.5b) profiles along a horizontal axis parallel to the nozzle symmetry axis, at a distance of 6.25 mm from centreline. Similarly to what observed for nozzle flows in chapter 2, SU2 is seen to provide a robust and predictive solution. Deviations from the nominal pressure and temperature profiles resulting from uncertainties on total pressure and temperature are below $< 0.01\%$ and $< 0.1\%$, respectively.

6.1.2 Non-ideal compressible-fluid effects in wind-tunnel flows

The operation of the wind-tunnel de Laval nozzle is examined first. The test in configuration $\mathcal{A}$ at neutral attitude is taken here as reference and the four flow conditions reported Tab. 6.2 are simulated numerically on the computational grid of Fig. 6.1. Figure 6.6 shows the profiles of the fundamental derivative of gasdynamics Γ, static to total pressure ratio P/P^t, Mach number M and local to reservoir speed of sound ratio $c/c(P^t, T^t)$ along the symmetry axis of the nozzle, from the inlet to the exhaust section. In all plots, Navier-Stokes simulations using the Spalart-Allmaras turbulence model are reported and comparison is drawn between numerical results obtained using the iPRSV and the PIG EoS. Figure 6.6a clearly shows that, for the entire duration of the test, the expansion in the de Laval nozzle occurs in a thermodynamic region in which the fundamental derivative of gasdynamics Γ is lower than 1. The corresponding PIG value is always greater than 1 and constant, regardless of operating conditions.

Fig. 6.6b and Fig. 6.6c report the pressure ratio and the Mach number profiles along the nozzle axis. Differently from perfect gases, the pressure ratio and the Mach number distribution along the nozzle axis, and therefore their exhaust values, are significantly influenced by the inlet thermodynamic conditions. The measured pressure ratios, with the corresponding uncertainty bars, are reported for reference in Fig. 6.6b alongside CFD results. As Γ_A increases, or, in other words, as total conditions in the settling chamber move towards more dilute conditions, the static to total pressure ratio at nozzle exhaust decreases, while the Mach number increases.

In the thermodynamic region explored in wind-tunnel tests, the non-ideal behaviour of the flow in the expansion process is determined by the non-ideal dependence of the speed of sound on density along isentropic transformations. The ratio of the local speed of sound c to the speed of sound calculated from thermodynamic model in reservoir conditions $c(P^t, T^t)$ is reported in Fig. 6.6d. Results obtained with using the iPRSV EoS differ from their PIG counterpart both quantitatively and qualitatively: while the PIG EoS delivers a speed of sound decreasing upon expansion in the isentropic process, the iPRSV EoS predicts a speed of sound increasing upon expansion for all the flow conditions attained during the test.

Since the flow variables at nozzle exhaust define the flow conditions upstream of the airfoil leading-edge shocks, it must be noted that, due to the non-ideal nature of the expansion occurring in the nozzle, not only the total variables in each flow condition are different, but also the pre-shock states $(P_A, v_A, \mathbf{u}_A, \vartheta)$. This effect is made even more apparent in Fig. 6.7, which reports

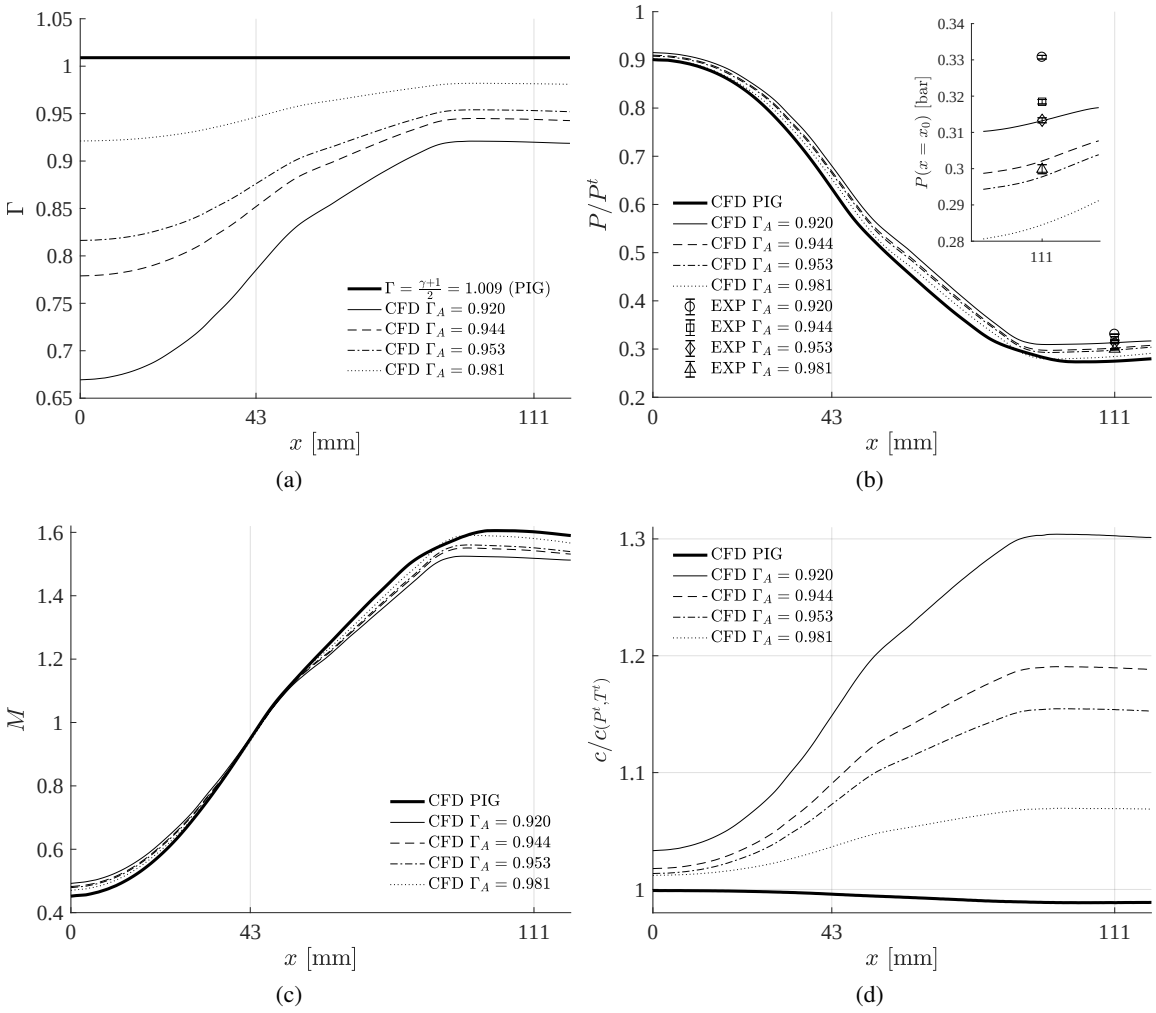

Figure 6.6: Expansion in the wind-tunnel supersonic nozzles. Profile of (a) Γ, (b) P/P^t, (c) M, and (d) $c/c(T^t, P^t)$ along the nozzle axis from numerical simulations and experiments. Test conditions are given in Tab. 6.2

the distribution of pressure P (in dimensional units) and Mach number M across the leading-edge shock and the expansion fan at the shoulder. In Fig. 6.7, results of the same Navier-Stokes simulations described so far are given in a portion of the domain which includes pressure taps 0, 1 and 3, i.e. the pre-shock, post-shock and post-expansion states. Results are extracted along a horizontal axis parallel to the nozzle symmetry axis, at a distance of 6.25 mm from the centreline, which corresponds to the line passing through pressure taps 1 and 3. On both profiles, pressure and Mach number measurements are reported for reference, together with the corresponding uncertainty bars. Overall, numerical simulations run using the iPRSV model agree with the experimental trends. Remarkably, the pressure plot of Fig. 6.7a reveals that the agreement between the measured and the computed pre-shock pressure, i.e. the pressure level achieved at nozzle exhaust, improves as dilute conditions are approached.

Figure 6.8 depicts the evolution of the flow layout at progressing testing time, or equivalently, at decreasing degree of non-ideality in the pre-shock state. Specifically, Fig. 6.8 depicts the flowfields simulated in three different test conditions, namely run 2-1, 2-2, and 2-4 (Tab. 6.2). Numerical results are obtained from Euler simulations using the iPRSV EoS. On the plot, equally spaced

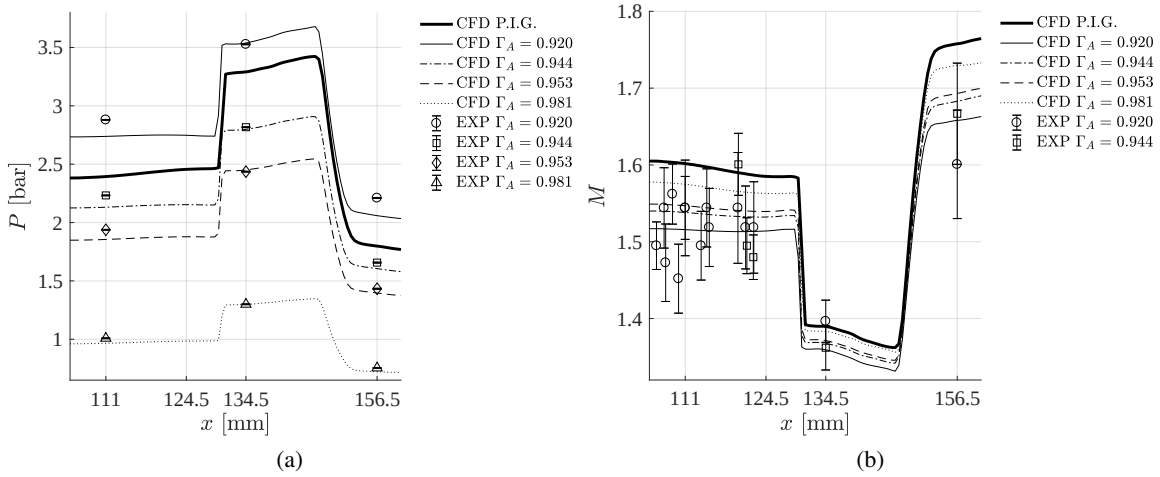

(a) (b)

Figure 6.7: Profile of (a) pressure, (b) Mach number across shock wave and expansion fan from experiments and numerical simulations. Test conditions are given in Tab. 6.2

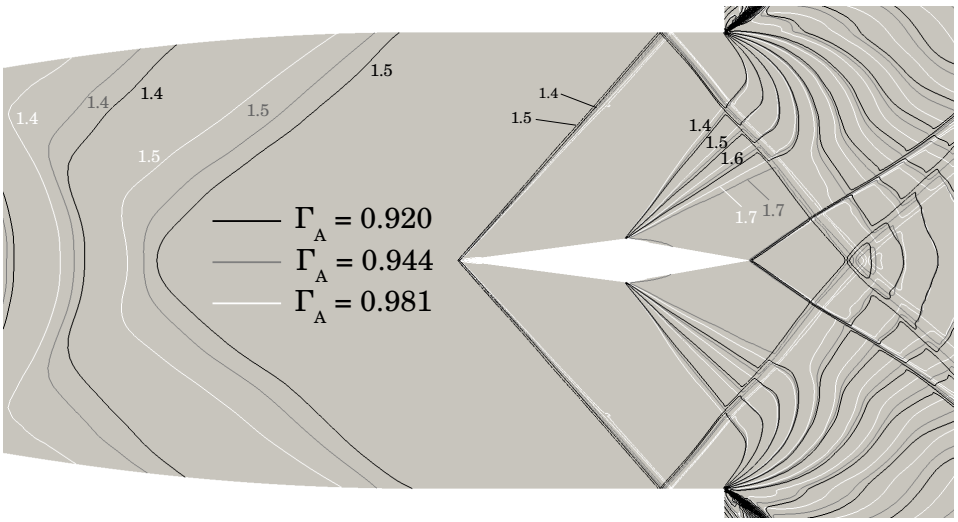

Figure 6.8: Mach number isolines for runs 2-1, 2-2, 2-4. Test conditions are given in Tab. 6.2

Mach number isolines covering the range $M = 0$ to 2.5 are reported. The flow layout in the three examined test conditions is influenced by the non-ideal effects commented so far. First, the Mach number distribution in the converging-diverging nozzle depends on inlet conditions. As more dilute conditions are reached, the exhaust Mach number increases and the flow progressively departs from the design point ($M_e = 1.5$), as indicated by the shape of the $M = 1.5$ isolines. Second, the shock angle β, which in turn depends on the pre-shock Mach number and thermodynamic state, varies during the test. The shock angle attains its largest value in the most non-ideal state (run 2-1) and its lowest value in close-to-ideal conditions (run 2-4). As already observed in Fig. 6.7b, the post-shock Mach number M_B changes from run 2-1 to run 2-4, following the variation of the pre-shock state. The third relevant non-ideal feature observed in Fig. 6.8 is the different Mach number distribution across the expansion fan obtained at varying test conditions, which can be ascribed to both the non-ideal dependence of the post-expansion state on upstream flow conditions and to the fact that the pre-expansion Mach number M_B changes during the test.

	$P_A^t \pm U_{P_A^t}$	$T_A^t \pm U_{T_A^t}$	$P_A \pm U_{P_A}$	Γ_A	run ID
Conf. $\mathcal{B}$	6.4802 ± 0.0092	259.3 ± 1.2	2.0699 ± 0.0030	0.939	6-1
$\alpha = 0°$	3.0088 ± 0.0092	258.2 ± 1.2	0.9120 ± 0.0030	0.981	6-4
Conf. $\mathcal{A}$	6.4247 ± 0.0091	255.5 ± 1.2	2.0566 ± 0.0030	0.937	1-1 and 4-1
$\alpha = 1°$	2.8405 ± 0.0091	250.5 ± 1.2	0.8679 ± 0.0030	0.981	1-4 and 4-4
Conf. $\mathcal{B}$	6.0510 ± 0.0092	256.9 ± 1.2	1.9160 ± 0.0030	0.943	3-1
$\alpha = 2°$	2.8452 ± 0.0091	250.6 ± 1.2	0.8493 ± 0.0030	0.981	3-4
Conf. $\mathcal{B}$	6.3010 ± 0.0091	253.4 ± 1.2	1.9993 ± 0.0030	0.937	5-1
$\alpha = 1°$	2.8289 ± 0.0092	249.8 ± 1.2	0.8537 ± 0.0030	0.981	5-4

Table 6.3: Tests performed at different flow deviation angles. Measured total temperature and pressure, measured pressure in the uniform supersonic flow upstream of the airfoil and Γ in the uniform flow from thermodynamic model. Pressures are expressed in bar, temperatures in °C.

6.1.3 Flow configurations at varying attitude of the airfoil

In chapter 5, tests run at varying attitude of the airfoil were described and experimental results were assessed against the inviscid shock-expansion theory. Experimental results were found to match theoretical predictions only for a subset of the examined geometrical configurations, namely the ones reported in Tab. 5.1 and Tab. 5.2. In all other tests, the wave pattern observed on the airfoil was qualitatively different from the expected one due to blockage effects. Moreover, particle deposition and vapour condensation on the front quartz window and on the polished back mirror of the test section hindered the achievement of useful schlieren images in many tests. Unavailability of schlieren visualizations for a large subset of the tested configurations motivated the effort of performing numerical simulations on all geometries, at varying total conditions. Indeed, numerical simulations allow to achieve a better understanding of the flow layout for all the test conditions whose corresponding schlieren visualization is missing. Moreover, Navier-Stokes simulations allow to simulate the boundary-layer growth on the walls of the test section, possibly capturing the prominent blockage effects observed in the experiments.

Navier-Stokes simulations of the test conditions reported in Tab. 6.3 are run using the iPRSV EoS. Results are shown Fig. 6.9. The plots report the pre-shock, post-shock and post-expansion pressures from experiments and numerical simulations. A spatial representation of the measured pressures is provided. Similarly to results presented in chapter 5, the post-expansion pressures computed in all geometrical configurations and the post-shock pressures corresponding to flow deviation angles greater than 10° (i.e. $\vartheta = 11°,\ 12°$) do not match the experimental results. Indeed, all simulations result in flow patterns qualitatively similar to the ones reported in Fig. 6.3 and in Fig. 6.8, thereby departing significantly from the flow layout observed in the experiments.

Figure 5.5c of chapter 5 depicts a schlieren visualization of the test at $\alpha = 1°$, configuration $\mathcal{B}$. A detail of the same schlieren image is reported here for convenience (Fig. 6.10a), and compared to the simulated flow-field (Fig. 6.10b). Flow conditions are labelled as run 5-1 in Tab. 6.3. In Fig. 6.10b, density isolines from Navier-Stokes (white lines) and Euler (black lines) simulations using the iPRSV EoS are reported. The simulation is run on the computational grid of Fig. 6.1.The simulated wave pattern is qualitatively different from the one observed in the experiment. Apparently, the numerical method adopted so far fails to predict the behaviour of the boundary layer on the walls confining the flow, including interactions with the incident shock waves. The failure is also possibly related to the fact that the steady CFD simulations do not account for the wind-tunnel start-up process, which eventually determines whether a supersonic flow is triggered in the

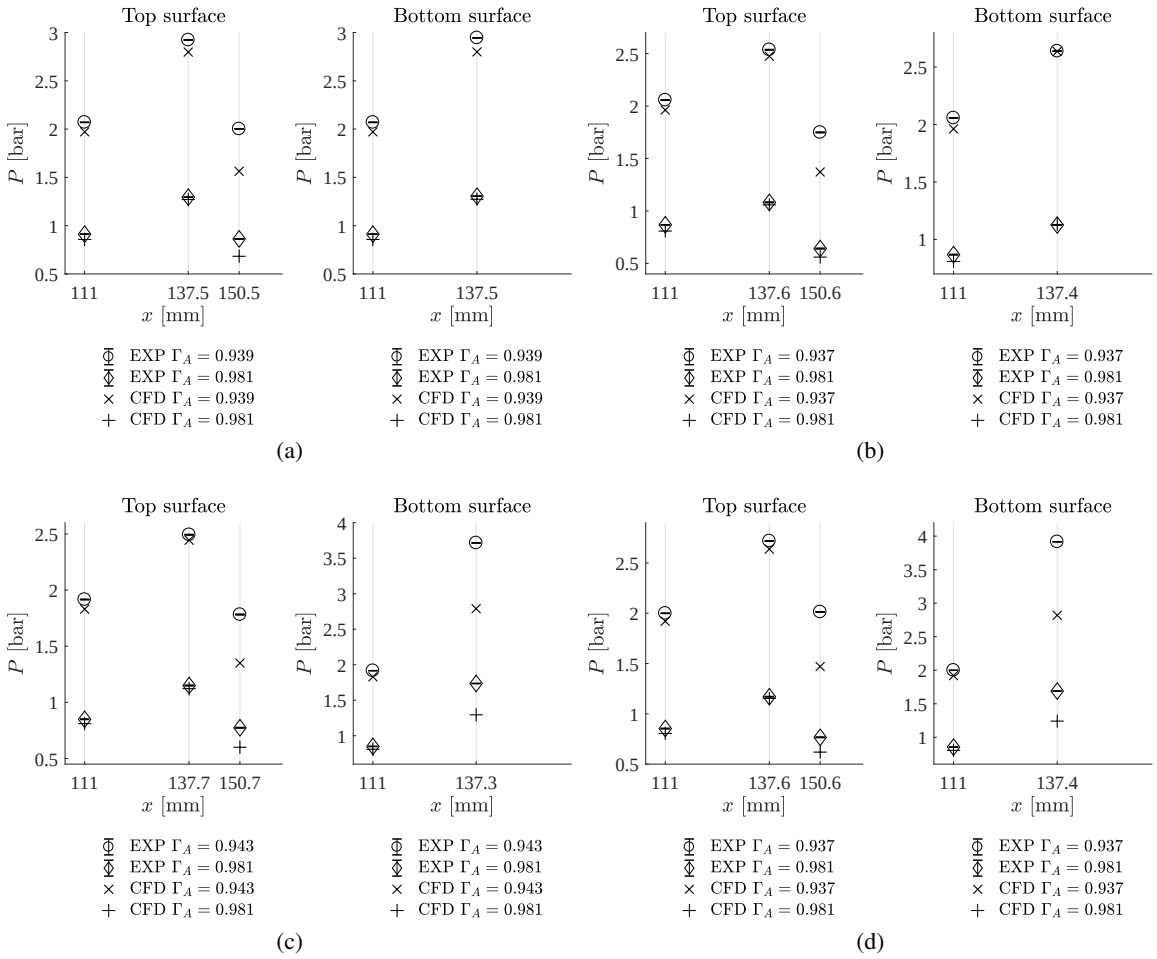

Figure 6.9: Pre-shock, post-shock and post-expansion states from experiments and numerical simulations. Test conditions are given in Tab. 6.3. (a) Runs 6-1 and 6-4: $\vartheta = 10°$ on top and bottom surface, (b) Runs 1-1 and 1-4 (4-1 and 4-4): $\vartheta = 6.5°$ on top surface ($\vartheta = 8.5°$ on bottom surface), (c) Runs 3-1 and 3-4: $\vartheta = 8°$ on top surface, $\vartheta = 12°$ on bottom surface, (d) Runs 5-1 and 5-4: $\vartheta = 9°$ on top surface, $\vartheta = 11°$ on bottom surface

test section.

Pre- and post-shock states from numerical simulations, limited to test conditions displaying a fine agreement with the experimental data, are reported in Tab. 6.4. The nomenclature is consistent with the one adopted in Tab. 5.1 of chapter 5, where the corresponding experimental results can be found.

6.2 Non-ideal nature of the oblique-wave pattern around the diamond airfoil

As mentioned in the introduction of the present thesis, chapter 1.3, recent works by Gori *et al.* (2017*a*) and Vimercati *et al.* (2017) report extensive theoretical and numerical studies on non-ideal oblique waves, which revealed the occurrence of oblique shock waves featuring Mach number increase across the shock in the non-ideal classical regime. These non-ideal shock waves slow the flow and carry a compression. Though, the decrease of the speed of sound across the shock causes an increase in the tangential Mach number which, for certain inlet conditions, compensates

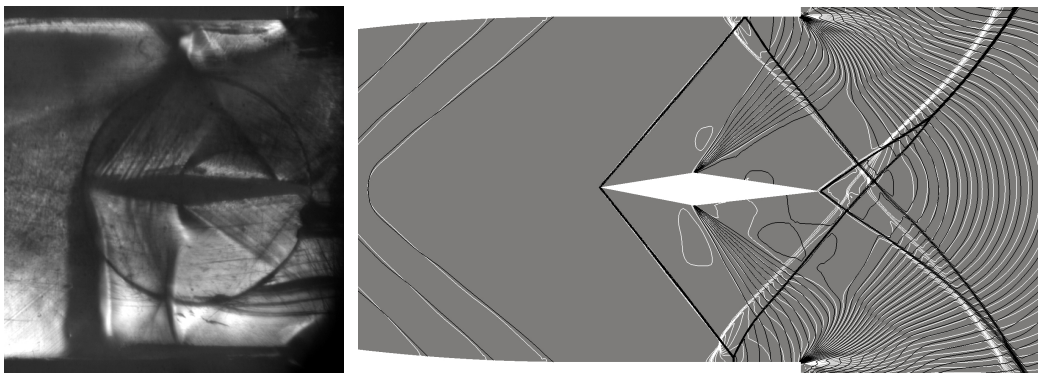

(a) (b)

Figure 6.10: (a) Schlieren image of the test in Configuration $\mathcal{B}$, $\alpha = 1°$. (b) Euler (black) and Navier-Stokes (white) density isolines obtained in the same geometrical configuration. Flow conditions are labelled as run 5-1 in Tab. 6.3

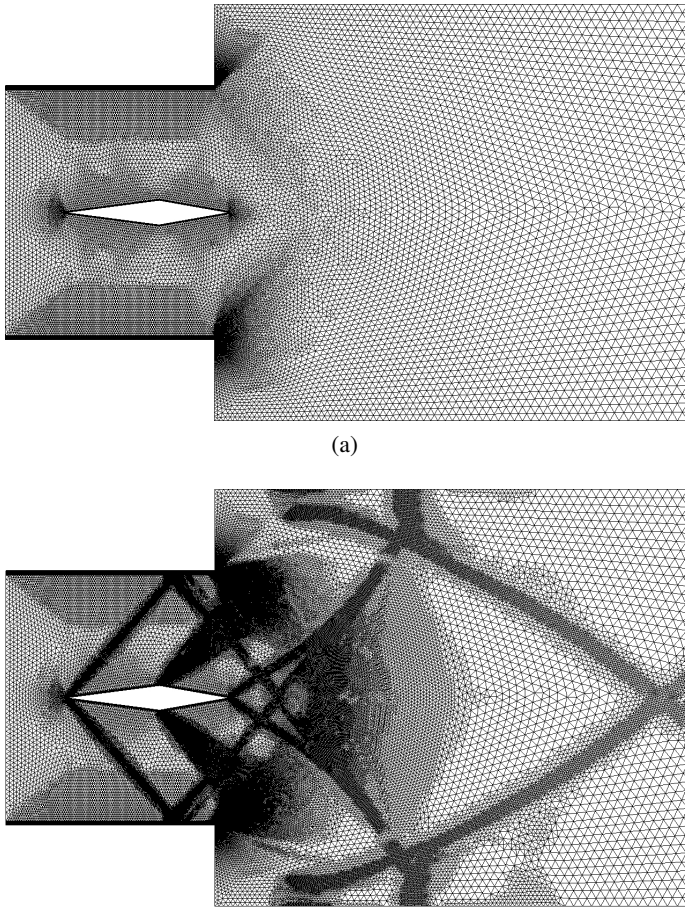

(a)

(b)

Figure 6.11: Computational grid. (a) Baseline (50k elements), (b) Adapted (220k elements)

ϑ	P_A^t	T_A^t	P_A	T_A	Γ_A	M_A	P_B	T_B	Γ_B	M_B	β	run ID
6.5	6.4247	255.5	1.9618	241.33	0.937	1.534	2.4740	243.47	0.912	1.390	46.88	1-1
6.5	5.9847	255.6	1.8080	241.83	0.944	1.541	2.2934	244.01	0.924	1.392	46.56	1-2
6.5	4.9525	254.8	1.4656	241.71	0.957	1.555	1.8763	243.85	0.942	1.397	46.17	1-3
6.5	2.8405	250.5	0.8089	238.56	0.981	1.580	1.0576	240.73	0.972	1.405	45.45	1-4
7.5	8.7076	277.6	2.7273	261.67	0.920	1.518	3.5016	264.39	0.891	1.363	47.85	2-1
7.5	7.0109	279.1	2.1181	264.52	0.944	1.542	2.7747	267.19	0.922	1.370	47.05	2-2
7.5	6.1849	278.4	1.8416	264.36	0.953	1.551	2.4327	267.00	0.934	1.373	46.89	2-3
7.5	3.3633	274.6	0.9569	266.47	0.981	1.581	1.2954	269.04	0.972	1.380	46.01	2-4
8	6.0510	256.9	1.8296	243.03	0.943	1.540	2.4435	245.83	0.919	1.356	48.83	3-1
8	5.5659	259.6	1.6616	245.95	0.951	1.549	2.2393	248.84	0.930	1.356	48.31	3-2
8	4.6788	259.1	1.3727	246.04	0.962	1.560	1.8672	248.94	0.945	1.359	47.98	3-3
8	2.8452	250.6	0.8099	238.69	0.981	1.580	1.1217	241.50	0.970	1.362	47.62	3-4
8.5	6.4247	255.5	1.9618	241.33	0.937	1.534	2.6354	244.17	0.909	1.348	47.84	4-1
8.5	5.9847	255.6	1.8080	241.83	0.944	1.541	2.4458	244.71	0.918	1.349	47.64	4-2
8.5	4.9525	254.8	1.4656	241.71	0.957	1.555	2.0054	244.54	0.937	1.353	47.22	4-3
8.5	2.8405	250.5	0.8089	238.56	0.981	1.580	1.1307	241.34	0.970	1.358	46.48	4-4
9	6.3010	253.4	1.9202	239.35	0.937	1.535	2.6370	242.47	0.907	1.331	49.55	5-1
9	5.9354	254.4	1.7939	240.57	0.943	1.540	2.4762	243.75	0.916	1.332	49.20	5-2
9	4.8687	254.3	1.4388	241.15	0.958	1.556	2.0129	244.37	0.936	1.334	48.64	5-3
9	2.8289	249.8	0.8054	237.89	0.981	1.579	1.1532	241.03	0.969	1.338	48.03	5-4
10	6.4802	259.3	1.9716	245.08	0.939	1.536	2.7973	248.61	0.905	1.309	49.91	6-1
10	6.1910	261.4	1.8695	247.36	0.944	1.541	2.6652	250.97	0.913	1.309	49.69	6-2
10	4.6625	261.1	1.3666	248.00	0.963	1.561	1.9862	251.59	0.942	1.310	49.23	6-3
10	3.0088	258.2	0.8569	246.02	0.981	1.579	1.2706	249.53	0.967	1.311	48.69	6-4

Table 6.4: Pre- and post-shock states from numerical simulations (Navier-Stokes, iPRSV). Pressures are expressed in bar, temperatures in °C, and angles in degrees. The values of Γ_A are computed using the SW EoS from the measured values of P_A^t, T_A^t and P_A and assuming that both the entropy and total enthalpy are constant from the reservoir to the pressure tap upstream of the airfoil

the decrease in the normal Mach number required by shock stability. The non-ideal increase of the flow Mach number across shock waves is not expected to be observed in the experimental campaign presented here. Indeed, the thermodynamic region explored in all the tests does not overlap with the thermodynamic region in which the non-ideal increase of the Mach number is predicted to occur, according to the analysis by Gori *et al.* (2017*a*) and Vimercati *et al.* (2017). In the present context, expected departs from ideality include the dependence of the post-shock and post-expansion states on the upstream flow conditions and a speed of sound decreasing across shock waves and increasing across expansion waves.

In the previous paragraph 6.1, numerical simulations of the flow within the test section of the TROVA were discussed to show the influence flow non-ideality and blockage effects on the flow pattern observed around the airfoil.

The test condition identified as run 2-1 in Tab. 6.2 is now simulated on the computational grid of Fig. 6.11. Differently from simulations presented in the previous paragraph, the flow domain includes only the constant-area duct housing the airfoil and a portion of the downstream ambient. The goal of the present analysis is to investigate the non-ideal nature of the oblique wave pattern observed around the airfoil, by comparing results of Navier-Stokes simulations run using the PIG and iPRSV EoS. Differently from simulations including the wind-tunnel nozzle, a uniform supersonic flow is imposed at the inlet boundary. The flow condition at the inflow boundary is defined by the measured pre-shock pressure and by the temperature and Mach number calculated considering an isentropic expansion in the wind-tunnel nozzle. Figure 6.11 shows the baseline grid (Fig. 6.11a) and the grid after three levels of adaptive refinement (Fig. 6.11b). The baseline and the final grid are made of 50k and 220k elements, respectively.

Figure 6.12 reports the distribution of pressure P, Mach number M, velocity module u and speed of sound c across the leading-edge shock and the expansion fan originating on the airfoil. Results are extracted from the Navier-Stokes PIG and iPRSV simulations, along the horizontal line passing through pressure taps 1 and 3, and refer to a portion of the domain extending from the exhaust section of the nozzle to the trailing edge of the airfoil. The pressure and Mach number profiles of Fig. 6.12a and Fig. 6.12b are compared to pressure and Mach number measurements.

Numerical results obtained using the iPRSV model match the experimental data more closely than the ones obtained using PIG model. However, the iPRSV simulation only loosely reproduce the pressure and Mach number jumps across the shock wave and the expansion fan measured from experiments. The trends of pressure, Mach number and velocity module computed using the PIG model (Fig. 6.7a-c) qualitatively match the ones obtained using the iPRSV EoS. However, the PIG model predicts a completely different behaviour of the speed of sound across the shock wave and the expansion fan, as can be observed in Fig. 6.7d. Both according to the PIG and iPRSV EoS, shock waves compress and slow the flow, while expansion fans expand and accelerate the flow. However, the speed of sound from the iPRSV simulation decreases across the shock and increases across the expansion fan, contrarily to the one resulting from the PIG simulation.

6.3 Conclusions

The SU2 CFD tool is applied to the simulation of supersonic non-ideal flows with oblique waves observed in the TROVA wind tunnel. Numerical simulations reproduce all the geometrical configurations and operating conditions investigated in wind-tunnel tests. Steady-state Euler and Navier-Stokes simulations are run and results obtained using different thermodynamic models are compared to the available experimental data. In the inviscid core of the flow, where pressure measurement points are located, results from both Euler and Navier-Stokes simulations complemented with non-ideal EoS agree fairly well with experimental data. The non-ideal nature of the

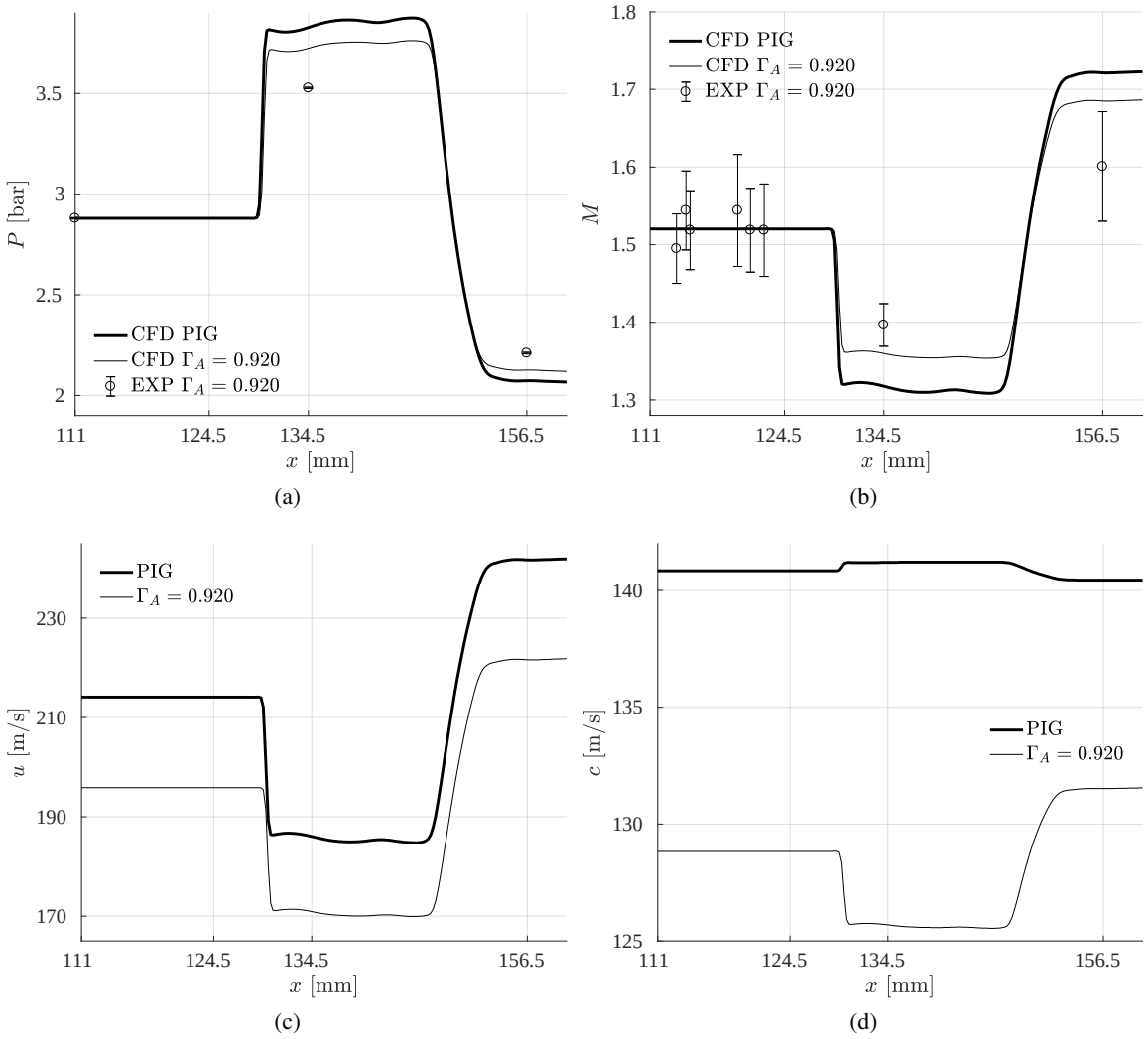

Figure 6.12: Profile of (a) pressure, (b) Mach number, (c) velocity module, (d) speed of sound across shock wave and expansion fan from experiments and numerical simulations. Test conditions are given in Tab. 6.2

expansion in the wind-tunnel nozzle and of the oblique wave pattern around the airfoil is correctly described by the numerical model. Namely, a significant dependence of the pre-shock, post-shock and post-expansion states on the corresponding upstream flow conditions is found, and the typical behaviour of the speed of sound across compressions and expansions taking place in the non-ideal classical regime is obtained. Consistently with experiments, the configuration of the wave pattern around the airfoil noticeably changes at varying operating conditions. Indeed, the shock angle and the slope of the expansion waves depend on upstream flow conditions. The flow conditions attained upstream of the airfoil, in turn, significantly depart from the design point of the wind-tunnel nozzle at progressing testing time, or, equivalently, as more dilute conditions in the total thermodynamic states are reached. Though inviscid flow features are properly described by the numerical model, the shock-boundary layer interaction on the upper and lower walls of the test section is not correctly reproduced, not even by Navier-Stokes simulations.

7 Conclusions and outlook

Experimental campaigns were carried out in the TROVA blow-down wind tunnel to characterize the NICFD flow of siloxane vapour MDM in planar converging-diverging nozzles and around a diamond-shaped airfoil. The non-ideal expansion processes occurring in supersonic nozzles of different shape and the oblique shock waves and expansion fans originating on the diamond airfoil were characterized by means of pressure and temperature measurements and schlieren visualizations.The flow arrangements analyzed in the present thesis are relevant to both fundamental research in the field of NICFD and to industrial applications. Remarkably, ORC turbine stators are converging-diverging nozzles, featuring expansion to supersonic conditions, shock-boundary-layer interaction, and fish-tail shock patterns, namely oblique shock waves at the blade trailing edge.

Performing accurate measurements in high-temperature and potentially condensing vapor flows is a challenging task, mostly because of difficulties related to the application of measurement techniques specifically developed and tested for dilute gases. Results presented in this thesis are a contribution to the experimental research aimed at providing the first reference datasets for non-ideal fluid flows. Assessment of thermodynamic models and CFD tools for NICFD flows indeed demands reliable reference experimental data. Throughout the thesis, experimental results were assessed against the NICFD theory and numerical simulations, complemented with state-of-the-art thermodynamic models.

Theoretical and numerical studies were carried out to design the nozzle shape and compute the nozzle discharge coefficient, thus evidencing its non-ideal dependence on the reservoir state. In a recent theoretical study, the discharge coefficient of planar converging-diverging nozzles was found to depend lineary on the fundamental derivative of gasdynamics in the sonic state and on the inverse of the second and third power of the curvature radius at the throat section. Numerical simulations presented in this work provided assessment of the functional dependence of the discharged massflow rate on the mentioned parameters. Moreover, the dependence of the discharged massflow rate on the geometry of the nozzle was found to be related to the overall shape of the converging portion, and not only to the local curvature of the nozzle profile in the close proximity of the throat. A possible future development downstream of this study may include the experimental verification of the present findings.

Nozzle flows and flows embedding oblique waves observed in experiments were proven to be non-ideal, since the inlet thermodynamic conditions were seen to significantly affect the flow dynamics, contrarily to the well-known behavior of perfect gases. In wind-tunnel testing of flows with oblique waves, the non-ideal nature of the expansion in the wind-tunnel nozzle and blockage effects played a major role. The former was found to influence the inviscid flow layout, viz. the shock angle and the slope of the expansion waves, while the latter shaped the interaction between the shock waves generated within the test section and the wall boundary layer.

Results obtained in the present work further confirm the need of accounting for non-ideal effects in the design and analysis of aerodynamic devices operating with molecularly complex vapours in thermodynamic states close to the liquid-vapour saturation curve and critical point. Moreover, the measurement techniques applied to the observation of NICF flows of pure siloxane vapour MDM proven to be suitable to the identification of non-ideal effects in compressible flows, thus setting a reliable methodology for future experimental investigations. Experimental campaigns envisaged for the near future include the observation of two peculiar phenomena occurring in the non-ideal classical regime, namely the non-monotone behaviour of the Mach number along

isentropic expansions in supersonic nozzles and non-ideal oblique shock waves featuring a Mach number increase across the shock. Experiments on both pure fluids and mixtures of siloxane vapours are planned.

Bibliography

ANDERSON, J. D. 2004 *Modern Compressible Flow: with Historical Perspective, Third Edition*. McGraw Hill Higher Education.

ANGELINO, G., INVERNIZZI, C. & MACCHI, E. 1991 Organic Working Fluid Optimization for Space Power Cycles. In *Modern Research Topics in Aerospace Propulsion* (ed. G. Angelino, L. De-Luca & W. A. Sirignano), chap. 16. New York: Springer.

ANTONINI, C., PERSICO, G. & ROWE, L. 2008 Prediction of the dynamic response of complex transmission line systems for unsteady pressure measurements. *Measurement Science and Technology* **19** (12), 125401.

BETHE, H. A. 1942 On the Theory of Shock Waves for an Arbitrary Equation of State. *Tech. Rep.* No. 545, NDRC-B-237. Office of Scientific Research and Development.

BLAZEK, J. 2005 *Computational Fluid Dynamics: Principles and Applications*. Elsevier.

BROWN, B. & ARGROW, B. 2000 Application of Bethe-Zel'dovich-Thompson Fluids in Organic Rankine Cycle Engines. *Journal of Propulsion and Power* **16** (6), 1118–1124.

BRUN, K., FRIEDMAN, P. & DENNIS, R. 2017 *Fundamentals and Applications of Supercritical Carbon Dioxide (SCO_2) Based Power Cycles*, 1st edn. Elsevier.

CALLEN, H B 1985 *Thermodynamics and an introduction to thermostatistics*, 2nd edn. Wiley.

CHAPMAN, D. R. 1950 An analysis of base pressure at supersonic velocities and comparison with experiment. *Tech. Rep.* NACA TN 2137. National Advisory Committee for Aeronautics.

CINNELLA, P., CONGEDO, P. M., PEDIRODA, V. & PARUSSINI, L. 2010 Quantification of Thermodynamic Uncertainties in Real Gas Flows. *International Journal of Engineering Systems Modelling and Simulation* **2**, 12–24.

COLONNA, P., CASATI, E., TRAPP, C., MATHIJSSEN, T., LARJOLA, J., TURUNEN-SAARESTI, T. & UUSITALO, A. 2015 Organic Rankine Cycle Power Systems: From the Concept to Current Technology, Applications and an Outlook to the Future. *ASME Journal of Engineering for Gas Turbines and Power* **137**, 100801.

COLONNA, P. & GUARDONE, A. 2006 Molecular Interpretation of nonclassical gasdynamics of dense vapors under the van der Waals model. *Physics of Fluids* **18** (5), 56101–56114.

COLONNA, P., GUARDONE, A., NANNAN, R. & ZAMFIRESCU, C. 2008*a* Design of the dense gas Flexible Asymmetric Shock Tube. *Journal of Fluids Engineering* **130**, 34501–34506.

COLONNA, P., GUARDONE, A. & NANNAN, R. N. 2007 Siloxanes: A New Class of Candidate Bethe-Zel'dovich-Thompson Fluids. *Physics of Fluids* **19** (086102).

COLONNA, P., HARINCK, J., REBAY, S. & GUARDONE, A. 2008*b* Real-gas effects in Organic Rankine Cycle turbine nozzles. *Journal of Propulsion and Power* **24** (2), 282–294.

COLONNA, P., NANNAN, N. R. & GUARDONE, A. 2008*c* Multiparameter equations of state for siloxanes. *Fluid Phase Equilib.* **263**, 115–130.

COLONNA, P. & VAN DER STELT, T. P. 2005 FluidProp: A program for the estimation of thermophysical properties of fluids. Energy Technology Section, Delft University of Technology, The Netherlands(www.fluidprop.com).

CONGEDO, P. M., CORRE, C., COLONNA, P., WITTEVEEN, J. & IACCARINO, G. 2012 Backward uncertainty propagation method in flow problems: application to the prediction of rarefaction shock-waves. *Comput. Methods Appl. Mech. Engrg* **213–216**, 314–326.

CONTI, C. C., SPINELLI, A., CAMMI, G., ZOCCA, M. & GUARDONE, A. 2017 Schlieren visualizations of non-ideal compressible-fluid flows. In *13th International Conference on Heat Transfer, Fluid Mechanics and Thermodynamics, HEFAT 2017*.

COZZI, F., SPINELLI, A., CARMINE, M., CHELI, R., ZOCCA, M. & GUARDONE, A. 2015 Evidence of complex flow structures in a converging-diverging nozzle caused by a recessed step at the nozzle throat. In *45th AIAA Fluid Dynamics Conference*.

CRAMER, M. S. & BEST, L. M. 1991 Steady, isentropic flows of dense gases. *Physics of Fluids A: Fluid Dynamics* **3** (4), 219.

CRAMER, M. S. & FRY, R. N. 1993 Nozzle flows of dense gases. *Physics of Fluids* **5** (5), 1246–1259.

DENTON, J. D. 1993 Loss mechanisms in turbomachines. In *International Gas Turbine and Aeroengine Congress and Exposition*, pp. 93–GT–435.

DUSSIN, D., FOSSATI, M., GUARDONE, A. & VIGEVANO, L. 2009 Hybrid grid generation for two-dimensional high-Reynolds flows. *Computers & Fluids* **38**, 1863–1875.

FEHER, E. G. 1968 The Supercritical Thermodynamic Power Cycle. *Energy Conversion* **8**, 85–90.

GALIANA, F. J. DURÁ, WHEELER, A. P. S., ONG, J. & DE M. VENTURA, C. A. 2017 The effect of dense gas dynamics on loss in ORC transonic turbines. *Journal of Physics: Conference Series* **821** (1), 012021.

GORI, G., GUARDONE, A., VITALE, S., HEAD, A. J., PINI, M. & COLONNA, P. 2015 Non-Ideal Compressible-Fluid Dynamics simulation with SU2: numerical assessment of nozzle and blade flows for Organic Rankine Cycle applications. In *3rd International Seminar on ORC Power Systems*.

GORI, G., VIMERCATI, D. & GUARDONE, A. 2017*a* Non-ideal compressible-fluid effects in oblique shock waves. *Journal of Physics: Conference Series* **821** (1), 012003.

GORI, G., ZOCCA, M., CAMMI, G., SPINELLI, A. & GUARDONE, A. 2017*b* Experimental assessment of the open-source SU2 CFD suite for ORC applications. *Energy Procedia* **129** (Supplement C), 256–263.

GUARDONE, A. 2010 Real-gas effects in supercritical carbon dioxide gasdynamic nozzles. In *Proceedings of the 6th International Conference on Heat Transfer, Fluid Mechanics and Thermodynamicsi, Antalya, Turkey*.

GUARDONE, A. 2011 Nozzle Design for Supersonic Flows of N_2O at Supercritical and Close-to-Critical Conditions. In *8th International Conference on Flow Dynamics*.

GUARDONE, A. 2015 Effects of molecular complexity and reservoir conditions on the discharge coefficient of adapted planar nozzles. *Journal of Physics: Conference Series* **633**, 012092.

GUARDONE, A., ISOLA, D. & QUARANTA, G. 2011 Arbitrary Lagrangian Eulerian formulation for two-dimensional flows using dynamic meshes with edge swapping. *Journal of Computational Physics* **230**, 7706–7722.

GUARDONE, A., SPINELLI, A. & DOSSENA, V. 2013 Influence of Molecular Complexity on Nozzle Design for an Organic Vapor Wind Tunnel. *ASME Journal of Engineering for Gas Turbines and Power* **135**, 042307.

GUARDONE, A. & VIMERCATI, D. 2016 Exact solutions to non-classical steady nozzle flows of Bethe-Zel'dovich-Thompson fluids. *Journal of Fluid Mechanics* **800**, 278–306.

GYFTOPOULOS, E. & BERETTA, G. P. 1991 *Thermodynamics Foundations and Applications*. Dover Publications, Inc.

HALUPOVICH, Y., NATAN, B. & ROM, J. 1999 Numerical solution of the turbulent supersonic flow over a backward facing step. *Fluid Dynamics Research* (24), 251–273.

HAMA, F. R. 1966 Experimental Investigations of Wedge Base Pressure and Lip Shock. *Tech. Rep.* NASA TR 32-1033. National Aeronautics and Space Administration.

HARTFIELD, R. J., HOLLO, S. D. & MCDANIEL, J. C. 1993 Planar measurement technique for compressible flows using laser induced iodine fluorescence. *AIAA Journal* **25** (3), 483–490.

HEAD, A. J., IYER, S., DE SERVI, C. & PINI, M. 2017 Towards the Validation of a CFD Solver for Non-ideal Compressible Flows. *Energy Procedia* **129** (Supplement C), 240–247.

HEAD, A. J., DE SERVI, C., CASATI, E., PINI, M. & COLONNA, P. 2016 Preliminary Design of the ORCHID: A Facility for Studying Non-Ideal Compressible Fluid Dynamics and Testing ORC Expanders. In *ASME Turbo Expo 2016: Turbomachinery Technical Conference and Exposition*.

HELFGEN, B., TÜRK, M. & SCHABER, K. 2003 Hydrodynamic and aerosol modelling of the rapid expansion of supercritical solutions (ress-process). *Journal of Supercritical Fluids* **26**, 225–242.

HUNG, P. C., IRWIN, G., KEE, R. & MCLOONE, S. 2005 Difference equation approach to two-thermocouples sensor characterization in constant velocity flow environment. *Review of Scientific Instruments* **76** (024902).

ISHIKO, K. & SHIMADA, T. 2010 Implicit LES of Compressible Turbulent Flow over a Backward-Facing Step in the Nozzle of Solid Rocket Motor. In *48th AIAA Aerospace Sciences Meeting Including the New Horizons Forum and Aerospace Exposition*.

JCGM-WG1 2008 Evaluation of Measurement Data – Supplement 1 to the 'Guide to the Expression of Uncertainty in Measurement' – Propagation of distributions using a Monte Carlo method. *Tech. Rep.*. IUPAC, BIECIIIS, OIML, IUPAP.

KLUWICK, A. 1993 Transonic nozzle flow of dense gases. *Journal of Fluid Mechanics* **247**, 661–688.

KLUWICK, A. 2004 Internal flows of dense gases. *Acta Mech.* **169** (1-4), 123–143.

KLUWICK, A. 2017 Non-Ideal Compressible Fluid Dynamics: A Challenge for Theory. *Journal of Physics: Conference Series* **821** (1), 012001.

KORST, H. H., PAGE, R. H. & CHILDS, M. E. 1955 A Theory for Base Pressure in Transonic and Supersonic Flows. *Tech. Rep.* ME-TN-392-2. University of Illinois, US.

KRULL, H. G., BEALE, W. T. & SCHMIEDLIN, R. F. 1955 Effect of several design variables on internal performance of convergent-plug exhaust nozzles. *Tech. Rep.* NACA RM E54L09. National Advisory Committee for Aeronautics.

LAMBRAKIS, K. C. & THOMPSON, P. A. 1972 Existence of Real Fluids with a Negative Fundamental Derivative Γ. *Physics of Fluids* **15** (5), 933–935.

LARJOLA, J. 1995 Electricity from industrial waste heat using high-speed Organic Rankine Cycle (ORC). *International Journal of Production Economics* **41**, 227–235.

LAX, P. D. 1957 Hyperbolic systems of conservation laws, II. *Comm. Pure Appl. Math.* **10**, 537–566.

VAN LEER, B. 1979 Towards the ultimate conservative difference scheme. V. A second-order sequel to Godunov's method. *Journal of Computational Physics* **32** (1), 101–136.

LEMMON, E. W., HUBER, M. L. & MCLINDEN, M. O. 2013 NIST reference database 23: reference fluid thermodynamic and transport properties–REFPROP, version 9.1. *Standard Reference Data Program* .

LO, R. C. & TSAI, W. H. 1995 Gray-scale Hough trasform for thick line detection in grey-scale images. *Pattern Recognition* **28**, 647–661.

MACCHI, E. & ASTOLFI, M., ed. 2016 *Organic Rankine Cycle (ORC) Power Systems Technologies and Applications*, 1st edn. Elsevier.

MATHIJSSEN, T., GALLO, M., CASATI, E., NANNAN, N. R., ZAMFIRESCU, C., GUARDONE, A. & COLONNA, P. 2015 The flexible asymmetric shock tube (FAST): a Ludwieg tube facility for wave propagation measurements in high-temperature vapours of organic fluids. *Experiments in Fluids* **56** (10), 195.

MCKAY, M. D., BECKMAN, R. J. & CONOVER, W. J. 2000 A comparison of three methods for selecting values of input variables in the analysis of output from a computer code. *Technometrics* **42** (1), 55–61.

MENTER, F. R. 1994 Two-Equation Eddy-Viscosity Turbulence Models for Engineering Applications. *AIAA Journal* **32** (8), 1598–1605.

MONTAGNE, J. L. & VINOKUR, M. 1990 Generalized flux-vector splitting and Roe average for an equilibrium real gas. *Journal of Computational Physics* **89** (2), 276–300.

O'BYRNE, S., DANEHY, P. M. & HOUWING, A. F. P. 2006 Investigation of hypersonic nozzle flow uniformity using no fluorescence. *Shock Waves* **15** (2), 81–87.

OLEINIK, O. 1959 Uniqueness and stability of the generalized solution of the Cauchy problem for a quasilinear equation. *Uspehi Mat. Nauk.* **14**, 165–170.

PALACIOS, F., COLONNO, M. F., ARANAKE, A. C., CAMPOS, A., COPELAND, S. R., ECONOMON, T. D., LONKAR, A. K., LUKACZYK, T. W., TAYLOR, T. W. R. & ALONSO, J. J. 2013 Stanford University Unstructured (SU2): An open-source integrated computational environment for multi-physics simulation and design. In *51st AIAA Aerospace Sciences Meeting and Exhibit*.

PINI, M., SPINELLI, A., DOSSENA, V., GAETANI, P. & CASELLA, F. 2011 Dynamic Simulation of a Test Rig for Organic Vapours. In *ASME 2011 5th International Conference on Energy Sustainability*, pp. 1977–1988.

PINI, M., VITALE, S., COLONNA, P., GORI, G., GUARDONE, A., ECONOMON, T., ALONSO, J. J. & PALACIOS, F. 2017 SU2: the Open-Source Software for Non-ideal Compressible Flows. *Journal of Physics: Conference Series* **821** (1), 012013.

POPE, A. 1978 *High-speed wind tunnel testing*. Krieger Pub Co.

REINKER, F., HASSELMANN, K., AUS DER WIESCHE, S. & KENIG, E. Y. 2016 Thermodynamics and Fluid Mechanics of a Closed Blade Cascade Wind Tunnel for Organic Vapors. *Journal of Engineering for Gas Turbines and Power* **138**, 052601.

REINKER, F., KENIG, E. Y., PASSMANN, M. & AUS DER WIESCHE, S. 2017 Closed Loop Organic Wind Tunnel (CLOWT): Design, Components and Control System. *Energy Procedia* **129** (Supplement C), 200–207.

ROSHKO, A. & THOMKE, G. J 1966 Observations of Turbulent Reattachment behind an Axisymmetric Dolvnstream-Facing Step in Supersonic Flow. *AIAA Journal* **4** (6), 975–980.

SAGNIER, P. & VÉRANT, J. L. 1998 On the validation of high enthalpy wind tunnel simulations. *Aerospace Science and Technology* (7), 425–437.

SAUER, R. 1947 General characteristics of the flow through nozzles at near critical speeds. TM 1147. NACA.

SMITH, H. E. 1967 The flow field and heat transfer downstream of a rearward facing step in supersonic flow. *Tech. Rep.* ARL 67-0056. Aerospace Research Laboratories.

SPALART, P. R. & ALLMARAS, S. R. 1994 A one-equation turbulence model for aerodynamic flows. *La Recerche Aérospatiale* **1**, 5–21.

SPAN, R. 2000 *Multiparameter equations of state: an accurate source of thermodynamic property data*. Springer: Berlin.

SPAN, R. & WAGNER, W. 2003 Equations of State for Technical Applications. I. Simultaneously Optimized Functional Forms for Nonpolar and Polar Fluids. *Int. J. Thermophys.* **24** (1), 1–39.

SPINELLI, A., CAMMI, G., ZOCCA, M., GALLARINI, S., COZZI, F., DOSSENA, V., GAETANI, P. & GUARDONE, A. 2017*a* Experimental observation of supersonic non-ideal compressible-fluid nozzle flows of siloxane MDM. *Energy Procedia* **129** (Supplement C), 1125–1132.

SPINELLI, A., COZZI, F., CAMMI, G., ZOCCA, M., GAETANI, P., DOSSENA, V. & GUARDONE, A. 2017*b* Preliminary characterization of an expanding flow of siloxane vapor MDM. *Journal of Physics: Conference Series* **821** (1), 012022.

SPINELLI, A., COZZI, F., DOSSENA, V., GAETANI, P., ZOCCA, M. & GUARDONE, A. 2016 Experimental investigation of a non-ideal expansion flow of siloxane vapor MDM. In *ASME Turbo Expo 2016: Turbomachinery Technical Conference and Exposition*.

SPINELLI, A., PINI, M., DOSSENA, V., GAETANI, P. & CASELLA, F. 2013 Design, Simulation, and Construction of a Test Rig for Organic Vapours. *ASME Journal of Engineering for Gas Turbines and Power* **135**, 042303.

STANEWSKY, E. 1973 Shock-Boundary Layer Interaction in Transonic and Supersonic Flows. In *Lecture Series 59 on Transonic Flows in Turbomachinery*. Von Karman Institute for Fluid Dynamics.

VAN DER STELT, T. P., NANNAN, N. R. & COLONNA, P. 2012 The iPRSV equation of state. *Fluid Phase Equilib.* **330**, 24–35.

SUTTON, G. P. & BIBLARZ, O. 2001 *Rocket Propulsion Elements*. New York: John Wiley & Sons, Inc.

THOL, M., DUBBERKE, F. H., BAUMHÖGGER, E., VRABEC, J. & SPAN, R. 2017 Speed of Sound Measurements and Fundamental Equations of State for Octamethyltrisiloxane and Decamethyltetrasiloxane. *Journal of Chemical Engineering Data* **62**, 2633–2648.

THOMPSON, P. A. 1971 A Fundamental Derivative in Gasdynamics. *Physics of Fluids* **14** (9), 1843–1849.

THOMPSON, P. A. 1988 *Compressilbe-Fluid Dynamics*. McGraw-Hill.

TOMITA, T., TAKAHASHI, M., SASAKI, M., TAKAHASHI, M., TAMURA, H., WATANABE, Y. & TSUBOI, M. 2003 Parametric Study on the Influence of a Discontinuous Step in a Nozzle Contour on Side-load. In *39th AIAA/ASME/SAE/ASEE Joint Propulsion Conference and Exhibit*.

TROPEA, C., YARIN, A. & FOSS, J. F., ed. 2007 *Springer Handbook of Experimental Fluid Mechanics*. Springer.

TURUNEN-SAARESTI, T., UUSITALO, A. & HONKATUKIA, J. 2017 Design and testing of high temperature micro-ORC test stand using Siloxane as working fluid. *Journal of Physics: Conference Series* **821** (1), 012024.

UUSITALO, A., HONKATUKIA, J. & TURUNEN-SAARESTI, T. 2017 Evaluation of a small-scale waste heat recovery organic Rankine cycle. *Applied Energy* **192**, 146–158.

VIMERCATI, D., GORI, G., SPINELLI, A. & GUARDONE, A. 2017 Non-ideal effects on the typical trailing edge shock pattern of ORC turbine blades. *Energy Procedia* **129** (Supplement C), 1109–1116.

VITALE, S., PINI, M., GORI, G., GUARDONE, A., ECONOMON, T. D., PALACIOS, F. & ALONSO, J. J. 2015 Extension of the SU2 Open Source CFD code to the simulation of turbulent flows of fluids modelled with complex thermophysical laws. In *22nd AIAA Computational Fluid Dynamics Conference*.

VAN DER WAALS, J. D. 1873 Over de continuïteit van den gas - en vloeistoftoestand (on the continuity of the gas and liquid state). PhD thesis, Leiden University.

WU, J. M., SU, M. W. & MOULDEN, T. H. 1971 On the near flow field generated by the supersonic flow over rearward facing steps. *Tech. Rep.* ARL 71-0243. Aerospace Research Laboratories.

ZAKHAROVA, Y. V., GOLDFELD, M. A. & FEDOROVA, N. N. 2008 Flow investigation in combustor chamber with backward-facing step. In *International Conference on Methods of Aerophysical Research, ICMAR 2008*.

ZEL'DOVICH, Y. B. 1946 On the possibility of rarefaction shock waves. *Zh. Eksp. Teor. Fiz.* **4**, 363–364.

ZEL'DOVICH, Y. B. & RAIZER, Y. P. 1966 *Physics of shock waves and high-temperature hydrodynamic phenomena*. Academic Press.

ZUCROW, M. J. & HOFFMAN, J. D. 1977 *Gas dynamics. Volume 2 – Multidimensional flow*. John Wiley and Sons, Inc.